DISS. ETH NO. 17454

Infrared Laser-Spectroscopic Determination of Isotope Ratios of Trace Gases

A DISSERTATION SUBMITTED TO
ETH ZÜRICH

FOR THE DEGREE OF DOCTOR OF SCIENCES

PRESENTED BY
HELEN WÄCHTER

DIPL. PHYS. ETH ZÜRICH
*1978.06.04, CITIZEN OF BRITTNAU AND BRUGG AG SWITZERLAND

ACCEPTED ON RECOMMENDATIONS OF
PROF. DR. M.W. SIGRIST, EXAMINER
PROF. DR. U. KELLER, CO-EXAMINER
PROF. DR. F.J.M. HARREN, CO-EXAMINER

ZÜRICH 2007

Contents

Abstract

In addition to the general interest in trace gas sensing, the measurements of their isotopic composition provides additional information about their origin, or can be used for process identification or as tracer. This is important in ecosystem and climate research, volcanic emissions, medical diagnostics, studies of extraterrestrial atmospheres, etc.

The aim of this thesis was to develop a laser spectrometer for measurements of the isotope ratios $^{15}N/^{14}N$ in N_2O and $^{13}C/^{12}C$ and $^{18}O/^{16}O$ in CO and CO_2 at trace levels yielding a precision better than 1‰. It should be a single instrument for all three gases, several isotopes should be measurable for each molecule and no pretreatment should be required.

The standard method today is isotope-ratio mass-spectrometry, which yields an excellent precision and accuracy (<0.1‰), but it requires careful and time-consuming sample preparation and it is too bulky for field applications. Another disadvantage is that isomers like $^{14}N^{15}N^{16}O$ and $^{15}N^{14}N^{16}O$ cannot be distinguished directly, as they have the same mass. Therefore, laser spectroscopy offers an interesting alternative

The molecules of interest have their strongest absorption lines in the mid-infrared between 4 μm and 5 μm. In this wavelength range our requirements of broad tuning range, narrow line width and room temperature operation are currently best met with a cw difference frequency generation (DFG) system, yet at the cost of complexity and laser power. We implemented such a system that is based on a Nd:YAG laser (1064.5 nm, 2 W), an external cavity diode laser (ECDL; 820–870 nm, 120 mW) and a nonlinear optical crystal (periodically poled MgO-doped $LiNbO_3$) for mixing. This source provides a continuous tuning range from 4.3 μm to 4.7 μm and exhibits a narrow line width of 1 MHz. Since $LiNbO_3$ has an absorption band at 5 μm, the power decreases strongly with increasing wavelength: At 4.3 μm the power amounts to 23 μW and at 4.7 μm it drops to only 5 μW. Theoretical calculations were performed to obtain the optimal crystal length and the optimal beam parameters. A second fiber-coupled version of the DFG-system was built to have a more robust and compact laser source with a Gaussian beam shape.

An important issue in laser spectroscopic isotope measurements is the large difference in the abundances of the main and the rare isotopes (e.g. $^{15}N/^{14}N$ = 0.4%). Two different configurations were tested: An only long path detection scheme and a balanced path length detection scheme, where the main isotope is measured along a shorter path than the less abundant one. Both configurations are implemented in a single-cell setup as well as in a dual-cell setup, where the isotopes where measured simultaneously in a sample and a reference cell. In addition, two different measurement methods were compared, direct absorption spectroscopy and wavelength modulation with first harmonic detection.

N_2O isotopes were measured with concentrations between 100 ppm and 2040 ppm. The best precision was obtained by using the dual-cell arrangement. As long as there was no large temperature change, the results for only long path detection (direct absorption spectroscopy: 5‰, wavelength modulation: 6‰) and balanced path length detection (direct absorption spectroscopy: 11‰, wavelength modulation: 6‰) were similar, but small temperature changes reduce the precision of the measurement to 18‰ in the first case. The best day-to-day reproducibility (6‰) was obtained by using the fiber-coupled DFG-system in combination with balanced path length detection and wavelength modulation. The precision (9‰) of this system was comparable to the dual cell configuration in combination with the free-space DFG laser source. Measurements on isotopically enriched samples were performed and the results were in good agreement with calculations (measured 316‰±60‰, calculated: 315‰). The time resolution is better for direct absorption spectroscopy in combination with the data acquisition card (15 sec to 6 min) than for wavelength modulation (20 min).

Measurements of $^{13}C/^{12}C$ and $^{18}O/^{16}O$ with CO concentrations of 200 ppm and 300 ppm were performed with wavelength modulation and direct absorption spectroscopy. Due to the lack of suitable weak absorption lines, only the balanced path length detection scheme was implemented. The best precision (5‰) was obtained with the dual-cell setup and direct absorption spectroscopy, with wavelength modulation the precision was 11‰.

Carbon dioxide (CO_2) isotope ratios were measured in the near infrared with cavity ringdown detection and in the mid-infrared with the single cell setup. Due to the weak absorption of CO_2 in the near-infrared, high concentrations of CO_2 (50% in air) were needed. With this detection scheme a precision of 45‰ was obtained. The strong absorption lines in the mid-infrared allowed measurements of CO_2 isotopes at concentration of 450 ppm (ambient indoor air). With the single cell setup a precision of 180‰ for only long path and 270‰ for balanced path length was obtained.

In this thesis, isotope measurements with laser spectroscopy of $^{15}N/^{14}N$ in N_2O, of $^{13}C/^{12}C$ and $^{18}O/^{16}O$ in CO and CO_2 at ppm concentrations are presented. Although the goal of a precision of ≤1‰ has not yet been achieved, it is the first time that the isotope ratios of N_2O and CO were measured with laser spectroscopy at ppm concentrations with a precision of a few ‰. In contrast to previous studies where only one molecule and often only one isotope ratio were recorded, it is now feasible to measure at least two different isotope ratios in three different molecules with one device. For field measurements the detection limit and the precision still need to be improved, as concentrations in the ppb-range (e.g. 314 ppb for N_2O) and precisions ≤ 0.1‰ are required. Possible modifications of experimental arrangements that are feasible to further enhance the system performance are discussed in the last chapter.

Zusammenfassung

Spurengasanalysen spielen in vielen Gebieten eine wichtige Rolle. Isotopenverhältnisse können zusätzliche Informationen über deren Ursprung liefern, sie können für Prozessidentifizierungen oder als Tracer benutzt werden. Dies ist von grossem Interesse in der Klima- und Ökosystemforschung, in der medizinischen Diagnostik, in der Erforschung extraterrestrischer Atmosphären und vielen weiteren Gebieten.

Das Ziel dieser Dissertation war es, ein Laserspektrometer zu entwickeln, um die Isotopenverhältnisse $^{15}N/^{14}N$ in N_2O, $^{13}C/^{12}C$ und $^{18}O/^{16}O$ in CO und CO_2 mit einer Präzision ≤1‰ zu messen. Es sollte ein einziges Instrument für alle drei Gase sein, mehrere Isotopen sollten für jedes Molekül messbar sein und es sollte keine Vorbehandlung erforderlich sein.

Die heutige Standardmethode ist Massenspektrometrie für Isotopenverhältnisse. Damit werden exzellente Präzisionen und Genauigkeiten (<0.1‰) erreicht, aber die Proben müssen sorgfältig und zeitintensiv aufbereitet werden und das Instrument ist nicht geeignet für Feldmessungen. Ein weiterer Nachteil ist, dass Isomere wie $^{14}N^{15}N^{16}O$ und $^{15}N^{14}N^{16}O$ nicht direkt unterschieden werden können, weil sie die gleiche Masse haben. Deshalb bietet Laserspektroskopie eine interessante Alternative.

Die zu messenden Moleküle habe die stärksten Absorptionslinien im mittleren Infrarot zwischen 4 μm und 5 μm. In diesem Wellenlängenbereich werden unsere Anforderungen wie ein grosser Abstimmbereich, schmale Linienbreite und Betrieb bei Raumtemperatur am besten durch einen Dauerstrichlaser basierend auf Differenz-Frequenz-Erzeugung (DFG) erfüllt, allerdings auf Kosten der Laserleistung und Komplexität des Systems. Es wurde ein solches System entwickelt und aufgebaut, basierend auf einem Nd:YAG Laser (1064.5 nm, 2 W), einem Diodenlaser mit externer Kavität (ECDL; 82–870 nm, 120 mW) und einem nichtlinearen optischen Kristall (periodisch gepoltes, MgO dotiertes $LiNbO_3$). Diese Laserquelle hat einen kontinuierlichen Abstimmbereich von 4.3 μm bis 4.7 μm und eine schmale Linienbreite von 1 MHz. Weil $LiNbO_3$ ein Absorptionsband bei 5 μm hat, nimmt die Leistung mit zunehmender Wellenlänge ab: Bei 4.3 μm beträgt die Leistung 23 μW, bei 4.7 μm nur noch 5 μW. Theoretische Berechnungen wurden durchgeführt, um die optimalen Strahlparameter und die optimale Kristalllänge zu bestimmen. Es wurde auch eine zweite, fasergekoppelte Version des DFG-Systems entwickelt, um eine kompaktere und robustere Laserquelle mit einem gaussförmigen Strahlprofil zu erhalten.

Ein wichtiges Thema bei der Isotopenmessung mit Laserspektroskopie ist der grosse Unterschied in der Häufigkeit des Hauptisotopes und des seltenen Isotopes (z.B. $^{15}N/^{14}N$ = 0.4%). Zwei verschiedene Konfigurationen wurden getestet: Ein Nur-Langweg-Aufbau und ein “Balanced-Path-Length”-Aufbau, bei dem das Hauptisotop mit einer

kürzeren Weglänge gemessen wird als das seltenere Isotop. Diese Konfiguration wurde sowohl für den Aufbau mit einer Zelle verwendet, wie auch für den Doppelzellenaufbau, bei dem die Isotope gleichzeitig in einer Probezelle und einer Referenzzelle gemessen werden. Zusätzlich wurden zwei verschiedene Messmethoden verglichen, direkte Absorptions-Spektroskopie und Wellenlängenmodulation.

Lachgas (N_2O) Isotope wurden bei Konzentrationen zwischen 100 ppm und 2040 ppm gemessen. Die beste Präzision wurde mit dem Doppelzellenaufbau erreicht. Solange keine starken Temperaturschwankungen auftraten, waren die Resultate für den Nur-Langweg-Aufbau (direkte Absorptionsspektroskopie: 5‰, Wellenlängenmodulation: 6‰) und den "Balanced-Path-Length"-Aufbau gleich gut (direkte Absorptionsspektroskopie: 11‰, Wellenlängenmodulation: 6‰). Im ersten Fall verschlechterte sich die Präzision allerdings auf 18‰, wenn Temperaturschwankungen auftraten. Die beste Tag-zu-Tag-Reproduzierbarkeit (6‰) wurde mit dem fasergekoppelten DFG-System in Kombination mit dem "Balanced-Path-Length"-Aufbau und Wellenlängenmodulation erreicht. Die Präzision (9‰) dieses Systems war vergleichbar mit der des Doppelzellenaufbaus in Kombination mit dem Freistrahl-DFG-System. Zusätzlich wurden Messungen an Proben mit angereicherten seltenen Isotopen durchgeführt und die Resultate sind in guter Übereinstimmung mit den Berechnungen (gemessen: 316‰±60‰, berechnet: 315‰). Die Zeitauflösung ist besser mit direkter Absorptionsspektroskopie (15 Sek bis 6 Min) als mit Wellenlängenmodulation (20 Min).

Messungen von $^{13}C/^{12}C$ und $^{18}O/^{16}O$ in CO wurden bei Konzentration von 200 ppm und 300 ppm mit direkter Absorptiosspektroskopie und Wellenlängenmodulation durchgeführt. Da keine geeigneten schwachen Absorptionslinien existieren, wurde nur der "Balanced-Path-Length"-Aufbau verwendet. Die beste Präzision (5‰) wurde mit dem Doppelzellenaufbau und direkter Absorptionsspektroskopie erreicht, mit Wellenlängenmodulation war die Präzision 11‰.

Kohlendioxid (CO_2) Isotopenverhältnisse wurden im nahen Infrarot mit "Cavity-Ringdown" und im mittleren Infrarot mit dem Aufbau mit einer Zelle gemessen. Da die Absorption im nahen Infrarot nur schwach ist, wurden hohe Konzentrationen von CO_2 benötigt (50% in Luft). Mit diesem Aufbau wurde eine Präzision von 45‰ erreicht. Die starken Absorptionslinien im mittleren Infrarot erlauben CO_2 Isotopenmessungen bei Konzentrationen von 450 ppm (Innenraumluft). Mit dem Nur-Langweg-Aufbau mit einer Zelle wurde eine Präzision von 180‰ erreicht, mit dem "Balanced-Path-Length"-Aufbau eine von 270‰.

In dieser Dissertation wurden Isotopenmessungen mit Laserspektroskopie von $^{15}N/^{14}N$ in N_2O, $^{13}C/^{12}C$ und $^{18}O/^{16}O$ in CO und CO_2 bei ppm-Konzentrationen präsentiert. Auch wenn das Ziel einer Präzision ≤1‰ noch nicht erreicht wurde, so wurden doch zum ersten Mal die Isotopenverhältnisse von N_2O und CO bei ppm Konzentrationen mit Laserspektroskopie mit einer Präzision von einigen ‰ gemessen. Im Gegensatz zu früheren Studien, wo nur ein Gas und oft nur ein Isotopenverhältnis gemessen wurde, ist es jetzt möglich, mindestens zwei

verschiedene Isotopenverhältnisse in drei verschiedenen Molekülsorten mit einem einzigen Gerät zu messen. Für Feldmessungen müssen die Nachweisgrenze und die Präzision noch verbessert werden, da Konzentrationen im ppb-Bereich (z.B. 314 ppb für N_2O) und Präzisionen ≤0.1‰ benötigt werden. Mögliche Modifikationen des experimentellen Aufbaus zur Verbesserung des Systems werden im letzten Kapitel besprochen.

1. Introduction

1.1 Trace gases and isotopes

Trace gas sensing is of increasing interest in numerous applications including air pollution, climate research, industrial process control, agriculture, food industry, volcanology, workplace safety, homeland security, medical diagnostics, etc [Sig94]. These various application areas pose rather different requirements for sensing in terms of detection sensitivity and selectivity, but also with respect to time resolution, dynamic range, accuracy and precision, versatility, robustness and costs of instrumentation used.

Laser-spectroscopic sensing devices offer the potential for high sensitivity and selectivity, multi-component capability, large dynamic range, robustness and ease of operation. An important aspect that often distinguishes laser-based sensors from competing techniques is that usually no sample preparation, i.e. neither pre-treatment nor pre-concentration are required.

Depending on the trace species and the application, concentrations between percent (%) and ppt (10^{-12} parts-in-volume) need to be detected. This large dynamic range can be addressed by implementing a detection scheme with an inherently large dynamic range such as the photoacoustic method, by using a weak absorption line for high concentration and a strong absorption line for low concentration, and/or by employing short and long absorption paths for high and low concentrations, respectively. These are rather unique features of the spectroscopic approach, notably with tunable lasers. The detection selectivity or specificity in a multi-component gas mixture, i.e. in real-world applications, may be more difficult to achieve than sufficient sensitivity because molecular absorption features often overlap. Hence a tunable narrowband source is a prerequisite for multi-component analyses.

A laser-sensing scheme comprises a (wavelength-tunable) laser source and a detection scheme both adapted to a given application. In recent years, much progress has been made both in laser source develoment as well as in the introduction of new detection schemes and improvements on existing ones.

In this work we focus on studies devoted to isotope ratio measurements. Isotopic compositions of trace gases are of interest in such diverse fields as ecological CO_2 exchange, volcanic emission, medical diagnostics, extraterrestrial atmospheres, etc.

In *ecosystem research* isotopic ratios of CO_2, H_2O, N_2O, NO and NO_2 [Gri04, Fla98, Yak00, Bow03] are of interest as they enable to determine the source of, e.g., CO_2 (soil, plants, or combustion during energy conversion as a result of anthropogenic activity).

In *volcanic research*, the forecast of eruptions attracts a lot of interest. In addition to seismic sensors the gaseous emissions of CO_2, HCl and SO_2 and of ratios of concentrations like CO_2/SO_2 or HCl/SO_2 may be used for interpreting magmatic processes at depth. Even more interesting are, however, isotopic ratios such as $H^{35}Cl/H^{37}Cl$ or $^{13}CO_2/^{12}CO_2$ as magmatic gases may react with rocks and other fluids on their path to the earth surface. Hence, changes of isotopic ratios in emitted gases can serve as indicators of increased volcanic activity, especially for sensing the progress towards eruption [Opp98, Ted99, Cas04, Ric02, Tit06].

A further area of trace gas monitoring, particularly also with isotopic selectivity, is in non-invasive *medical diagnostics* [Ama05, Hal05, Wol05]. Exhaled human breath has been shown to contain hundreds of different species. Some of them have been identified as being characteristic for certain diseases. Isotope ratios of CO_2 have been identified as being indicators for the presence of Helicobacter pylori (Nobel prize for medicine in 2005), the bacteria associated with peptic ulcers and gastric cancer [Kol95].

A further research field concerns isotope ratio measurements in *extraterrestrial atmospheres*. A very recent preliminary investigation is devoted to the development of a near-IR tunable-diode-laser based instrument for future in-situ measurements of H_2O and CO_2 isotopes in the Martian atmosphere [Bar06].

These four (and many more) areas illustrate the importance of precise isotope ratio determinations. However, the detection of individual isotopes and of isotope ratios impose an additional challenge onto the selectivity and the dynamic range of the detection scheme because isotopes are chemically identical and often their ratios of abundance are rather small, e.g. $^{13}CO_2$ only accounts for ca. 1 % of the natural CO_2 and the ratio between the stable nitrogen isotopes $^{15}N/^{14}N$ is only ca. 0.4 %.

There are different nominations for molecules consisting of different isotopes. An *isotopologue* denotes a molecular entity that differs only in isotopic composition (e.g. CH_4, CH_3D, CH_2D_2) [Iso07a]. *Isotopomers* are isomers having the same number of each isotopic atom but differing in their positions. The term is a contraction of “isotopic isomer”. Isotopomers can be either constitutional isomers (e.g. $CH_2DCH{=}O$ and $CH_3CD{=}O$) or isotopic stereoisomers (e.g. (R)- and (S)-CH_3CHDOH or (Z)- and (E)-$CH_3CH{=}CHD$) [Mos96, Iso07b]. This means that $^{14}N^{15}N^{16}O$ and $^{15}N^{14}N^{16}O$ are isotopomers, and $^{13}C^{16}O$, $^{12}C^{18}O$ and $^{12}C^{17}O$ are isotopologues. But these terms are used like synonyms by many authors. Another often used expression is *isotopes of a molecule* (e.g. the $^{14}N^{15}N^{16}O$ and $^{15}N^{14}N^{16}O$ are isotopes of nitrous oxide). In this thesis the term *isotope of a molecule* is used throughout for the sake of simplicity.

1.2 Isotope fractionation

1.2.1 Origin of fractionation effects and definitions

In classical chemistry it is assumed that all the processes are the same for different isotopes. But if measured precisely enough, a difference can be seen in the chemical and physical behavior. This phenomenon is called isotope fractionation. It can be seen, e.g., in transitions of a compound from one state to another (liquid water to vapor water) or into another compound (carbon dioxide into plant organic carbon). Also in chemical equilibrium processes (dissolved bicarbonate and carbon dioxide) and in physical equilibrium processes (liquid and vapor) a difference in isotopic composition between the compounds can be found. The isotope ratio is defined as:

$$R = \frac{\text{abundance of rare isotope}}{\text{abundance of abundant isotope}} = \frac{^{less}C}{^{main}C} \tag{1}$$

where ^{main}C is the concentration of the main isotope and $^{minor}C$ the one of the less abundant isotope. But usually the isotope ratios are not given as absolute numbers for several reasons:

- The differences in isotope ratios are in general small. The ratios would need to be given with many digits and the differences would be difficult to be recognized.
- To compare the values they need to be compared to international standard values.
- Most time absolute values are less relevant than changes of isotope ratios during processes.

Therefore the isotope ratio of a sample normally is compared to the one of a standard reference substance and the deviation of these ratios is given by the δ-value [Cra57]:

$$\delta = \left(\frac{^{minor}C_{sample} / ^{main}C_{sample}}{^{minor}C_{ref} / ^{main}C_{ref}} - 1 \right) \cdot 1000‰ = \left(\frac{R_{sample}}{R_{ref}} - 1 \right) \cdot 1000‰ \tag{2}$$

where the indices sample and ref correspond to sample gas and standard reference gas, respectively.

The reason for the different behavior of the isotopes is the difference in mass. The kinetic energy of a molecule is determined by the temperature $kT \sim mv^2/2$, where T is the temperature in Kelvin, k is the Boltzmann constant, m is the molecular mass and v is the average molecular velocity. This means molecules with heavier isotopes have a lower velocity that the others. This has different consequences, e.g. heavier molecules have lower diffusion velocities, and the collision frequency with other molecules is lower, one reason why lighter molecules react faster in general [Whi00].

Another reason for isotope fractionation is that the heavier molecules usually have higher binding energies. The potential energy of a binding (e.g. between two molecules in a liquid or

crystal, or between two atoms in a molecule) is generally very similar for different isotopes. But the quantized energy levels in this potential depend on the mass, e.g. for a two-atomic molecule with a harmonic potential (approximation for small energies) the energy levels are given by $E_n = (n + 1/2)\hbar\omega$ with $\omega = \sqrt{f/\mu}$ where f is the spring constant and μ is the reduced mass ($\mu = m_1 m_2/(m_1 + m_2)$, m_1: mass of atom 1, m_2: mass of atom 2), leading to $E_n \propto \sqrt{1/\mu}$. This means that the energy levels of the heavier isotope are lower than for the lighter leading to a higher binding energy. As a result in most chemical reactions the light isotopic species reacts faster than the heavy one, e.g. $Ca^{12}CO_3$ dissolves faster in an acid solution than $Ca^{13}CO_3$ [Moo00]. Another effect is the fractionation during evaporation, e.g. $^1H_2{}^{18}O$ and $^2H^{16}O^1H$ have lower vapor pressure than $^1H_2{}^{16}O$ and they also evaporate less easily [Moo00]. At higher temperatures the differences between binding energies of isotopic molecules become smaller resulting in a reduced isotope effect.

In some cases it can also be the heavier isotope that reacts faster, often due to a lower binding energy of the heavier isotope. This is called inverse isotope effect. For some interactions the potential energy well is less deep for the heavy particle leading to a lower binding energy than for the lighter one. Examples for this are the higher vapor pressure of $^{13}CO_2$ in the liquid phase and the lower solubility of $^{13}CO_2$ in water compared to $^{12}CO_2$ [Moo00].

The fractionation factor α describes how isotope-selective a certain process (A ⇒ B for kinetic processes, or A ⇔ B for equilibrium processes) is and is given by:

$$\alpha_{A\to B} = \frac{R(B)}{R(A)}, \qquad \alpha_{A\leftrightarrow B} = \frac{R(B)}{R(A)} \tag{3}$$

where R(A) and R(B) denote the isotope ratios in the compounds A and B, respectively. In general isotope effects are small, i.e. $\alpha \cong 1$. Therefore it is more interesting to know the deviation of α from 1, which is called fractionation ε [Moo00]:

$$\varepsilon = \alpha_{A\to B} - 1 = \left(\frac{R(B)}{R(A)} - 1\right) \cdot 1000‰ \tag{4}$$

The fractionation ε describes the enrichment (ε > 0) or the depletion (ε < 0) of a certain process. In most cases the fractionation is rather small in the range of a few ‰. The definitions for the fractionation ε (Eq. 4) and the δ-value (Eq. 2) look very similar but mean different things. The fractionation compares the isotopic composition before and after a process or between two compounds in an equilibrium reaction whereas the δ-value compares the isotopic composition of a substance to the isotopic composition of a (international standard) reference substance.

1.2.2 Kinetic, equilibrium and mass-independent fractionation

There are three different types of fractionation: kinetic fractionation, equilibrium fractionation and mass-independent fractionation. Kinetic fractionation is related to fast, irreversible, incomplete and unidirectional physical or chemical processes. Examples are evaporation, diffusion, dissociation reactions and biochemical reactions like photosynthesis or bacterial reduction. These reactions are mainly determined by the binding energy and because the lighter isotope generally has a higher velocity and a lower binding energy the reaction product will be depleted in the heavy isotope with respect to the original substance. For kinetic fractionation the fractionation factor α and therefore the fractionation ε is given by the ratios of the reaction rates *k* of the heavy and the light isotope [Whi00]:

$$\alpha_{A\to B} = \frac{k_{heavy}}{k_{ligth}} \quad \Rightarrow \quad \varepsilon = \left(\frac{k_{heavy}}{k_{ligth}} - 1\right) \cdot 1000‰ \tag{5}$$

The second type of fractionation is equilibrium fractionation, which happens in equilibrium reactions with an isotopic exchange mechanism. Examples are evaporation and condensation of a system with a liquid and a vapor phase or some chemical reactions. This fractionation arises from the mass dependence of translational, vibrational and rotational energies of the molecules. In equilibrium reactions the system is minimizing the energy, thus the isotopes will distribute corresponding to their translational, vibrational and rotational energies. From these three energies the vibrational has the largest contribution. For equilibrium fractionation the fractionation factor is given by the equilibrium constant of the isotope exchange reaction $^{less}A + {}^{main}B \Leftrightarrow {}^{main}A + {}^{less}B$ [Moo00]:

$$\alpha_{A\leftrightarrow B} = K = \frac{{}^{main}C_A \, {}^{less}C_B}{{}^{less}C_A \, {}^{main}C_B} = \frac{R_B}{R_A} \tag{6}$$

where ${}^{main}C_S$ and ${}^{less}C_S$ are the concentration of the substance S containing the main or the less abundant isotope, respectively. Equilibrium fractionation is generally smaller than kinetic and it depends strongly on the specific process whether there is enrichment or a depletion of the heavy isotope.

Another type of fractionation can be seen, when an element has three or more isotopes, as for example oxygen exists as ^{16}O, ^{17}O and ^{18}O. Generally it is expected that the fractionation of the heaviest isotope is twice as large as for the less heavy one [Thi02] e.g.:

$$\varepsilon\left({}^{17}O\right) \approx 0.52\varepsilon\left({}^{18}O\right) \tag{7}$$

Experiments have verified this relationship for almost all cases but there are exceptions. In very few cases the fractionation seems to be independent of the mass differences that is called mass-independent fractionation. An example for this is stratospheric ozone with $\delta^{17}O$

= 80‰ and $\delta^{18}O$ = 100‰ [Bre99]. The origin of this effect is not fully understood, it might be related to the symmetry of the molecules.

1.3 Gases and isotopes of interest

1.3.1 Isotopes and standard references

1.3.1.1 Nitrogen

Nitrogen has two stable isotopes ^{14}N and ^{15}N with abundances of 99.63% and 0.368%. The standard reference material for nitrogen is the atmospheric N_2, which is the largest nitrogen reservoir and has an extremely constant isotopic composition due to its inert character [Moo00].

Strong fractionation can happen in biochemical processes like nitrification, denitrification and nitrogen fixation. They are mainly carried out by bacteria. Only little is known about the fractionation in these processes and it is difficult to predict the amount of fractionation. An important non-biological process is the dissolution of N_2 in water, which is an equilibrium process with a fractionation of +0.85‰. The natural δ-values cover a range from –12‰ (N_2 in natural gas) to +20‰ (manure) [Moo00]. Marine plankton has $\delta^{15}N$ between –3‰ to +12‰, for non-nitrogen fixing terrestrial plants (no artificial fertilizer) it is between +6‰ and +13‰ and for nitrogen-fixing terrestrial plants it varies from –2‰ to +4‰ [Whi00].

1.3.1.2 Carbon

Carbon has the two stable isotopes ^{12}C and ^{13}C with natural abundances of 98.9% and 1.1%, respectively [Hitran05]. There are several reservoirs of terrestrial carbon: atmospheric CO_2, carbon dissolved in the oceans, carbon contained in plants, in the soil and inside the earth's crust (lithosphere). The lithosphere interacts very slowly with the other reservoirs, but the exchange of carbon between the others is very fast and intense, e.g. within one year 25% of the atmospheric carbon gets exchange with the other reservoirs. This system of interacting reservoirs is called the global carbon cycle [Moo01].

The international reference standard for carbon was Pee Dee Belemnite (PDB) from North America, but it is exhausted since long times. Therefore it was replaced by Vienna Pee Dee Belemnite (V-PDB) with an abundance ratio of 0.011237 [Daw02]. The difference between PDB and V-PDB is smaller than 0.01‰.

The natural variation of $\delta^{13}C$ is as large as 100‰ for terrestrial carbon [Daw02], an overview is given in Table 1. The most depleted is bacterial methane (CH_4) with $\delta^{13}C$ between –60‰ and –80‰, the most enriched is groundwater HCO_3^- with $\delta^{13}C$ between –25‰ and +15‰ [Moo00].

Table 1: Variations of $\delta^{13}C$ in natural substances [Moo00]

Substance	**$\delta^{13}C$ [‰]**
Bacterial CH_4	–80 to –60
Groundwater HCO_3^-	–20 to +15
Freshwater carbonate	–20 to +15
Atmospheric CO_2	–10 to –5
Marine carbonate	–2 to +3
Marine plants	–20 to –10
Land C_4 plants	–15 to –10
Land C_3 plants	–30 to –20
Coal	–27 to –20
Oil	–34 to –24
Natural gas (CH_4)	–50 to –20

One of the main fractionation processes is photosynthesis. It is mainly kinetic and has a fractionation of about –18‰ [Moo00]. For the diffusion process of CO_2 into the surface layer of plant leafs a fractionation of 4.4‰ is expected from theoretical calculations, for the dissolution the equilibrium fractionation is + 0.9‰ and during hydration and dissociation of CO_2 an equilibrium fractionation of +8‰ occurs. To form organic compounds different processes with different fractionations exist. The C_3 type plants, comprising about 90% of all plants, use a process called Benson-Calvin Cycle to produce compounds containing three carbon atoms. The total fractionation of the photosynthesis of these C_3 plants is –20 to –30‰. The C_4 plants (e.g. hot-region grasses, maize, sugarcane) use the Hatch-Slack cycle to produce compounds containing four carbon atoms. The total fractionation of C_4 plants is about –13‰. A third type are the CAM plants, which have a special metabolism called Crassulacean acid metabolism. They generally use the process of the C_4 plants but sometimes also the one of the C_3 plants, hence their total fractionation lies between the ones of the two other types [Whi00, Daw02].

Other important fractionation processes are bacterial decomposition of organic matter to methane with a fractionation of –55‰ and CO_2 with a fractionation of +25‰ or the uptake of CO_2 by seawater with a fractionation of –2‰ [Moo00]. These and more fractionation processes lead to different isotopic compositions for different substances (see Table 1). The biospheric carbon has a strong influence on the atmospheric CO_2. The large uptake of CO_2 by

the plants during summer and equal release of CO_2 in winter results in a seasonal variation of the CO_2 concentration with a corresponding variation in $\delta^{13}C$ [Fla98]. Additional to this variation, an increase of the CO_2 concentration since industrialization is observed correlated to a change in $\delta^{13}C$ [Moo00].

1.3.1.3 Oxygen

Oxygen has three stable isotopes ^{16}O, ^{17}O and ^{18}O with natural abundances of 99.8%, 0.035% and 0.2%, respectively [Moo00]. The international standard reference material is either Vienna Standard Mean Ocean Water (V-SMOW) for water samples or Vienna Pee Dee Belemnite (V-PDB) for carbonate samples [Moo00]. V-SMOW has never existed in nature, it is an average over all oceans. Another standard reference material is SLAP (Standard Light Antarctic Precipitation) with $\delta^{18}O_{SLAP/V\text{-}SMOW} = -55.5‰$. The natural variations of $\delta^{18}O$ are in a range of 100‰ [Moo00]. The $\delta^{17}O$ usually gives no additional information, because normally the processes have mass-dependent fractionation and therefore $\delta^{17}O$ can be calculated from $\delta^{18}O$ as described in (7). Exceptions from this rule are called mass-independent fractionation, an example for this is ozone as mentioned above.

In the hydrological cycle the strongest fractionation of –27‰ happens during evaporation. This means that the ocean vapor (–13‰ to –12‰) is isotopically lighter than the ocean water (–0.5‰ to +0.5‰). This also influences the isotopic composition of precipitation, which has a large variation in the δ-value depending on many climatological and local factors. $\delta^{18}O$ is lower for precipitation further away from the equator, further inland, at higher altitude and during winter. Because of this the $\delta^{18}O$ of ice in the Arctic and Antarctic can be as low a –50‰, the $\delta^{18}O$ of tropic precipitation is –8‰ to –1‰ and in temperate zones it is –35‰ to –2‰. The surface water of lakes can have δ-values as high as +20‰ if there is strong evaporation [Moo00].

Photosynthesis has a fractionation of $\varepsilon^{18}O = +16‰$ to +27‰, therefore the cellulose of the most plants have $\delta^{18}O = +27‰$. During photosynthesis, CO_2 and O_2 are in oxygen isotopic equilibrium with water, which is the dominant source of O. Thus the isotopic composition of cellulose depends on the precipitation, whose isotopic composition can vary strongly [Whi00].

1.3.2 Nitrous oxide (N_2O)

The most abundant isotopes of nitrous oxide are $^{14}N_2{}^{16}O$ (99%), $^{14}N^{15}N^{16}O$ (0.36%), $^{15}N^{14}N^{16}O$ (0.36%), $^{14}N_2{}^{18}O$ (0.20%) and $^{14}N_2{}^{17}O$ (0.037%). Its isotopic composition gives important information, e.g. on ecosystem gas exchange [Esl00c]. The atmospheric concentration of N_2O has increased from 270 ppb to 314 ppb in the last 200 years [Rah97]. In

the same time the abundance of the heavy isotopes has decreased by $\delta(^{15}N^{14}N^{16}O) = -1.8‰$, $\delta(^{14}N^{15}N^{16}O) = -2.2‰$ and $\delta(^{14}N_2{}^{18}O) = -1.2‰$ [Röc03a]. This change in the isotopic signature indicates a change in the global sources of the N_2O since the beginning of the industrialization.

The main sources of nitrous oxide are bacterial nitrification and denitrification processes in soils and aquatic systems. The largest amount is most probably N_2O emission from soil and is strongly influenced by fertilizer use (natural soil: 3.3–9.9 Tg/year, agricultural soil: 0.7–4.3 Tg/year). The contribution of the oceans is about 3 Tg/year. Industrial sources (1.3 Tg/year) are nylon production, nitric acid production, fossil fuel fired plants, and vehicular emissions. The total N_2O emission is calculated to be 17.7 Tg/year [IPCC]. It is difficult to determine the emission rate for the various sources, as there are large variations with location and time. Isotope measurements can help identifying different sources.

The main sinks of nitrous oxide (12.3 Tg/year) are photolytic decomposition and reaction with electronically excited oxygen atoms $O(^1D)$ [Kai06]:

$$N_2O + h\nu \rightarrow N_2 + O(^1D) \quad (182 < \lambda < 225 \text{ nm}) \tag{8}$$

$$N_2O + O(^1D) \rightarrow NO + NO \tag{9}$$

$$N_2O + O(^1D) \rightarrow N_2 + O_2 \tag{10}$$

Reaction (8) contributes 90% of the sink, reaction (9) 6% and reaction (10) 4%. Due to small mixing of tropospheric and stratospheric air the lifetime of atmospheric N_2O is about 120 years [IPCC].

For nitrogen the international standard is the N_2 of the atmosphere ($^{15}N/^{14}N = 0.3613 \cdot 10^{-2}$) [Whi00]. Average tropospheric N_2O has $\delta^{15}N = 7.0‰$ and $\delta^{18}O = 20.7‰$, in the stratosphere it is even more enriched ($\delta^{15}N = 15‰$ and $\delta^{18}O = 12‰$) [Ste03]. Isotope fractionation of N_2O occurs mostly in the stratosphere by photolytic decomposition, where the lighter isotope is preferred, leading to an enrichment of the heavier isotopes of the stratospheric N_2O. In addition, the fractionation of N_2O depends on the position of the N isotope within the linear N_2O isotope molecule, i.e. there is a difference whether the ^{15}N is in the center or at the end of the N_2O molecule [Röc01], known as site-selective fractionation. Since this fractionation happens mainly in the stratosphere the isotopic composition of N_2O in the earth atmosphere depends strongly on the altitude. The major land biospheric sources of N_2O are depleted in ^{15}N and ^{18}O relative to the troposphere, so the isotopic composition of tropospheric N_2O can only be explained by large back fluxes from the enriched stratospheric N_2O [Ste03]. N_2O production in soil and oceans originates mainly from nitrification and denitrification of ammonia and nitrate by bacteria. Some of these enzymatic processes have a large fractionation and depending on environmental conditions several pathways are possible leading to different isotopic signatures of all [Ste03]. Not all of these processes are fully understood and site-selective ^{15}N measurements could give further insights.

1.3.3 Carbon monoxide (CO)

Carbon monoxide plays an important role in our atmosphere because its main sink is the reaction with the OH radical ($CO + OH \Rightarrow CO_2 + H$), therefore 60% of atmosphere's OH-based self-cleaning capacity is occupied by CO. This means that CO competes with CH_4 and many other species for available OH. Therefore an increase in CO emission leads to a lower OH level inducing an increase in CH_4, which is a strong greenhouse gas [Bre99].

The main sources of atmospheric CO are fossil fuel combustion (300–550 Tg/yr), biomass burning (300–700 Tg/yr), CH_4 oxidation (400–1000 Tg/yr) and non-methane hydrocarbon oxidation (200–600 Tg/yr) [Bre99]. Each source has its characteristic isotopic composition offering the possibility to identify the sources of atmospheric CO.

The isotope ratios of special interest are $^{13}C/^{12}C$ (1%) and $^{18}O/^{16}O$ (0.2%), sometimes also the relation between $^{17}O/^{16}O$ (0.04%) and $^{18}O/^{16}O$ or the concentration of ^{14}CO (10 molecules/cm^3) contain important information [Hitran05, Bre99]. Depending on the source, $\delta^{13}C$ is between –21‰ and –35‰, but also values of –53‰ have been measured (see Table 2) [Bre99]. The value varies in an annual cycle with an amplitude of 6‰ to7‰ because of enhanced methane oxidation in summer [Mak03].

The value of $\delta^{18}O$ varies for the different sources from 0‰ to 24‰, which is more than for the value of $\delta^{13}C$, and it is therefore an important parameter for identification of CO sources (see Table 2) [Bre99]. The $\delta^{18}O$ also follows an annual cycle with an amplitude of 8‰, which is mainly caused by the varying strength of sources and by kinetic fractionation resulting from the CO + OH reaction [Mak03]. Because heavier isotopes have a lower zero point energy their reaction rate k is normally lower but the CO + OH reaction shows an inverse isotope effect of $\varepsilon = 10‰$ (Eq. 7) [Mak03].

Table 2: Isotopic composition of different CO sources [Bre99]. (NMHC: Non-Methane-Hydro-Carbons)

Source	**$\delta^{13}C$ [‰]**	**$\delta^{18}O$ [‰]**
Fossil fuel combustion	–27.5	23.5
Biomass burning	–21.3	16.3
CH_4 oxidation	–52.6	0 to 15
NMHC oxidation	–32.2	0 to 15

For nearly all substances on earth the isotopic composition $\delta^{17}O$ always corresponds to the isotopic composition of $\delta^{18}O$ with $\delta^{17}O = 0.5\ \delta^{18}O$. Deviations from this value are called mass independent fractionation [Thi02], a typical example for this is ozone with $\delta^{17}O = 80‰$ and $\delta^{18}O = 100‰$. But also CO shows a small excess of ^{17}O due to ozonolysis and the CO+OH reaction [Bre99].

The radioactive isotope ^{14}C is mainly produced in the stratosphere by cosmic radiation and therefore the concentration of ^{14}CO gives information about effects due to transport and to CO removal by OH [Bre99].

1.3.4 Carbon dioxide (CO_2)

Carbon dioxide plays an important role in many different fields, e.g. in the environment, in the atmosphere, in biology, in medicine, in industry etc. Carbon dioxide is a strong greenhouse gas and with a concentration of 380 ppm it is one of the most abundant trace gases in the atmosphere.

Atmospheric CO_2 is strongly interacting with other carbon reservoirs on earth, namely oceans, terrestrial plants, soil, and lithosphere. The latter is only interacting very slowly with the others and is therefore negligible. Between the other reservoirs the interaction is very fast, in one year 25% of the atmospheric carbon is exchanged [Moo01]. These fluxes in this carbon cycle can be analyzed by measuring the isotopes of CO_2.

The main isotope is $^{12}C^{16}O_2$ (98%) and the most important less abundant isotopes are $^{13}C^{16}O_2$ (1.1%) and $^{18}O^{12}C^{16}O$ (0.39%). There are other combinations of carbon isotopes and oxygen isotopes but their abundances are even lower. The δ-value of atmospheric CO_2 has small seasonal variations due to plant activities and therefore the δ-value itself and its variations strongly depend on location, e.g. $\delta(^{13}C^{16}O_2)$ and $\delta(^{18}O^{12}C^{16}O)$ have variations of about 1‰ at Point Barrow (Alaska), but at the South Pole no seasonal variations are observed [Moo01].

Before industrialization the average concentration was 270 ppm, today it is 380 ppm and it is still increasing with an annual increase of 0.5%. This increase is mainly due to fossil fuel combustion (5.4 Gt/year) and changing use of land (1.7 Gt/year) mainly deforestation [Moo01]. Half of the CO_2 emissions are directly taken up by the oceans and land plants. Due to different amounts of land masses in the northern and southern hemisphere there is a weak gradient in the CO_2 concentration.

Every source in the carbon cycle has its specific isotopic composition and many chemical processes involving CO_2 are isotope selective. Before industrialization the $\delta^{13}C$ of atmospheric CO_2 was –7‰, until today this value has decreased by 1.5‰ due to changes of CO_2 sources. CO_2 dissolved in oceans has a slightly positive δ-value of 1‰, atmospheric CO_2 has a more negative δ-value of –8‰, land plants and soil have $\delta^{13}C = –25‰$ and fossil fuel has $\delta^{13}C = –28‰$ [Moo01]. Photosynthesis has a fractionation of –17‰ and CO_2 uptake by oceans has a fractionation of –2‰. The oxygen isotopes show a completely different behavior than the carbon isotopes. The value of $\delta^{18}O$ is mainly influenced by isotope exchange with water and therefore it is strongly influenced by oceans and precipitation. In

the stratosphere the water concentration is very low and CO_2 shows a large enrichment in ^{17}O due to isotope transfer with ozone [Blu02].

The isotopic composition of CO_2 close to the ground and in the soil is strongly influenced by land plants and therefore has an annual cycle in CO_2 concentration, in $\delta^{13}C$ and in $\delta^{18}O$. The latter is influenced by plants as for photosynthesis three CO_2 molecules are taken up but only one is really used. The other two are then in equilibrium with the leaf water where oxygen isotope exchange happens, before they exit the plant again. Therefore $\delta^{18}O$ directly yields information about plant activities [Moo01].

The isotopic composition of CO_2 produced by fossil fuel burning changes strongly with the type of fuel, as coal, oil, natural gas etc. were produced from different land and water plants by different chemical processes. For example $\delta^{13}C$ varies in natural gas between –20‰ to –50‰ [Moo00]. Generally rather negative $\delta^{13}C$ values are obtained by fossil fuel burning, the global average is about –27‰. The value of $\delta^{13}C$ decreases with increasing CO_2 production [Moo01]:

$$\Delta\delta^{13}C/\Delta CO_2 = -0.015‰/ppm$$
$$\Delta\delta^{13}C/year = -0.025‰/year$$

This is not simply mixing of CO_2 from fossil fuel burning with atmospheric CO_2. Large amounts of emitted CO_2 are taken up by the oceans, where mixing and isotope exchange happens and are released again with a certain fractionation. Thus the oceans tend to wash out the original signature of the fossil fuel CO_2 to a large extent. The terrestrial biosphere does not show this behavior because the carbon reservoir is not mixed as in the oceans, most of the CO_2 taken up in the growing season returns into the atmosphere later in the year with identical $\delta^{13}C$.

1.4 Measurement methods

1.4.1 Isotope ratio mass spectrometry (IRMS)

Today, the standard method for such measurements is isotope-ratio-mass-spectrometry (IRMS). The advantage of IRMS is its high precision and accuracy. As example Röckmann et al. [Röc03b] developed an IRMS instrument in combination with gas chromatography yielding a reproducibility of ±0.1‰ for $\delta^{15}N$ in N_2O. For N_2O isotope measurements, pure N_2O samples have to be extracted from the air samples by gas chromatography. As CO_2 has a more than 1000 times higher concentration it needs to be removed first with a chemical trap, otherwise it would saturate the chromatographic column [Röc03b]. Unfortunately, isomers like $^{14}N^{15}N^{16}O$, $^{15}N^{14}N^{16}O$ and $^{14}N_2{}^{17}O$, cannot be distinguished directly, as they all have the

same mass. In order to be able to distinguish $\delta^{14}N^{15}N^{16}O$ and $\delta^{15}N^{14}N^{16}O$, N_2O needs to be fragmented into NO and then comparison of the $\delta^{15}N$ of NO and the $\delta^{15}N$ of N_2O gives the site-selective isotopic composition [Röc03b].

A second example is the isotopic composition of atmospheric CO related to air pollution, which was measured by Gros et al. [Gro02] with a precision of 0.1‰ for $\delta^{13}C$, 0.2‰ for $\delta^{18}O$ and 0.3‰ for $\Delta^{17}O$, which is the deviation from the expected $\delta^{17}O$ in relation to $\delta^{18}O$. Nakagawa et al. [Nak04] measured the isotopic composition of CO in Pacific Ocean water with a precision of 0.2‰ for $\delta^{13}C$, and 1‰ for $\delta^{18}O$. To measure carbon monoxide with IRMS the samples need to be purified and the CO needs to be converted to CO_2 by Schütze reagent [Sch49, Smi65] and then the CO_2 is cryogenically trapped [Bre99]. From this CO_2 the isotopic compositions $\delta^{13}C$ and $\delta^{18}O$ can be measured. To measure $\delta^{17}O$ the CO_2 needs to be transformed to O_2 because $^{13}C^{16}O$ and $^{12}C^{17}O$ have the same mass. When measuring $\delta^{13}C$ the value needs to be corrected by the amount of ^{17}O, normally this is done by measuring $\delta^{18}O$ and assuming normal mass dependent fractionation. But since CO shows a small mass independent fractionation this value might be wrong.

Isotope measurements of CO_2 were done by many different groups, as $\delta^{13}C$ and $\delta^{18}O$ of CO_2 is very important for studying the global carbon cycle or climate changes [Gho03] and materials containing C or O usually are converted to CO_2 for isotope measurements [Gho03]. Therefore it is a well-known method for this gas and good precisions can be obtained for the isotope ratios. For example, precisions of 0.012‰ for $\delta^{13}C$ and 0.019‰ $\delta^{18}O$ have been obtained by Werner et al. [Wer01]. Nevertheless, measurements of different laboratories often disagree by 10 times their reported precisions [Cop06], leading to a reduced accuracy. These differences may result from unidentified contaminations with other gases and isotope dependent release of CO_2 from the cold surface in the cold trap, which is needed to extract pure CO_2 from air [Wer01].

1.4.2 Fourier transform infrared spectroscopy (FTIR)

Isotope ratios have been determined in N_2O by FTIR spectroscopy as well, in particular also the $^{15}N/^{14}N$ ratio in N_2O has been measured site-selectively with FTIR spectroscopy [Esl00c, Tur00, Zha00, Gri00]. The best precision was obtained by Esler et al. [Esl00c] with a laboratory-based high resolution (0.012 cm^{-1}) FTIR spectrometer with a multipass cell of 2.4 m path length. The achieved precisions in pure N_2O are 0.6‰ for $\delta^{14}N^{15}N^{16}O$, 1.4‰ for $\delta^{15}N^{14}N^{16}O$, 2.5‰ for $\delta^{14}N_2{}^{16}O$, and 4.4‰ for $\delta^{14}N_2{}^{17}O$. Griffith et al. [Gri00] measured the isotope fractionation of N_2O in the stratosphere with a balloon-borne FTIR instrument by recording the spectrum at rising or setting sun through the limb of the earth's atmosphere. By using the sun as light source and the long path of the light through the atmosphere at sunrise

and sunset, they were able to measure $\delta^{14}N^{15}N^{16}O$ and $\delta^{15}N^{14}N^{16}O$ at atmospheric concentrations (313 ppb) with a precision of 5‰ at different altitudes in the stratosphere.

The isotopic composition of CO has been measured by Feilberg et al. [Fei02] to determine the reaction rate of CO + OH for the different isotopes. Gas samples of different CO isotopes, ozone, water vapor and synthetic air were mixed together. In this mixture the ratios of reaction rates (Eq. 3) of $^{13}C^{16}O$ (α = 0.960±0.014), $^{12}C^{18}O$ (α = 0.943±0.019), and $^{13}C^{18}O$ (α = 0.948±0.024) relative to $^{12}C^{16}O$ were determined and also the reaction rate of $^{12}C^{17}O$ (α = 0.996±0.0067) relative to $^{12}C^{18}O$.

The $^{13}C/^{12}C$ ratio in CO_2 has been measured with FTIR spectroscopy by Esler et al. [Esl00a, Esl00b]. This method relies on calibration using synthetically calculated absorbance spectra and a chemometric multivariate calibration algorithm. It can directly be applied to air samples. The analysis is carried out on a benchtop instrument (spectral resolution: 1 cm^{-1}), which is deployable for field studies. The authors demonstrated the determination of the $^{13}C/^{12}C$ ratio of CO_2 in air with an analytical precision of the order of ±0.1‰. Since $^{18}O^{12}C^{16}O$ was included in the calibration, in principle it is possible to derive a value for $\delta^{18}O$ but the precision is too poor to measure small variations in natural abundance. A field deployable instrument has been developed by Mohn et al. [Moh07] with a precision of ±0.15‰ and an accuracy of 0.4‰ for $^{13}C/^{12}C$ in ambient CO_2. For this a new calibration algorithm was developed.

1.4.3 Laser spectroscopy

In recent years laser spectroscopy has attracted considerable attention as a useful alternative. Based on the good selectivity and time resolution, the technique is of particular interest also for isotopes and isomers. Laser-based sensing can be divided into near-IR [Lau06, Cas05, Gag03, Cro02, Hör04] and mid-IR [Man05, Gag05, Tuz07, Dah01, Lee91, Bow03, Cla04, Bor03, Erd02, Ric02] systems. Near-IR systems use diode lasers and probe weak overtone and combination bands of molecules. Hence, their sensitivity is limited. Mid-IR systems employ lead salt diode lasers [Lee91, Man02, Bow03], quantum cascade lasers (QCLs) [Man05, Gag05, Tuz07, Dah01] or nonlinear optical devices – notably difference frequency generation (DFG) sources [Cla04, Bor03, Erd02, Ric02, Mad05] – and probe fundamental infrared absorption bands of molecules. They are inherently more sensitive – i.e. can detect lower concentrations – provided appropriate detection techniques are available. Detection schemes such as direct absorption spectroscopy [Han94, Nel04, Erd02, Man05], wavelength modulation [Ker05, Cas04, Gag03, Gag02, Wei04, Cla04], optogalvanic spectroscopy [Mur94], cavity ringdown or cavity leak-out spectroscopy [Cro02, Dah01, Bak04, Hal05, Bor03] have been employed. Another detection scheme is photoacoustic spectroscopy [Lau06, Sig94, Web05, Wol05, Kos05], but for isotope selective measurements it is less

suitable because of the need of higher pressure. The overlapping of the absorption lines permits only large changes in the isotopic ratio to be observed [Wol05].

Until now most of the laser spectroscopic measurements of isotope ratios were done with high concentrations, especially N_2O isotopes were only measured in pure N_2O samples. Uehara et al. [Ueh03a, Ueh03b] measured the $^{15}N/^{14}N$ ratio in pure N_2O with a diode laser at 2 μm with a precision of $\Delta\delta = 0.3‰$ in a multipass cell by using two different path lengths for the main and the less abundant isotopes (balanced path length detection scheme). Gagliardi et al. [Gag05] measured the isotopic composition of pure samples of CH_4 and N_2O in with a cryogenically cooled quantum cascade laser (QCL) at 8 μm and wavelength modulation in a single path cell. For CH_4 they achieved a precision of $\Delta\delta = 9‰$, for N_2O the situation was less favourable because the preferred absorption lines were outside the QCL wavelength range. In another study, Gagliardi et al. [Gag03] used a near-IR diode laser for $^{13}CO_2/^{12}CO_2$ measurements again employing wavelength modulation and achieving a short-term precision of 0.03%. They also discussed a possible use of this portable instrument for in-situ measurements in volcanic gases.

First laser-spectroscopic measurements of CO isotopes were done by Lee et al. [Lee91]. A lead salt diode laser at 4.7 μm was used in combination with a White cell, which offered different path lengths for the main and the less abundant isotopes. To improve the signal to noise ratio wavelength modulation with second harmonic detection was used. They obtained a precision of 0.5% for the $^{13}C^{16}O/^{12}C^{16}O$ ratio of 2.37 ppm CO in air and a precision of 1.5% for the $^{12}C^{18}O/^{12}C^{16}O$ ratio. These precisions are too large to observe differences in isotope ratios of a few ‰.

The best precision of $\Delta\delta = 0.18‰$ was obtained by McManus et al. [Man05, Sal06] for the $^{13}C/^{12}C$ ratio of CO_2 in atmospheric air with a pulsed QCL at 4.3 μm and a multipass cell with balanced path length detection. The advantage of this system is its near room-temperature operation (except for the cryogenically cooled IR detector but that may be replaced by a Peltier-cooled detector in the future). However the drawback is the comparatively large QCL line width, which exceeds the molecular absorption line width and hence complicates the data evaluation and in some cases of other isotopes may even impede an accurate isotopic analysis particularly in the presence of other interfering compounds. With a similar setup, but using only one path length, Tuzson et al. [Tuz07] obtained a precision of $\Delta\delta = 0.16‰$ for $^{13}C/^{12}C$ and $\Delta\delta = 0.25‰$ for $^{16}O/^{18}O$ in ambient CO_2, which is the best result until today. Castrillo et al. [Cas04] made first field measurements of isotope ratio of volcanic CO_2 with an accuracy of 0.5‰ for $^{13}C/^{12}C$. Their spectrometer consists of a diode laser at 2 μm and two single pass cells for the sample and the reference gas, respectively. The only pre-treatment was drying and cooling of the gas samples making it a quasi-continuous measurement system.

1.4.4 Comparison of methods

Although isotope-ratio mass-spectrometry (IRMS) has many advantages like high precision and accuracy and being a well-known and established method it has also some disadvantages: It requires careful and time-consuming sample preparation and the instrument is too bulky for field measurements. In addition, IRMS is insensitive to isomers, e.g. $^{14}N^{15}N^{16}O$ and $^{15}N^{14}N^{16}O$ or $^{12}C^{17}O$ and $^{13}C^{16}O$ cannot be distinguished directly.

Fourier transform infrared spectroscopy (FTIR) has the advantage that it is a well established method and it has a good selectivity, e.g. it can distinguish between $^{14}N^{15}N^{16}O$ and $^{15}N^{14}N^{16}O$, but it requires high resolution instruments and yield long measurement times. Good precisions are only obtained for high concentrations and for molecules and isotopes where the shift of the absorption lines between different isotopic compositions is rather large.

Laser spectroscopy offers a useful alternative because it needs no sample preparation, small instruments can be designed for field measurements, it offers a better selectivity regarding molecules and isotopes with the same mass, and a good time resolution. But the small variations of the δ-value in nature and the low concentrations of trace gases in ambient air still pose a big challenge for laser spectroscopy. It is evident that there is a great potential in laser-based spectroscopic methods that has not been fully exploited yet. Hitherto, all studies have addressed isotopes of one or a maximum of two molecules at a time and have been performed in pure gases or at rather high concentrations in the percent to ppm-range. For many real-world applications, however, concentrations are much lower, e.g. typically 300 ppb for ambient N_2O. Furthermore, the required precision of <1‰ and sufficient reproducibility are often not achieved. This is crucial as the changes in isotopic composition are usually very small, e.g. δ-values are typically of the order of a few ‰.

This thesis discusses high precision measurements of isotope ratios of gases at trace concentration, particularly of N_2O, CO and CO_2 isotopes at ppm levels. We developed and implemented a mid-IR laser spectrometer based on difference frequency generation and two different detection schemes, namely balanced path length detection and only long path detection. The spectra were recorded with two different methods, wavelength modulation and direct absorption spectroscopy. All combinations of measurement methods and detection schemes were tested regarding precision of a single measurement and long-term stability and the advantages and disadvantages are discussed.

2. Near infrared spectroscopy on CO_2 isotopes

2.1 Introduction

Most molecules can be measured both in the mid-infrared and in the near infrared. Both wavelength ranges have their own advantages and disadvantages. The strongest absorption lines usually are in the mid-infrared (see Figure 1) but then the choice of laser source is rather limited. At, e.g., 4.3 μm, where CO_2 has its strongest absorption lines, there are only lead salt diode laser, which require cryogenic cooling and offer only low power (<0.1 mW), or quantum cascade laser, which need also cryogenic cooling for continuous wave operation or have a large line width in pulsed mode. Another possibility is to use nonlinear crystals for difference-frequency generation (see chapter 3) or optical parametric oscillators.

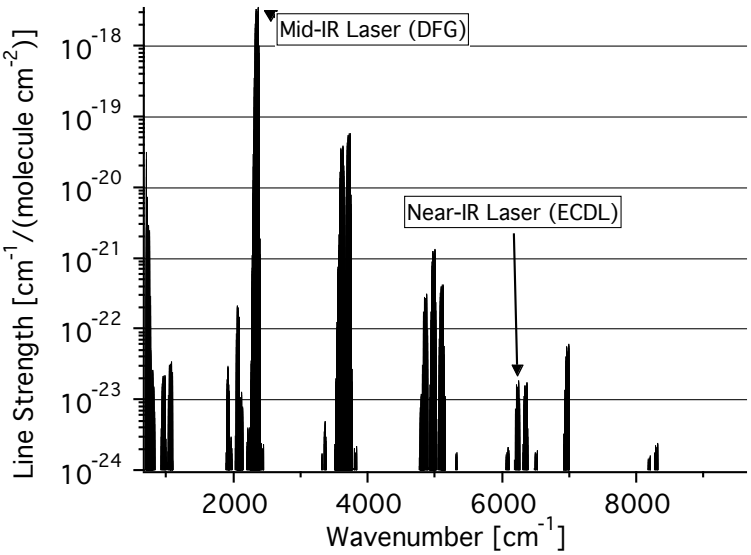

Figure 1: Absorption lines of CO_2 at different wavenumbers [Hitran05]. In the near-IR at 1.6 μm the absorption lines are five orders of magnitude weaker than the strongest ones in the mid-IR. (DFG: Difference-frequency generation; ECDL: External cavity diode laser)

In the near infrared the selection of lasers is much wider, especially in the telecom wavelength range around 1.55 μm where diode lasers of high quality and low price are available. In combination with an external cavity, a laser system with a broad tuning range, high laser power and easy operation is obtained. But the absorption line strength of the molecules is usually much lower, e.g. for CO_2 it is five orders of magnitude lower than in the

mid-infrared (see Figure 1). This means that more sensitive detection methods, e.g. cavity ringdown, are required, which complicates the setup again.

In this work two different setups were tested, either using a near infrared laser and cavity ringdown or using a mid-infrared laser source based on difference frequency generation together with a multipass cell. In this chapter the near infrared setup is described. The molecules of interest are CO_2, CO and N_2O. For the less abundant isotopes, however, only information on CO_2 is available in the Hitran database 2000 [Hitran00]. Therefore only the isotopic composition of CO_2 was studied with this setup.

2.2 Cavity ringdown theory

Cavity ringdown spectroscopy is a very sensitive technique to measure the absorption in a gas. Originally, this technique was used for sensitive measurements of the reflectivity of mirrors [Her80, And84]. The first applications of cavity ringdown for spectroscopy were reported in 1988 by O'Keefe and Deacon [Oke88]. The method bases on the fact that a photon in an optical cavity has a limited lifetime that depends on the losses of the cavity, i.e. mainly on the reflectivity of the mirrors and the absorption between the mirrors. This photon lifetime can be measured as intensity decay of the light coupled into the cavity when switching off the incoming beam. Because this decay time (ringdown time) is rather short, fast detectors are needed and this technique can only be used with high reflectivity mirrors and low gas absorption.

A setup for gas measurements with cavity ringdown mainly consists of a tunable laser source, a high finesse cavity and a fast detector, as depicted in Figure 2. To build a stable optical cavity the relationship between the cavity length L and the mirror curvature radius $\Re_m$ should fulfill the following stability condition [Sie86].

$$0 \le g_1 \cdot g_2 \le 1 \quad \text{with} \quad g_j = \left(1 - \frac{L}{\Re_{m_j}}\right) \tag{11}$$

For a symmetric cavity ($\Re_{m1} = \Re_{m2}$), as it is often used for cavity ringdown experiments, i.e. $g_1 = g_2 = g$, Eq. (11) is fulfilled for:

$$L \le 2\Re_m \tag{12}$$

This means that the cavity length L should be shorter than twice the mirror curvature radius $\Re_m$. This is the case in this experiment where the cavity length is L = 52 cm and the mirror curvature radius is $\Re_m$ = 1 m.

To couple a laser beam into a cavity the beam needs to be matched to the cavity modes. An optical cavity has different spatial modes ($TEM_{q,p}$), which have different ringdown times. Therefore the beam shape usually is matched to the $TEM_{0,0}$ mode by using an appropriate lens in front of the cavity. If a continuous wave laser is used, either the wavelength or the

cavity length needs to be adjusted so that the longitudinal cavity mode fits to the laser wavelength.

When the laser beam is mode-matched to the cavity, light can be coupled in and an intensity build-up occurs. After switching off the laser beam the light intensity in the cavity decays exponentially with a certain time constant τ [Ber00, Sch97].

$$I(t) = I_0 \exp(-t/\tau) \tag{13}$$

This decay time τ depends on the losses of the cavity, which are mainly given by the reflectivity of the mirrors and by the absorption of the gases in the cavity. To find out the relationship between the losses and the decay time, the light coupled in is thought as light packet traveling in the cavity going back and forth between the two cavity mirrors. Then the intensity of the light packet or of the pulse after one round trip in the cavity is given by:

$$I_{rt} = I_0 R_1 R_2 e^{-2\alpha L} = I_0 e^{-2\alpha_{av} L} \quad \text{with} \quad \alpha_{av} = -\frac{1}{2L}\ln(R_1 R_2) + \alpha \tag{14}$$

Here R_1 and R_2 are the reflectivities of the cavity mirrors, α is the absorption coefficient of the gas in the cavity and L is the cavity length. α_{av} is called the average loss coefficient and is useful to obtain the time dependence of the light intensity in the cavity. The time needed for one round trip is $t_{rt} = 2L/c$, so the relationship between the decay time τ and the losses α_{av} is given by:

$$I(t_{rt}) = I_0 e^{-t_{rt}/\tau} = I_0 e^{-2\alpha_{av} L} \quad \Rightarrow \quad \tau = \frac{t_{rt}}{2\alpha_{av} L} = \frac{1}{c\alpha_{av}} \tag{15}$$

where I_0 is the initial intensity and c is the speed of light. When using two identical mirrors $R_1 = R_2 = R$ with high reflectivity $R \approx 1$ then the formula for the average losses α_{av} and thus the formula for the decay time τ can be simplified with $\ln(R^{-1}) = 1 - R$:

$$\alpha_{av} = \frac{1-R}{L} + \alpha \quad \Rightarrow \quad \tau = \frac{1}{c\left(\frac{1-R}{L} + \alpha\right)} \tag{16}$$

In the case when no absorbing gas is present in the cavity the decay time τ_{empty} is only given by the reflectivity R of the mirrors and the cavity length L:

$$\tau_{empty} = \frac{L}{c(1-R)} \tag{17}$$

To obtain the absorption coefficient α of the gas filled into the cavity it is sufficient to measure the decay time of the empty cavity and of the gas-filled cavity. The difference of the inverse of the decay times directly gives the absorption coefficient of the gas [Bus99]:

$$\alpha = \frac{1}{c}\left(\frac{1}{\tau} - \frac{1}{\tau_{empty}}\right) \tag{18}$$

When measuring the ringdown time of the empty cell and of the cell filled with a sample gas the absorption coefficient can thus simply be obtained by using Eq. (18). The advantage of this method is that the absorption coefficient is obtained directly by comparing two time

constants. This is in contrast to transmission spectroscopy where the difference between two strong signal amplitudes is taken, a background needs to be subtracted and the absorption needs to be corrected with the path length.

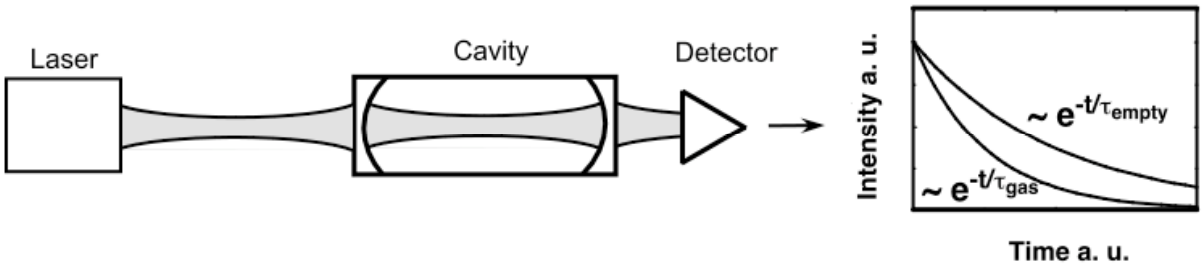

Figure 2: Laser light is coupled into a high-finesse cavity and after switching off the laser beam a ringdown event is observed by the photodiode. The ringdown time depends on the absorption in the cell and therefore yields information about the compounds and concentrations of the gas.

The detection limit is related to the precision of the measurement of the ringdown time of the empty cell τ_{empty} and is given as [Zal95]:

$$\alpha_{\min} = \frac{1}{c}\left(\frac{1}{\tau_{empty} - \Delta\tau} - \frac{1}{\tau_{empty}}\right) = \frac{(1-R)\Delta\tau}{L(\tau_{empty} - \Delta\tau)} \tag{19}$$

where $\Delta\tau$ is the minimum deviation that still can be detected. Usually for $\Delta\tau$ the standard deviation of several measurements of the empty cavity is taken. The detection limit is increased if the cavity length L is increased, if the mirror reflectivity is increased or if the standard deviation of the measured ringdown times is reduced. The latter can be done by averaging over several ringdown events before fitting an exponential decay curve.

A low detection limit does not necessarily correspond to a high precision of the measurements. For this also the wavelength needs to be measured precisely and the line strength needs to be known well enough as the concentration is given by the area under the absorption line.

2.3 Experiments, measurements and results

2.3.1 Experimental arrangement

The setup (see Figure 3) for the cavity ringdown experiment consists of an external cavity diode laser (ECDL, Tunics BT1600) with a wavelength of about 1.6 μm, an acousto-optical modulator (AOM, Infra Action, FCM-401E5C) to switch off the laser beam fast, a cavity ringdown cell with high-reflectivity mirrors, and a photodiode (InGaAs, New Focus, Model

1811) to record the ringdown event. The ECDL has a power of 6 mW, a coarse tuning range of 1.57 – 1.62 μm and a fine-tuning range of 5 GHz. It is fiber coupled with a silica-based single-mode fiber.

Two high-reflectivity mirrors (Los Gatos Inc.) with a reflectivity of >99.99% are used to build the high-finesse cavity. One of the mirrors is directly used as window of the cell, the other mirror is mounted on a ring piezo (Piezomechanik HPSt 100/25-15/15 V VS35), which enables to sweep the cavity length to match the cavity modes to the laser wavelength. Both mirrors can be aligned from outside without opening the cell. The cell itself is made from stainless steel tubes with a total length of 57 cm and an inner diameter of 3.5 cm, which gives a cell volume smaller than 0.6 liter. The distance between the mirrors is 52 cm. The longer the cavity the longer the ringdown time, which make it easier to measure it more precise. The chosen length of 52 cm is a compromise between having a long ringdown time and having reasonable cell dimensions. For the second window of the cell a lens is used, which focuses the beam onto the photodiode. The signal from the photodiode is recorded by an oscilloscope (Tektronix, TDS 620). A more detailed discussion of the system can be found in [Vog06].

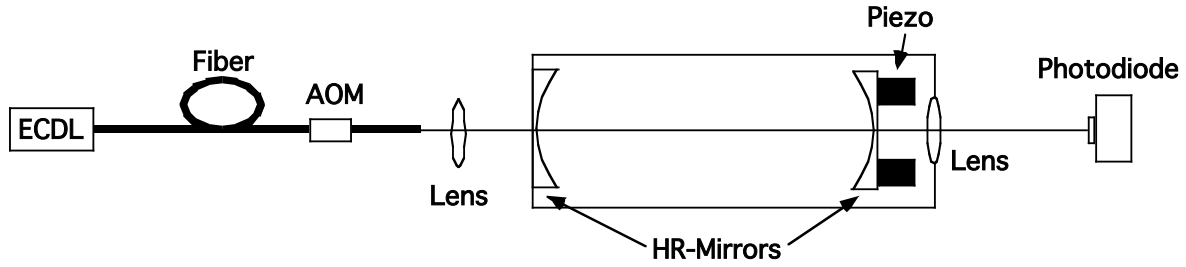

Figure 3: Setup of the cavity ring down experiment. The light of a fiber-coupled external cavity diode laser (ECDL) is coupled into a high-finesse cavity. When the light is switched off by the acousto-optical modulator (AOM) the ringdown event is recorded with the photodiode.

To align the cavity first both mirrors were aligned so that the reflected beam overlapped with the incoming beam. Then the mirrors were aligned to highest transmission and shortest ringdown time. The latter indicates that the TEM_{00} mode was obtained because higher modes usually have longer ringdown times.

2.3.2 Measurements and data evaluation

The isotopic ratio of $^{13}C/^{12}C$ of 50% CO_2 in air was measured at a pressure of 5 mbar. The selected absorption lines at 1597.792 nm for $^{13}CO_2$ and 1597.732 nm for $^{12}CO_2$ have similar line strength when corrected with the natural abundance of the isotopes [Hitran05]. To measure an absorption spectrum the wavelength of the laser was scanned in steps of 0.1 GHz. The voltage of the piezo was modulated with a frequency of 10 Hz so that the cavity length is

swept at least over one free spectral range. When a cavity mode matches the wavelength the transmission through the cavity increases rapidly. If the modulation is too fast, this buildup is incomplete leading to a lower signal. When the signal is large enough a trigger signal is sent from the oscilloscope to the acousto-optical modulator to switch off the laser beam and the ringdown event is recorded by the oscilloscope. To improve the signal-to-noise ratio we averaged over 100 ringdown events before fitting an exponential decay function. Such a measurement of an averaged ringdown event is shown in Figure 4.

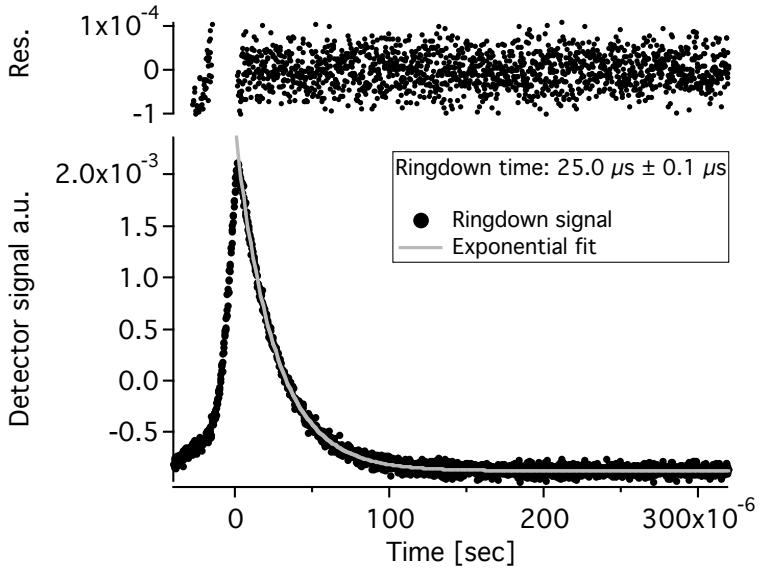

Figure 4: Ringdown signal and exponential fit. On top the residual is plotted. The ringdown signal was obtained by averaging over 100 ringdown events. The exponential fit provides a ringdown time of 25.0 μs ± 0.1 μs for this measurement.

A fast fitting algorithm for a single-exponential function [Hal04] has been implemented, which is about 700 times faster than the nonlinear Levenberg-Marquardt algorithm provided by Labview. The averaged ringdown time of the empty cavity is 25.2 ± 0.2 μs. It was obtained by measuring the ringdown time at wavelengths between the absorption lines. The ringdown time is rather sensitive to the alignment of the mirrors it varies between 20 μs and 30 μs most probably due to local variations of the mirror reflectivity. The measured absorption lines $\alpha(\nu)$ were fitted with a Gaussian curve (see Figure 5), then concentration of each isotope is determined by the area under the curve divided by the line strength S_{ij}.

$$N = \frac{1}{S_{ij}} \int \alpha(\nu) \mathrm{d}\nu \tag{20}$$

where N denotes the number of molecules per volume. The concentration is then given by comparing N to the total number of molecules. The isotope ratio is calculated by comparing the number of $^{13}C^{16}O_2$ molecules and the number of $^{12}C^{16}O_2$ molecules. The measurement time is rather long it takes about two hours for one isotope-ratio measurement.

2.3.3 Results

The derived isotopic ratio was $^{13}CO_2/^{12}CO_2$ = 1.08% ± 0.05% (corresponding to a δ-value of –23‰ ± 45‰), which is in good agreement with the natural abundance of 1.10574% [Hitran05]. Nevertheless the precision needs to be improved to be able to measure changes in the isotopic ratio in nature. one reason for the low precision and accuracy is related to the fact that the value of the line strength is not known precisely enough, e.g. in the Hitran database [Hitran05] there are only five digits listed. A second problem is that the wavelength steps are smaller than the resolution of the wavemeter (Burleigh WA-1000, resolution 1 pm) leading to mistakes in the wavelength scale. These problems could be solved by simultaneous measurements in a reference cell and by using an etalon for wavelength measurements.

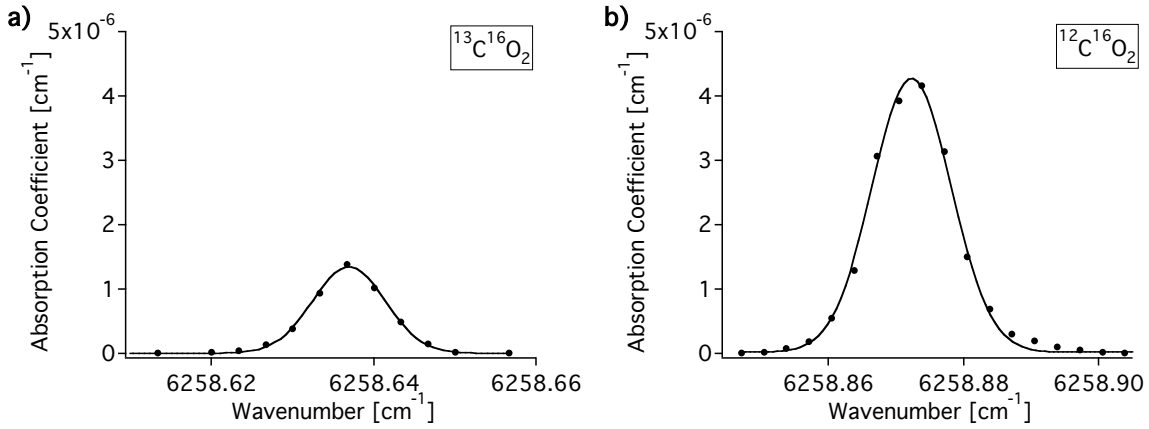

Figure 5: Measured absorption lines of CO_2 isotopes of 50% CO_2 in air at 5 mbar. The measured isotope ratio of $^{13}C^{16}O_2/^{12}C^{16}O_2$ = 1.08 ± 0.05% is in good agreement with the natural abundance of 1.10574%.

The detection limit is $6 \cdot 10^{-8}$ cm^{-1} (SNR = 3), this corresponds to a noise-equivalent detection sensitivity of $4.5 \cdot 10^{-8}$ $cm^{-1}Hz^{-1/2}$. Since the natural abundance of $^{13}CO_2$ is rather small, this detection limit would require measurements on gas concentration with ≥2% of CO_2.

2.4 Conclusion

A near infrared spectrometer based on cavity ringdown was tested for isotope measurements of carbon dioxide. The self-made cavity ringdown cell has a ringdown time constant of 25.2 ± 0.2 µs. An external cavity diode laser at 1.6 µm was used as a laser source. The isotope ratio $^{13}C/^{12}C$ of CO_2 with a concentration of 50% in air was determined by measuring the area under the chosen absorption lines at about 6259 cm^{-1}. An isotope ratio of 1.08% was obtained with a precision of ±0.05%. This is in good agreement with the natural abundance of 1.10574% [Hitran05] and corresponds to a δ-value of –23‰±45‰. The detection limit is

$6 \cdot 10^{-8}$ cm^{-1} (SNR = 3). This detection limit is higher than what is required for measurements at ambient CO_2 concentrations (380 ppm). The precision of the isotope ratio is not good enough to evaluate differences in nature, but for tracer applications of ^{13}C at high concentration, e.g. breath analysis, the detection limit and the precision are sufficient. The remaining measurements on other molecules and their isotopes – to be presented in the following chapters – have all been performed in the mid-infrared region where lower detection limits and better precision can be expected, yet on the cost of more sophisticated laser systems.

3. Mid-infrared laser source: Difference Frequency Generation

3.1 Introduction

The fundamental infrared (IR) or mid-IR region of the electromagnetic spectrum between, say, 3 and 20 μm is of special interest for many applications, notably molecular spectroscopy [Han94]. The reason is that most organic and inorganic molecules exhibit strong vibrational-rotational transitions in this wavelength region. The molecules of main interest in this work are CO_2, N_2O and CO. These molecules have their strongest absorption lines at around 4.3 μm, 4.6 μm and 4.7 μm, respectively, as shown in Figure 6. As the concentrations of these gases in ambient air are rather low, ppm or even ppb, and thus the concentrations of the less abundant isotopes are even lower, strong absorption lines are required. Therefore the mid-IR wavelength region is of preferable for isotope measurements.

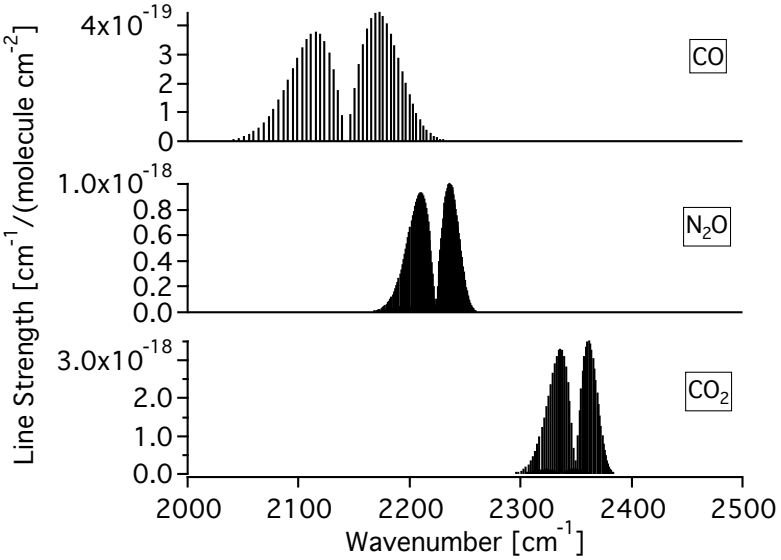

Figure 6: Absorption lines of CO, N_2O and CO_2 as a function of wavenumber in the mid-IR region [Hitran05].

Apart from an appropriate detection scheme, which enables sensitive absorption measurements, a good mid-infrared tunable laser source is a prerequisite for successful trace gas sensing and analysis. In addition to tunability, a narrow line width guarantees sufficient

specificity of detection of different isotopes of the same molecule. In the preferred mid-IR range, the choice of coherent sources is, however, rather limited. Table 3 lists tunable lasers with wavelengths longer than 3 μm. It essentially includes the conventional well-established line-tunable CO and CO_2 gas lasers, continuously tunable semiconductor lasers (lead salt diode and quantum cascade lasers), color center lasers, novel crystalline solid-state lasers and nonlinear optical devices (optical parametric oscillators and difference frequency generation sources).

Table 3: Tunable continuous-wave mid-IR laser sources with wavelengths ≥ 3 μm (RT: room temperature, LN_2: liquid nitrogen (77K), TE: thermoelectric cooling, SHG: second harmonic generation, QCL: quantum cascade laser, OPO: optical parametric oscillator, DFG: difference frequency generation).

Laser	**Wavelength [μm]**	**Tuning Characteristics**	**Power**	**Operation**
CO	5 – 6 (2.7 – 4, overtone)	Only line tunable	50 mW to Watts	LN_2 cooling, also ≤ 0°C
CO_2	9 – 11 (4.5–5.5, SHG)	Only line tunable	Watts	RT operation
Lead salt diode	4 – 30	~ cm^{-1} mode hop-free	< 0.1mW	Cryogenic cooling
QCL	4 – >24, THz	cm^{-1} to >100 cm^{-1} per device	mW	LN_2/TE cooling, also RT
Color center	1 – 3.3	~ 0.5 μm for single crystal	100 mW	LN_2 cooling
Solid State	2.2 – 3.1	~ 0.5 – 1 μm	≤1 W	RT operation
OPO	3 – 16	~ μm for specific setup	≤1 W	RT operation
DFG	3 – 16	~ μm for specific setup	μW to mW	RT operation

Recent progress both in solid state lasers and in quantum cascade lasers (QCLs) appears promising. Solid-state laser materials like Ce^{2+}:ZnSe or Fe^{2+}:ZnSe offer tuning ranges of 2.2–3.1 μm [Sor01] or 4–4.5 μm, respectively (though the latter only pulsed and with cryogenic cooling) [Ada99]. New developments in quantum cascade lasers (QCLs) equipped with external cavities yield a continuous tuning range of around 10% of the central wavelength and – at least partly – room-temperature continuous-wave operation [Fai06, Mau05].

The important region between 4 μm and 5 μm is accessible by lead salt diode lasers, quantum cascade lasers (QCL) and systems using nonlinear crystals like difference frequency

generation (DFG) or optical parametric oscillators (OPO) (see Table 3). Lead salt diode lasers need cryogenic cooling and the mode-hop free tuning range of these lasers is rather limited. Pulsed QCLs work at room temperature or with thermoelectric cooling but their frequency chirp often results in a line width larger than the absorption lines of the measured gases at a reduced pressure of 50 mbar, which is required in this experiment to differentiate between isotope lines. cw QCLs offer narrow line widths but at present commercially available devices still need cryogenic cooling for wavelengths shorter than 5 μm. Wavelength tuning of QCLs is done by temperature resulting in a limited tuning range of a few cm^{-1}. First devices operating at room temperature for wavelengths around 4 μm have been demonstrated recently and first developments of QCLs with external cavity, offering a larger tuning range of more than 100 cm^{-1}, have been reported for longer wavelengths in the last year [Fai06], but they just became commercially available very recently. OPOs offer high power and a large wavelength range but in order to achieve a small line width an etalon must be implemented, leading to a limited mode-hop free tuning range, especially when working computer controlled. As a result, our requirements of broad tunability in the 4–5 μm region, narrow line width and room-temperature operation are currently best met with a cw DFG system, yet on the cost of complexity and laser power.

In order to cover the wavelength range around 4 to 5 μm, to access N_2O, CO and CO_2, we built a DFG-system with a periodically poled $LiNbO_3$ crystal as nonlinear optical medium. The experimental arrangement of the DFG-source is depicted in Figure 13. It is based on a diode-pumped cw Nd:YAG laser (Innolight Mephisto, 2 Watt, 1064.5 nm) as signal source and a tunable cw external cavity diode laser (ECDL, Sacher TEC-120-850-150, 120 mW, 820 nm–875 nm) as pump laser. The two laser beams are mixed in an AR-coated periodically poled MgO-doped $LiNbO_3$ (MgO:PPLN) crystal (HC-Photonics, 50mm x 6 mm x 0.5 mm). After the crystal the near-IR light is blocked with a germanium filter. This source provides a continuous tuning range from 4.3 μm to 4.7 μm (idler) by using only one crystal grating with a period of 23.1 μm, when quasi-phase matching is realized by changing the crystal temperature between 30°C and 130°C. The DFG-system is discussed extensively in section 3.3.1. The information presented here (chapter 3) is essentially published in [Träg07].

3.2 Difference Frequency Generation (DFG)

Difference frequency generation (DFG) represents a nonlinear optical effect that is related to the nonlinear susceptibility of second order ($\chi^{(2)}$) of a material. Other related effects are second harmonic generation (SHG) and sum-frequency generation (SFG). Hence, DFG represents a three-beam interaction process that is mostly used to generate tunable coherent mid-infrared radiation although it has also been employed for THz -generation.

3.2.1 Birefringent and quasi phase matching and conversion efficiency

In difference frequency generation the light of two laser beams is mixed in a nonlinear crystal and light with a frequency of the difference of the two incident frequencies is generated. The generated frequency is given by energy conservation:

$$\hbar\omega_p - \hbar\omega_s = \hbar\omega_i \quad \rightarrow \quad \omega_i = \omega_p - \omega_s. \tag{21}$$

The laser with the highest frequency ω_p is called pump laser, while the second laser is called signal laser with the frequency ω_s. The generated idler beam has the lowest frequency ω_i. The phase matching condition is given by the conservation of momentum:

$$\Delta\vec{k} = \vec{k}_p - \vec{k}_s - \vec{k}_i = 0, \tag{22}$$

where $\Delta\vec{k}$ is the phase mismatch, and $\vec{k}_p$, $\vec{k}_s$, and $\vec{k}_i$ are the wavevectors of the pump, signal, and idler beam, respectively. In the case of collinear wave propagation the wavevectors can be replaced by $\left|\vec{k}\right| = nc/\lambda$ and Eq. (22) changes to:

$$\frac{n_p}{\lambda_p} - \frac{n_s}{\lambda_s} - \frac{n_i}{\lambda_i} = 0 \tag{23}$$

where n is the refractive index at the corresponding wavelength, λ is the wavelength with the subscripts p, s, and i corresponding to pump, signal and idler, respectively, and c is the speed of light in vacuum. Phase matching in a birefringent crystal can be achieved by i) angle tuning, ii) temperature tuning or iii) wavelength tuning (changing the wavelength of the pump and/or signal laser). The most common way to achieve phase matching with a birefringent crystal is realized by angle tuning, i.e. by rotating the crystal until the phase matching condition is fulfilled.

For infinite plane waves the idler intensity is given by [Bye77]:

$$I_i = 2\frac{\omega_i^2 d_{eff}^2 L^2 I_s I_p}{c^3 \varepsilon_0 n_p n_s n_i} \mathrm{sinc}^2\left(\frac{\Delta kL}{2}\right) \tag{24}$$

where d_{eff} is the effective nonlinear coefficient, L is the crystal length, I is the intensity of the laser beam for pump, signal and idler beams, respectively, ε_0 is the dielectric constant and Δk is the phase mismatch. Hence the idler intensity scales with the product of the incident intensities $I_s \cdot I_p$ and the square of the crystal length L^2. This is valid as long as there is no pump depletion and negligible walk-off between the beams. These effects limit the useful crystal length and they are discussed in more detail in section 3.2.2. The effective nonlinear coefficient d_{eff} describes the nonlinearity of the crystal seen by the incident light. It depends on the crystal structure, the direction of propagation and polarization of the light, and the nonlinear coefficients d_{ij} (Table 5) given by the tensor of the nonlinear susceptibility $\underline{\chi}^{(2)} = 2 \cdot \underline{d}$.

To achieve phase matching it is taken advantage of the different refractive index for ordinarily and extraordinarily polarized light. Depending on the combination of polarization

of the pump and signal beam and depending on positive or negative birefringence of the crystal, the phase matching is called type I, type II or type III as defined in Table 4. For quasi phase matching (QPM, see below) all three beams have the same polarization.

Table 4: Different phase matching types for DFG processes for positive and negative birefringent crystals. (PM: phase matching, e: extraordinarily polarized, o: ordinarily polarized, QPM: quasi phase matching)

PM type	Birefringence	Pump beam	Signal beam	Idler beam
I	positive	o	e	e
I	negative	e	o	o
II	positive	o	e	o
II	negative	e	o	e
III	positive	o	o	e
III	negative	e	e	o
QPM		e	e	e

Eq. (24) implies a possibility to generate light at the idler frequency without phase matching. I_i has a maximum at $\Delta k / 2 = m\pi / 2$ when m is a natural number. This yields the coherence length $l_c = \pi / \Delta k$ after which the newly generated idler light will interfere destructively with the light generated within the previous coherence length. Thus, after twice the coherence length all generated light is destroyed. This can be avoided by changing the polarization of the material by 180° after one or an odd multiple of the coherence length l_c because this will change the sign of the nonlinear coefficient, so the light will interfere constructively and a build-up of the generated light occurs as illustrated in Figure 7. This means that idler power can be generated without fulfilling the phase matching condition by using a periodically poled crystal. A quasi phase matching (QPM) condition can be written by using the grating period $\Lambda = 2l_c$ of the crystal:

$$\frac{n_p}{\lambda_p} - \frac{n_s}{\lambda_s} - \frac{n_i}{\lambda_i} - \frac{1}{\Lambda} = 0. \tag{25}$$

For the same parameters as for the bulk material less idler power will be generated for quasi phase matching than for birefringent phase matching by a factor of $(2/\pi)^2$. This factor is often included in d_{eff} by reducing its value by a factor $2/\pi$. Although the efficiency is lower than in the case of birefringent phase matching, often more power can be generated this way because the highest nonlinear coefficient can be used (e.g. for $LiNbO_3$ $d_{33} = -27$ pm/V (see Table 5) instead of $d_{22} = 3.07$ pm/V, which is relevant for birefringent phase matching of type II). Since all involved polarizations are the same (extraordinarily polarized, see Table 4), the walk-off angle is zero, therefore longer crystals can be used resulting in higher idler power. Furthermore, the selection of pump and signal wavelengths is rather flexible (see also section 3.3.1.1). However, the production of periodically poled crystals is difficult and not possible

for all crystals. Until now only $LiNbO_3$ (PPLN), $RbTiOAsO_4$ (PPRTA), $KTiOPO_4$ (PPKTP), $KTiOAsO_4$ (PPKTA) and $LiTaO_3$ (PPSLT) are commercially available periodically poled. These are ferroelectric crystals that are poled by applying a strong electrical field. Another, non-ferroelectric material is GaAs. In the beginning thin plates of GaAs with alternate polarization were stacked manually [Lal98]. Today orientation patterned GaAs, where the periodic poling is implemented during crystal growth [Bli06, Kuo06, Lev02], is becoming available.

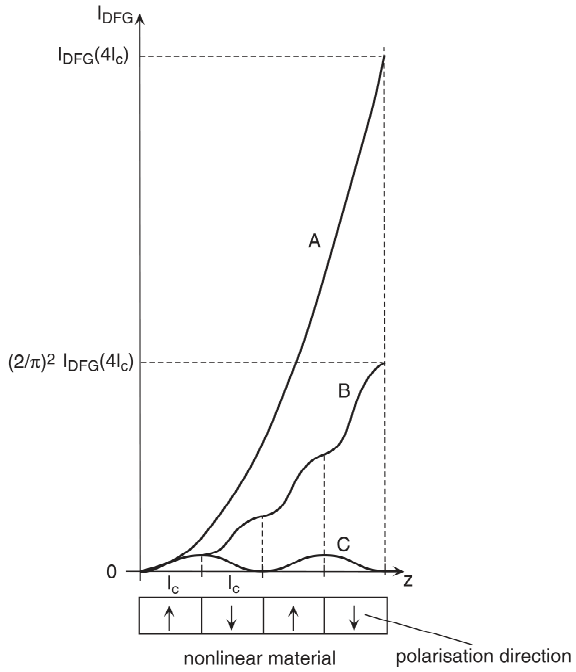

Figure 7: Idler power generation for phase matching condition $\Delta k = 0$ (A), non-phase matching condition $\Delta k \neq 0$ (C) and quasi phase matching condition in case of a periodically poled crystal (B). l_c denotes the coherence length [Fis03].

Eq. (24) is obtained under the assumption of infinite plane waves and no absorption. For Gaussian beams the relationship between idler power P_i, crystal length L, pump power P_p, signal power P_s, and absorption coefficient α is given by the following formula [Bor03, Boy68, Chu68]:

$$P_i = P_p P_s \frac{32\pi^2 d_{eff}^2 L}{\varepsilon_0 c n_i \lambda_i^2 (n_s \lambda_p + n_p \lambda_s)} \mathrm{h}(\xi, \sigma, \mu, \alpha, L). \tag{26}$$

The focusing function $\mathrm{h}(\xi, \sigma, \mu, \alpha, L)$ for diffraction limited Gaussian beams is given by:

$$\mathrm{h}\left(\xi, \sigma, \mu, \alpha, L\right) = \mathrm{Re}\left(\frac{e^{-\frac{\alpha L}{2}}}{4\xi} \int_{-\xi}^{\xi} \mathrm{d}\tau \int_{-\xi}^{\xi} \mathrm{d}\tau' \frac{e^{-i\sigma(\tau-\tau') + \frac{\alpha L}{4\xi}(\tau+\tau')}}{1 + \tau\tau' - i\frac{1+\mu^2}{1-\mu^2}(\tau - \tau')} \right), \tag{27}$$

where

$$\xi = \frac{L}{b} \tag{28}$$

$$\mu = \frac{k_s}{k_p} = \frac{n_s \lambda_p}{n_p \lambda_s} \tag{29}$$

$$\sigma = -\pi b \left(\frac{n_p}{\lambda_p} - \frac{n_s}{\lambda_s} - \frac{n_i}{\lambda_i} - \frac{1}{\Lambda} \right). \tag{30}$$

Here Λ is the grating period, and b is the confocal parameter of both pump and signal beam and is given by the minimal beam waist w: $b = k_p w_p^2 = k_s w_s^2$, σ describes the phase mismatch. The focusing function h(ξ, σ, μ, α, L) is discussed further below in chapter 3.3.1 (see also Figure 10, Figure 12 and Figure 14). These equations are valid for both bulk and periodically poled crystals, only d_{eff} changes by a factor 2/π compared to the case of a bulk crystal. The focusing function describes two competing effects: the efficiency is increased by focusing the beams because of higher intensities, but at the same time reduced because of less collinear wavevectors. A possibility to overcome this problem is to use waveguide periodically poled nonlinear crystals [Yan06]. Here the beams are confined in a waveguide in the crystal leading to collinear wavevectors and high intensities at the same time. With this technique continuous wave (cw) idler power in the milliwatt range can be achieved whereas with bulk or periodically poled crystals the cw idler power is normally in the microwatt range [Yan06].

The limes $\xi \to 0$ gives the result for the infinite plane wave because $b \to \infty$ for plane waves. In this case the focusing function reduces to $h \sim \xi$, resulting in an idler power proportional to L^2, as in the case for the plane waves (see Eq. 24).

An often used nonlinear crystal for difference frequency generation in the mid-infrared is $LiNbO_3$ because it can be made periodically poled (known as PPLN) and it has a large nonlinear coefficient. Its effective nonlinear coefficient is given by $d_{eff} = 2/\pi\, d_{33} M_{ij} = -14.4$ pm/V with $d_{33} = -27$ pm/V and $M_{ij} = 0.85$ for $LiNbO_3$ at 3.3 µm [Str02]. M_{ij} is the Miller factor that describes the dispersion of the nonlinear coefficient [Rob92, Cho72, Mil64]. The factor 2/π is needed when using quasi phase matching.

To calculate the phase matching condition the refractive index needs to be known for all wavelengths. It is given by the temperature dependent Sellmeier equation, e.g. for extraordinary polarized light in $LiNbO_3$ [Jun97]:

$$n_e^2 = 5.35583 + 4.629 \cdot 10^{-7} F + \frac{0.100473 + 3.862 \cdot 10^{-8} F}{\lambda^2 - (0.20692 - 0.89 \cdot 10^{-8} F)^2} + \frac{100 + 2.657 \cdot 10^{-5} F}{\lambda^2 - 11.34927^2} - 1.5334 \cdot 10^{-2} \lambda^2. \tag{31}$$

Here $F = (T–24.5)(T+570.82)$ describes the temperature dependence when T is the temperature in °Celsius and λ is the wavelength. This equation takes also the multiphonon absorption in account, which yields more accurate data for wavelength between 4 and 5 μm.

When choosing the grating period and the temperature of the crystal, the thermal expansion of the crystal also needs to be considered because it also influences the grating period although much less than the change of the refractive index with temperature. The thermal expansion is (at 25°C) $a_a = 15 \cdot 10^{-6}$/°C and $a_c = 7.5 \cdot 10^{-6}$/°C [Cry06a] with the index a and c corresponding to the crystal axes. The refractive index of $LiNbO_3$ strongly depends on its composition, the Sellmeier equation in (31) is for congruent composition, it will be different for stochiometric composition. Also the refractive index of MgO doped $LiNbO_3$, as often used in experiments, differs from that of ordinary $LiNbO_3$.

3.2.2 Nonlinear crystals

There are numerous crystals showing nonlinear optical effects, but only a few of them are useful for difference frequency generation. The crystal material needs to be transparent at all wavelengths of pump, signal and idler beams, it should have a high nonlinear coefficient and a high damage threshold. In some cases, e.g. strong dispersion and weak birefringence, phase matching is not possible. These requirements limit the choice of nonlinear crystals. The optical properties of some nonlinear crystals used in DFG-systems are listed in Table 5. Figure 8 shows the absolute nonlinear coefficient and the transparency range of selected crystals for comparison.

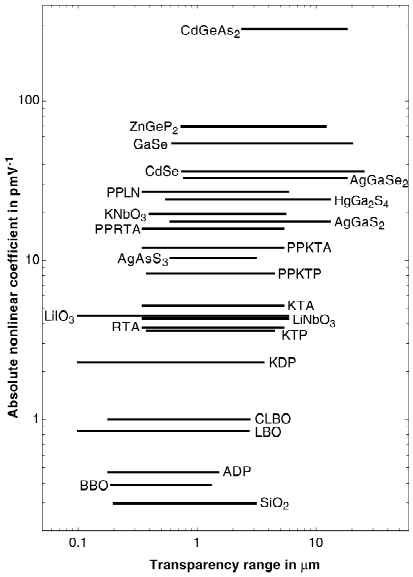

Figure 8: Transparency range of some selected nonlinear crystals used for mid-IR DFG generation as a function of the absolute value of the nonlinear coefficient. For the periodically poled materials (PPLN, PPRTA, PPKTA, PPKTP), the nonlinear coefficient d_{33} is given [Fis03].

Table 5: Nonlinear coefficients d_{ij} measured at wavelength λ_m, transparency range and approximate damage threshold for ns pulses of selected nonlinear optical crystals used in DFG.

Crystal	**Nonlinear coefficients [pm/V] [Sut03]**			**λ_m [μm]**	**Transparency range [μm] [Dmi99]**	**Damage threshold pulsed [MW/cm^2] [Dmi99, Gsä]**
$AgGaS_2$	d_{14}=57	d_{36}=20 d_{36}=23.6		10.6 1.064	0.46–13	25
$AgGaSe_2$	d_{36}=33			10.6	0.7–19	25
$CsTiOAsO_4$ (CTA)	d_{31}=2.1	d_{32}=3.4	d_{33}=18.1	1.064	0.35–5.3	500 [Dmi93]
GaAs	d_{14}=368.7	d_{36}=83 [Rob92]		10.6	1–17 [She97]	60 [She97]
GaSe	d_{22}=54.4			10.6	0.62–20	30
$KNbO_3$	d_{15}=–17.1 d_{32}=–15.8	d_{24}=–16.5 d_{33}=–27.4	d_{31}=–18.3	1.064	0.4–>4	180
$KTiOAsO_4$ (KTA)	d_{31}=4.2 d_{24}=2.9 [Rob92]	d_{32}=2.8	d_{33}=16.2	1.064	0.35–5.3	1200
$KTiOPO_4$ (KTP)	d_{15}=1.91 d_{32}=4.53	d_{24}=3.64 d_{33}=16.9	d_{31}=2.54	1.064	0.35–4.5	150
LiB_3O_5 (LBO)	d_{24}=0.74 d_{15}=1.03 d_{32}=–10	d_{31}=0.8–1.3 d_{24}=–0.94 d_{33}=–0.94	d_{33}=0 d_{31}=1.09	1.064 1.079	0.155–3.2	900
$LiIO_3$	d_{15}=–5.53	d_{31}=–7.11	d_{33}=–7.02	1.064	0.28–6	120
$LiInS_2$	d_{31}=9.9	d_{32}=8.6	d_{33}=15.8	10.6	0.35–12.5 [Mol06]	100 [Mol06]
$LiNbO_3$	d_{31}=–5.95 d_{15}=–5.95 [Cry06b]	d_{33}=–34.4 d_{33}=–27 [Rob92] d_{22}=3.07 [Cry06b]		1.064 –	0.4–5.5 [Cry06b]	300
$LiTaO_3$	d_{22}=2 [Mol06]	d_{31}=–1 [Mol06]	d_{33}=–21 [Mol06]	1.064	0.4–5 [Mol06]	–
$RbTiOAsO_4$ (RTA)	d_{31}=3.8	d_{32}=2.3	d_{33}=15.8	1.064	0.35–5.3 [Rai06]	400 [Rai06]
$RTiOPO_4$ (RTP)	d_{31}=4.1	d_{32}=3.3	d_{33}=17.1	1.064	0.35–4.3 [Rai06]	600 [Rai06]
$ZnGeP_2$	d_{36}=75	d_{14}=69 [Rob92]	d_{25}=69 [Rob92]	10.6	0.74–12	3

Table 6: Figure of Merit for different setups and crystals. (PP: periodically poled, OP: orientation patterned, ECDL: external cavity diode laser)

Crystal	**Pump laser**	**Signal laser**	**Idler wavelength [μm]**	**Idler Power [μW]**	**Figure of Merit [μW/(W²cm)]**
PPLN [Mad05]	ECDL 1030–1070 nm, with Yb-fiber amplifier 700 mW cw	Er-fiber laser 1545–1605 nm 5 W cw	2.9–3.5	cw 3500	200
PPLN [Fis02]	Nd:YAG 1064 nm pulsed 6 ns rep. 4–8 kHz 5 kW peak power	ECDL 1500–1600 nm 5mW cw	3.2–3.7	pulsed 2000	$4.4 \cdot 10^5$ (a) $4.4 \cdot 10^5$ (b)
PPLN [Bor03]	Diode laser master/slave 848–855 nm, 78 mW cw	Nd:YAG 1064 nm with Yb-fiber amplifier 5 W cw	4.15–4.35	cw 172	110
PPLN This setup (see section 3.3.1)	ECDL 850–870 nm 125 mW cw	Nd:YAG 1064 nm 2 W cw	4.3–4.7	cw 5 to 23	4 – 19
Waveguide PPLN [Yan06]	Diode laser 940 nm 17.5 mW cw	ECDL 1550 nm 20 mW cw	2.30–2.44	cw 400	$1.2 \cdot 10^5$
$AgGaS_2$ [Kho03]	ECDL 679–683 nm 40 mW cw	Diode laser 786–791 nm 20 mW cw	4.9–5.1	cw 0.1	31
PPKTP [Fra99]	Nd:YAG 1064 nm 222 mW cw	ECDL 1490–1568 nm with Er-fiber amplifier 34 mW cw	3.2–3.4	cw 0.170	22
PPKTA [Fra00]	Nd:YAG 1064 nm 117.2 mW cw	ECDL 1519 nm 17.4 mW cw	3.45–3.75	cw 0.140	70
PPRTA [Che01]	Ti:Al_2O_3 laser 710–720 nm 100 mW cw	Ti:Al_2O_3 laser 874–915 nm 200 mW cw	3.4–4.5	cw 10	250
OP GaAs [Lev02]	DFB diode laser 1306–1314 nm 1.5–3.3 mW cw	ECDL 1535–1570 nm with Er-fiber amplifier 1 Watt cw	7.9	cw 0.038	6
GaSe [Hsu06]	Nd:YAG 1064 nm pulsed 20ps 750 μJ, rep. 10 Hz	OPA 1100–4800 nm pulsed 5 ps, 35–50 μJ	2.4–28	pulsed 5 μJ	0.0041 (a) $2.1 \cdot 10^6$ (b)
$LiInS_2$ [Che05]	Ti:sapphire cw 700–810 nm	Ti:sapphire cw 800–900 nm	5.5 – 11.3	cw –	12.4

(a) FoM calculated with peak powers

(b) FoM calculated with average powers

For an easier comparison and characterization of crystals and DFG setups reported in the literature the following Figure of Merit (*FoM*) is useful:

$$FoM = \frac{P_i}{P_p P_s L}, \tag{32}$$

where P_i, P_p and P_s denote the power of the idler, pump and signal beams, respectively, and L is the crystal length. This way the comparison is independent of the chosen laser powers and crystal lengths. In Table 6 the Figure of Merit is listed for some representative setups involving various crystals and combinations of pump and signal lasers. Some of the systems generate a cw idler beam by using two cw lasers for pump and signal, other arrangements have a pulsed idler beam by using two pulsed lasers or one pulsed and one cw laser.

When choosing pump and signal laser several issues have to be considered. The laser wavelengths need to be within the transparency range of the crystal, and the wavelengths and the polarizations should be chosen so that phase matching is possible. Another important aspect is the laser power. As the conversion efficiency is rather low, high laser powers are preferred, but too high powers will damage the crystal, the surface of the crystal or the antireflection (AR) coating on the crystal. The AR-coating has often a lower damage threshold than the crystal itself. At high power of the pump laser other effects like optical parametric generation (OPG) or amplification (OPA) could become even stronger than the difference frequency generation resulting in an enlarged line width. If the signal laser has much more power than the pump laser, pump depletion might be a problem. Therefore pump and signal laser and nonlinear crystal have to be carefully matched. To estimate how low the signal power needs to be to avoid pump depletion, the following formula can be used:

$$\eta = \frac{I_i}{I_p} = \frac{8\pi^2 d_{eff}^2 L^2 I_s}{\varepsilon_0 n_p n_s n_i c \lambda_i^2} << 1, \tag{33}$$

where I_i, I_p, and I_s denote the idler, pump, and signal intensity, respectively, d_{eff} is the effective nonlinear coefficient, L is the crystal length, λ_i is the idler wavelength, ε_0 is the dielectric constant and n is the refractive index with the subscripts p, s, and i referring to pump, signal and idler, respectively. η is the conversion efficiency from pump beam to idler beam where $\eta = 1$ implies that 100% of the pump beam is converted to the idler beam. This case gives the nonlinear interaction length L_{nl}, one of several characteristic lengths of a DFG-system:

$$L_{nl} = \sqrt{\frac{\varepsilon_0 n_p n_s n_i c \lambda_i^2}{8\pi^2 d_{eff}^2 I_s}} \tag{34}$$

Crystal lengths longer than L_{nl} will not increase the idler power because of pump depletion. The aperture length L_{an} is the distance after which the beam is displaced by $2w_0$ because of walk-off effects and is given by:

$$L_{an} = \sqrt{\pi}\,\frac{w_0}{\rho_n}, \tag{35}$$

where w_0 is the minimal beam waist and ρ_n is the walk-off angle. The diffraction length L_{diff} is the length after which the beam diameter has increased by a factor of $\sqrt{2}$. Longer crystals will not increase the idler power. This effect can be calculated more precisely by using the focusing function in Eq. (27).

$$L_{diff} = 4kw_0^2 \tag{36}$$

For pulsed lasers the interaction length L_{qs} represents a further important issue:

$$L_{qs} = \sqrt{\pi}\tau\left(\frac{1}{v_{g1}} - \frac{1}{v_{g2}}\right)^{-1} \tag{37}$$

where τ is the pulse duration, v_{g1} and v_{g2} are the group velocities of the pump and the signal beams, respectively. L_{qs} describes the length after which the pulses from the two beams are separated by τ. Another characteristic length for pulsed lasers is the dispersion length L_{ds} given by

$$L_{ds} = \frac{\tau^2}{g_n}, \tag{38}$$

where g_n is the group velocity dispersion. This length describes the length after which the pulse duration has doubled. With these characteristic lengths first estimation for crystal lengths and pulse durations can be made.

3.3 DFG laser sources

The literature on DFG laser sources, new nonlinear crystal materials and applications has become extensive in recent years. By far most systems have been and still are developed in view of spectroscopic gas sensing and analysis. A recent overview of systems has been given in reference [Fis03]. In the following the DFG setup is described that has been developed for measurements on isotopes of trace gases.

3.3.1 Detailed discussion of a DFG laser source

Isotopic composition of trace gases like CO_2, CO or N_2O are of special interest in this work. These molecules with their isotopes exhibit strong absorption lines between 4.3 to 4.7 μm (see Figure 6 above). Therefore a continuous wave DFG source, which enables continuous tuning and narrow line width (to differentiate between isotopes), was implemented. In the following sections the theoretical calculations, the setup and the characterization of this system are described.

3.3.1.1 Calculations of optimal crystal length and beam parameter

For the wavelengths of interest we chose $LiNbO_3$ as nonlinear optical medium because it has a transmission range from 0.4 μm to 5.0 μm, a large nonlinear coefficient, and it can be produced periodically poled.

However, $LiNbO_3$ has an absorption band at 5 μm so the absorption between 4 μm and 5 μm cannot be neglected. The absorption coefficient at 4.3 μm is 0.25 cm^{-1}, at 4.6 μm it is 0.55 cm^{-1} and at 4.7 μm 0.75 cm^{-1} [Mye96]. There are other crystals that can be used at this wavelength, e.g. $AgGaS_2$ or $AgGaSe_2$ (Table 5), but they are not available periodically poled, so birefringent phase matching has to be used. This means the crystal length needs to be shorter because of walk-off effects and it is not possible to use the maximum nonlinear coefficient. Furthermore the alignment is more critical than with a periodically poled crystal. Finally, wavelength tuning is also an important issue. When working with such crystals, angle tuning has to be used which makes wavelength tuning over larger ranges more complicated. Often noncritical phase matching is used, because of its larger acceptance bandwidth but for a certain idler wavelength the pair of signal and pump wavelength is fixed in this case. This limits the choice of lasers and normally two diode lasers with lower power than other lasers have to be used.

In contrast, when using quasi phase matching, the phase matching is realized by choosing a grating period, so nearly every combination of lasers can be used (e.g. an external cavity diode laser (ECDL) that can be conveniently wavelength tuned, and a Nd:YAG laser with fixed wavelength that delivers high laser power). Phase matching is achieved by choosing the correct grating period Λ, which can be adjusted to other wavelengths by changing the temperature of the crystal because of the temperature dependence of the refractive index (see Eq. 31). When scanning the wavelength for spectroscopy the crystal temperature can be changed simultaneously to achieve mid-IR wavelength ranges of several hundred nm with only one grating period. Depending on wavelength the temperature acceptance bandwidth can be quite large (see Figure 15b below). Even larger wavelength ranges can be achieved by using a crystal with several gratings as shown in Figure 9. Typical grating periods for our wavelength range are approximately 23 μm. As a result it appears advantageous to use PPLN for the envisaged 4.3 – 4.7 μm wavelength range rather than a bulk $AgGaS_2$ or other crystal despite the non-negligible absorption of PPLN.

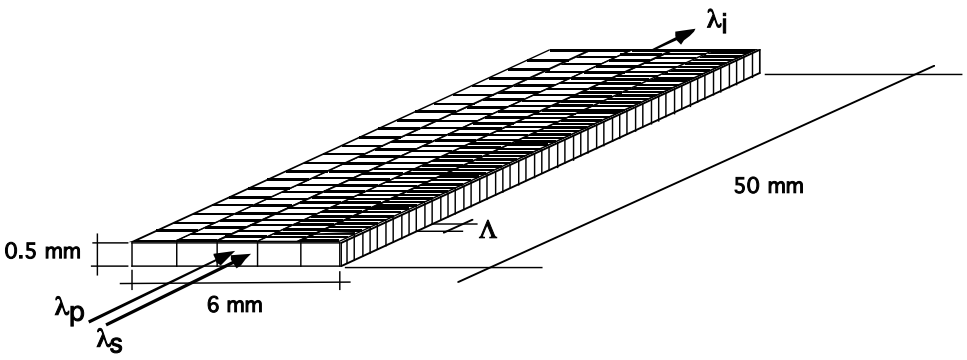

Figure 9: A periodically poled crystal with several gratings for different wavelengths.

According to Eq. (26) the idler power increases with the crystal length but also the absorption increases, therefore there is an optimum crystal length for this wavelength region. The maximum of the focusing function h(ξ, σ, μ, α, L) (Eq. 27) is not at $\sigma = 0$ but e.g. at $\sigma = 1.3$ for a pump wavelength of 863 nm, signal wavelength of 1064 nm and a crystal length of 5 cm (see Figure 14 below), so the maximum idler power is not obtained at perfect phase matching, but for a slightly different grating period. But to simplify the calculations σ was set to 0. The focusing function and hence the idler power has a clear maximum at about $\xi = 1.3$ (see Figure 10). It depends only slightly on wavelength and absorption. Therefore for a chosen crystal length L there is an optimal confocal parameter b.

When the idler power is plotted as a function of crystal length L and of the confocal parameter b, it can be seen that a long crystal combined with a large confocal parameter yields higher idler power (see Figure 11). But in a real experiment the confocal parameter is limited by the thickness of the crystal and longer crystals than 6 cm are not easily commercially available. The problem with longer crystals is that crystal defects are having too much influence. The thickness of the crystal is limited by the production process of the periodically poled grating. This is done by applying an electric field to change the orientation in the crystal, which requires very strong field strengths. This limits the thickness to 1 mm. Most crystals have a thickness of 0.5 mm, resulting in a better grating quality than for 1 mm thickness.

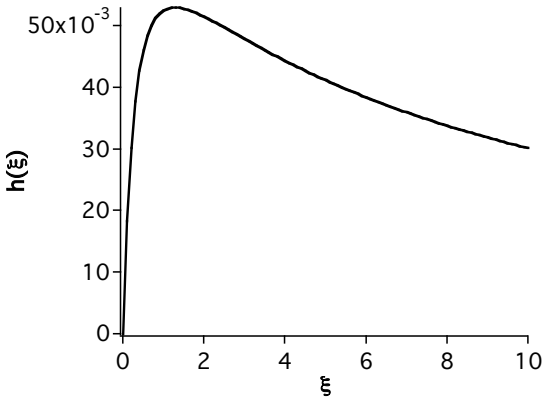

Figure 10: Focusing function h(ξ) versus ξ calculated for λ_p = 868 nm, λ_s = 1064 nm, α = 0.75 cm^{-1}, σ = 0, and L = 5 cm. The maximum is at ξ = 1.3 and for small ξ the focusing function h is proportional to ξ. The symbols are explained in Eqs. (26–30) above.

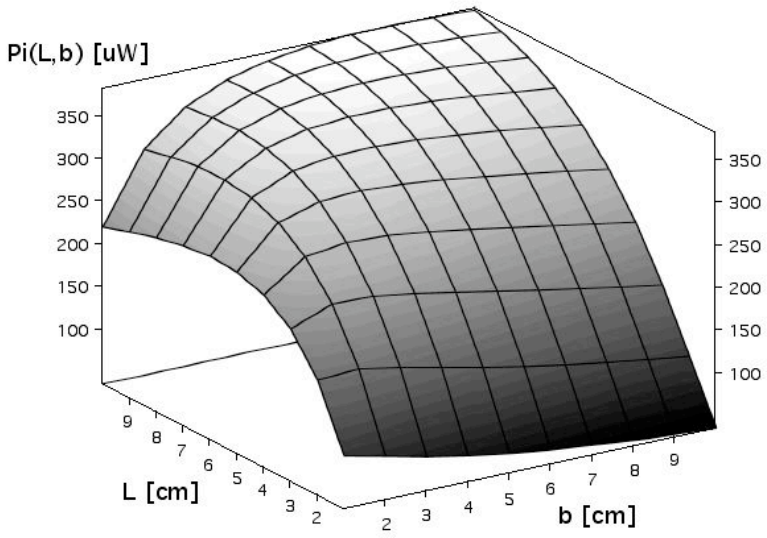

Figure 11: Idler power P_i versus crystal length L and confocal parameter b calculated at a pump wavelength of 853 nm. The idler power increases with simultaneously increasing crystal length L and confocal parameter b.

In Figure 12 it can be seen how the idler power changes for different crystal lengths. The calculations were made with σ = 0 and keeping ξ = L/b = 1.3 at the maximum. The result is that at λ_p = 853 nm (λ_s = 1064 nm, λ_i = 4.3 μm) the optimal length is longer than 10 cm, at λ_p = 863 nm (λ_i = 4.6 μm) it is 5.9 cm, and at λ_p = 868 nm (λ_i = 4.7 μm) it is 4.0 cm. We chose a crystal length of 5 cm implying b = 4 cm, which gives a minimal beam waist of 0.13 mm. Such a Gaussian beam propagates within the crystal over its whole length.

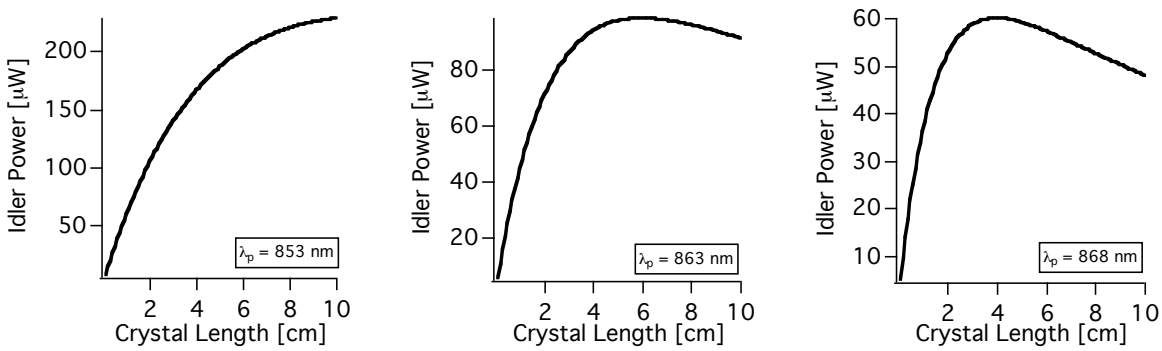

Figure 12: Idler power as a function of crystal length for pump wavelengths λ_p of 853 nm, 863 nm, and 868 nm. The signal laser is a Nd:YAG laser fixed at λ_s = 1064 nm. The calculations were made with $\sigma = 0$ and keeping $\xi = L/b = 1.3$ at the maximum. At 853 nm the ideal crystal length is longer than 10 cm, at 863 nm it is 5.9 cm, at 868 cm it is 4.0 cm.

Based on Eq. (26), an idler power between 55 μW to 170 μW is expected for a pump power of 150 mW, a signal power of 2 Watt and a crystal length of 5 cm.

3.3.1.2 Free-space setup and characterization

Our DFG system (Figure 13) consists of an external cavity diode laser (EDCL) as pump laser, a continuous wave Nd:YAG laser as signal laser and a MgO-doped periodically poled $LiNbO_3$ crystal (MgO:PPLN). The ECDL (Sacher TEC-120-850-150) has a power of 150 mW and a wavelength range between 820 nm and 875 nm. To cover the idler wavelength range from 4.3 μm to 4.7 μm, pump wavelengths from 852 nm to 868 nm are needed. The Nd:YAG laser (Innolight Mephisto) has a cw power of 2 Watts and a wavelength of 1064.5 nm. The MgO:PPLN crystal (HC-Photonics) is 5 cm long and 0.5 mm thick. It has several gratings with periods of 21.45, 22.00, 22.50, 23.10, and 23.65 μm, each with a width of 1.2 mm. For the wavelength of interest in this experiment, only the grating period of 23.1 μm is needed, it is quasi phase matched for the different wavelengths by changing the temperature from 30°C to 130°C. The crystal is antireflection-coated for the pump, signal and idler wavelengths.

The laser beams are focused by several lenses (including cylindrical lenses, not shown in Figure 13) so that the minimal beam radius is 0.13 mm within the crystal. The λ/4 and λ/2 plates are used to match the beam polarization for quasi phase matching in the PPLN crystal. A small part of the pump beam is directed to a wavemeter. The recorded pump wavelength then yields the idler wavelength. After the crystal a germanium filter is used to block the near infrared light.

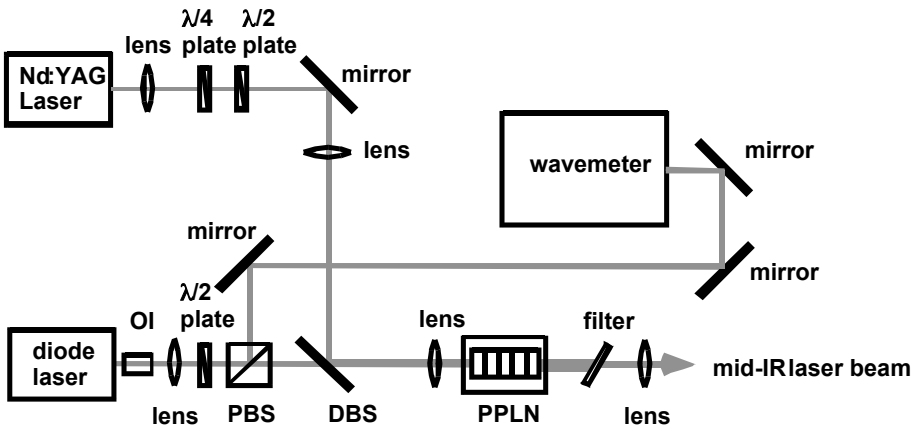

Figure 13: Setup for difference frequency generation. (OI: optical isolator, PBS: polarizing beam splitter, DBS: dichroic beam splitter, PPLN: periodically poled $LiNbO_3$)

We tested and characterized this DFG-system by focusing the mid-IR beam onto a detector (VIGO PDI-2TE-5, TE-cooled) and recording the signal with a lock-in amplifier with a time constant of 100 ms. For modulating the laser power with a frequency of 1.8 kHz, a chopper was placed after the Nd:YAG laser. To find the crystal temperature for phase matching, the temperature was increased in steps of 0.2°C or 0.5 °C while keeping the pump wavelength constant (see Figure 14).

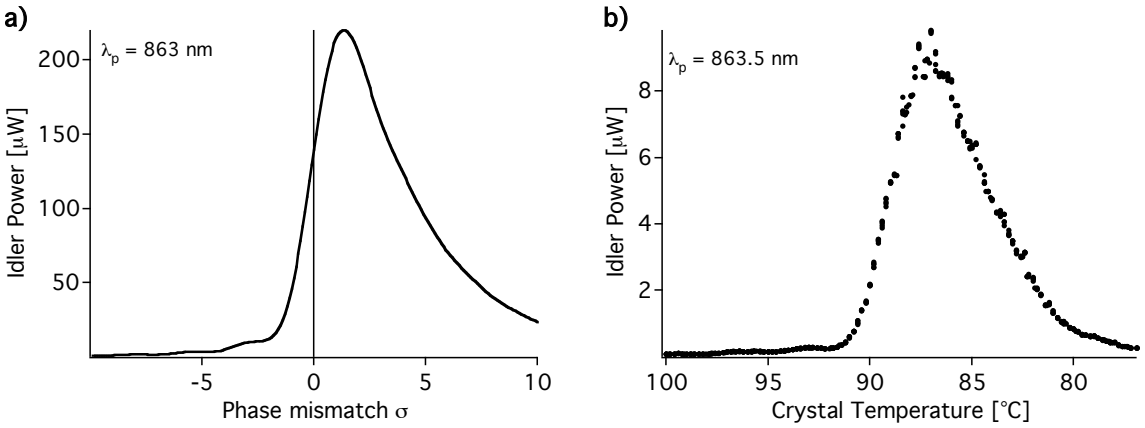

Figure 14: a) Idler power as a function of phase mismatch σ(see Eqs. 26 and 30), calculated for a pump wavelength of 863 nm, a signal wavelength of 1064 nm and a crystal length of 5 cm. b) Measured idler power as a function of crystal temperature corresponding to phase mismatch, at a wavelength of 863.5 nm and a crystal length of 5 cm. It can be seen that the measured and the calculated curve have a similar shape.

The temperature for phase matching is 6.6% to 11.2% higher than theoretically calculated (see Figure 15a) and the temperature acceptance bandwidth increases for longer wavelengths and is between 2.5°C and 3.7°C (see Figure 15b). The power of the cw mid-infrared beam amounts to 23 μW at 4.3 μm and 5 μW at 4.76 μm (Figure 15c). It decreases for increasing

wavelengths because of the crystal absorption near 5 μm. The generated idler power is about four to ten times lower than calculated, most probably because of imperfections in the crystal, its grating quality and non-Gaussian beam shape of the ECDL pump laser.

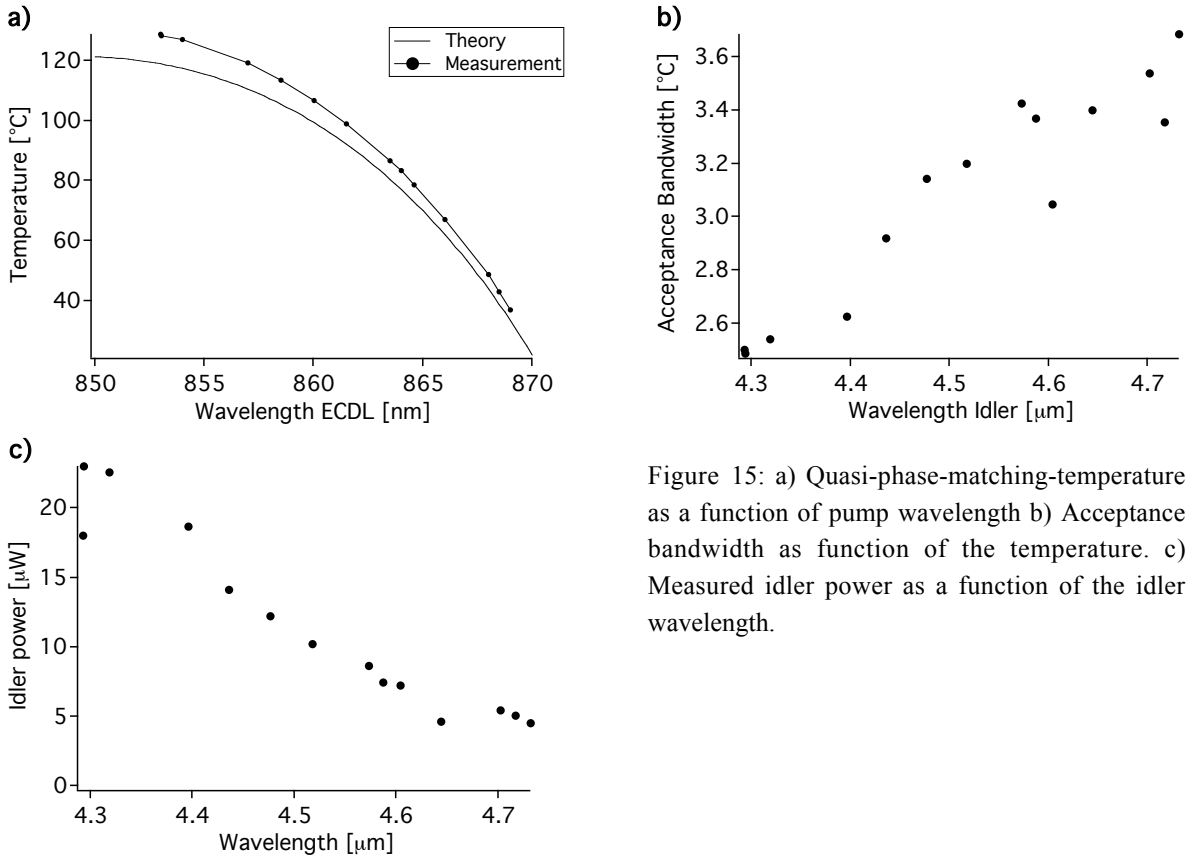

Figure 15: a) Quasi-phase-matching-temperature as a function of pump wavelength b) Acceptance bandwidth as function of the temperature. c) Measured idler power as a function of the idler wavelength.

For measurements of the isotopic composition of trace gases, the laser line width should be sufficiently narrow to clearly resolve adjacent molecular lines also when recorded at reduced gas pressure. The line width of our cw mid-IR source has been determined as approximately 1 MHz from the convolution of the line widths of the ECDL (1 MHz) and the Nd:YAG laser (100 kHz), and thus fulfills the requirements by far.

3.3.1.3 Fiber-coupled setup and characterization

In order to improve the robustness and the stability of the DFG-source and to reduce the system size, a fiber-coupled setup was built by coupling each laser beam into a fiber and using a wavelength division multiplexer (OZ-Optics, WDM-12P-820/1064-5/125-PPP) to combine the two beams into one fiber (see Figure 16 and Figure 17).

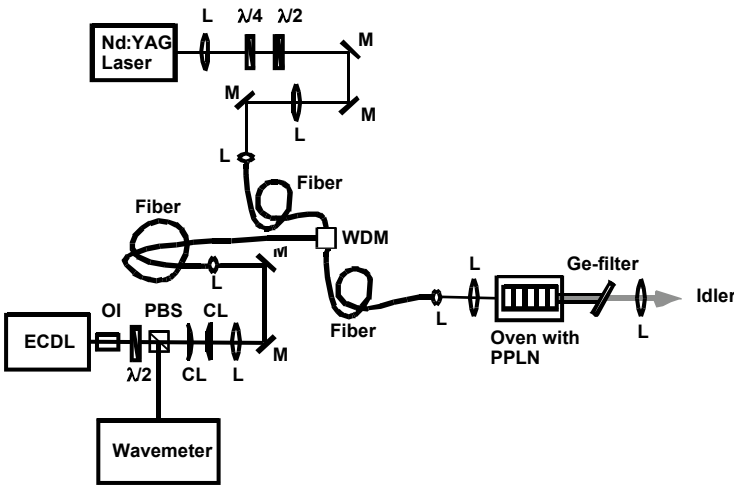

Figure 16: Setup of fiber-coupled DFG-system. (L: Lens, CL: Cylindrical lens, M: Mirror, OI: Optical isolator, PBS: Polarizing beam splitter, WDM: Wavelength division multiplexer, λ/2: Half-waveplate, λ/4: Quarter-waveplate)

Figure 17: Photo of the fiber combiner (wavelength division multiplexer). The fiber from the ECDL is connected to Port R (left), the fiber from the Nd:YAG laser is connected to Port T (top) and the combined beams are coupled into the fiber at Port 1 (bottom).

To achieve good coupling efficiency of the lasers to the fiber the beam shapes are matched to the coupling lens by using several lenses. Depending on beam quality, coupling efficiencies up to 50% for the diode laser and up to 80% for the Nd:YAG laser are expected. The losses in the WDM are specified to be smaller than 1dB, which correspond to a transmission of 80%. Therefore the expected total transmission is 40% for the ECDL and 64% for the Nd:YAG laser (Table 7). For the ECDL the output power is close to the calculated one. For the Nd:YAG laser the output power is only close to the calculation in the case of low incident power, for higher power the efficiency decreases, most probably due to changes in the beam shape at higher power.

Table 7: Efficiencies of fiber coupling and transmission through fiber combiner.

	ECDL	**Nd:YAG**	**Nd:YAG (low power)**
Incident power	90 mW	1000 mW	100 mW
Efficiency calculated	50% · 80% = 40%	80% · 80% = 64%	80% · 80% = 64%
Output power calculated	36 mW	640 mW	58 mW
Output power measured	33 mW	300 mW	50 mW
Efficiency measured	36%	36%	50%

The advantages of guiding both beams within the same fiber are manifold: The two beams always overlap, the output beams have Gaussian shapes, and a potential laser replacement requires its coupling into the fiber again and not a readjustment of the whole system. The disadvantage is that the power is lower due to coupling losses. Furthermore, as the two wavelengths see two different core diameters, the beam diameter, the divergency and the position of the minimal beam waist are different for the two beams after the fiber as illustrated in Figure 18.

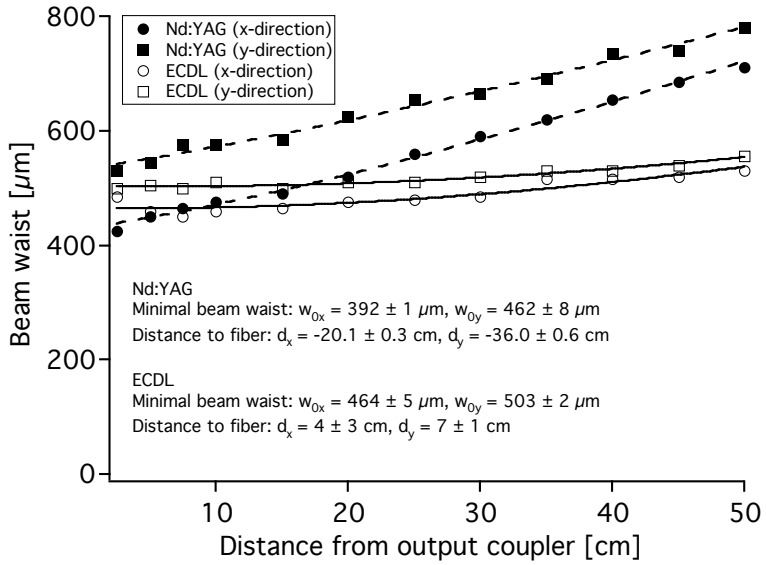

Figure 18: Measured beam shape of ECDL and Nd:YAG laser after the fiber. The beam parameters of the two laser beams are different because the different wavelengths see different core diameters of the fiber.

Because of this the two beams have different shapes when focused with a lens. Therefore two different lenses were tested to focus the beams into the nonlinear crystal. With the first lens the minimal beam waists had the optimum size as calculated but their positions were very different. With the second lens the minimal beam waists were smaller but at about the same position. The second setup generated more idler power than the first one (Table 8) and was therefore employed for the spectrometer.

Table 8: Influence on idler power of different lenses to focus pump and signal beams into the crystal.

Lens	Focal length [mm]	Minimal beam waist [μm]	Distance between waists [mm]	Detector signal (Idler) [mV]
1	190	149 (Nd:YAG) 103 (ECDL)	33	90±10
2	75	60 (Nd:YAG) 45 (ECDL)	11	120±10

At a wavelength of 4.6 μm an idler power of 0.26 μW is generated, which is much less than with the free space system (8 μW), but the Figure of Merit (Eq. 32) is the same for both systems. Important advantages of the fiber-coupled system are the more robust and compact setup and the Gaussian beam shape of the idler (Figure 19).

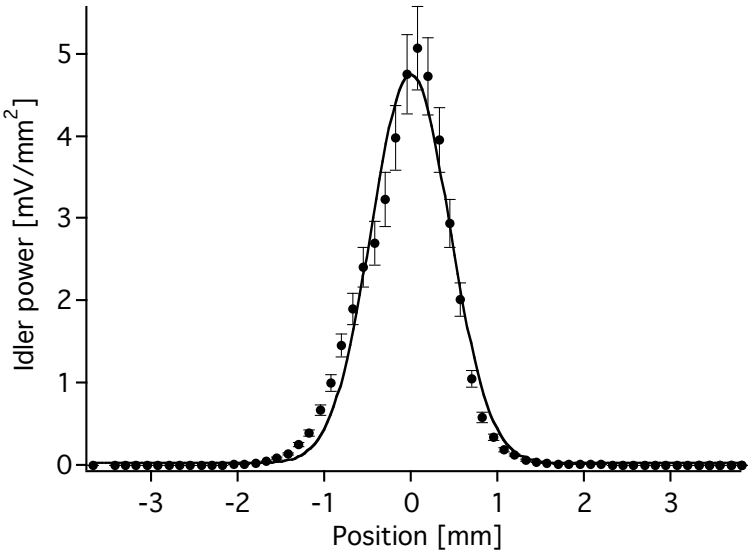

Figure 19: Beam shape of idler beam in the fiber-coupled system. A detector with a small area is scanned across the idler beam to measure the beam shape (dots). The solid line is a fit with a Gaussian function.

In contrast, the beam had sort of an M-shape in the free-space system (section 3.3.1.2), which made it difficult to focus the beam, e.g., on a detector. The spectrometer with the fiber-coupled DFG-system is more robust than the free-space device and has a much better day-to-day reproducibility. However, the precisions of the isotope-ratio measurements performed with both systems are comparable (Chapter 5.4).

3.4 Conclusion and Outlook

Tunable coherent sources in the mid-infrared range play an important role. This is manifested by the ever-growing number of publications. The development is fostered by numerous applications primarily in gas sensing. The requirements with respect to sensitive and selective monitoring devices with multi-component capability are manifold: access to a broad wavelength range, broad – preferentially continuous – wavelength tunability, narrow line width (i.e. much narrower than typical molecular absorption line widths), preferentially room-temperature (RT) or near-RT operation, compact and robust set-up for field applications. In this respect, DFG systems represent a very valuable choice. Since their first realization in 1974 [Pin74], DFG-based devices have reached a mature level. Today, their wavelength range can be chosen between, e.g., 2 μm and 19 μm only depending on available pump and signal sources and nonlinear crystals. The tuning of a DFG source is straightforward and continuous, and the wavelength generated can be accurately determined via the near-infrared input wavelengths. The line width is basically given by the line width of the pump and signal laser. This enables narrow mid-IR line widths as required for high-resolution spectroscopy. In contrast to alternative mid-IR sources, DFG systems are generally room-temperature devices except for the crystal that may require heating in small temperature-controlled oven. Line widths of continuous-wave DFG sources are in the MHz range, which makes them attractive for studies requiring high spectral resolution. DFG sources are rather low-power lasers with cw-powers in the μW to mW range. With fiber-amplifiers for the near-IR pump and signal sources, higher powers can be achieved if necessary [Mad05]. Recent developments in waveguide technology in PPLN [Yan06] or KTP appear particularly attractive in view of higher conversion efficiencies. Last but not least, a DFG system can be made compact in view of today's diode lasers and diode-pumped solid-state lasers used as pump and signal sources.

Both DFG-systems presented in this chapter, i.e. free-space and fiber-coupled devices, are laser sources that fulfill the requirements for spectroscopic isotope measurements. They are both continuously tunable between 4.3 μm to 4.7 μm, have a narrow line width (1 MHz), can easily be modulated and are accessible by computer control. The only drawback is the rather low power of 23 μW (free space, at 4.3 μm) and of 0.26 μW (fiber-coupled, at 4.6 μm), which is rather low for, e.g., cavity ringdown or photoacoustic measurements but sufficient for long-path direct measurements (see chapters 4 - 6). The lower power of the fiber-coupled system is due to fiber-coupling losses and lower power of pump and signal lasers caused by degradation, but the conversion efficiency is the same for both systems. The idler power is generally lower than predicted by theoretical calculations. This is most probably due to imperfections in the nonlinear crystal. The calculations were used to determine the optimal beam parameters and crystal length. Owing to the wavelength-dependent crystal absorption, there is an optimal crystal length, which was calculated to be about 5 cm. The beam shape of

the idler looks like an M-shape for the free space system, similar to the beam shape of the ECDL. In the fiber-coupled system the idler has a Gaussian beam shape like the pump and signal beams exiting the fiber. The fiber-coupled system is also more robust and compact than the free space system, which is important for future field measurements.

Future developments in several areas such as availability of new nonlinear crystal materials including organic media with better quality and higher nonlinear, quasi-phase matching for additional crystal materials, waveguide technology, etc. will contribute to improve the performance of DFG devices, enhance their distribution and increase their role as attractive sources for spectroscopic applications.

4. Spectroscopic considerations on isotope ratio measurements

4.1 Introduction

As discussed in chapter 2, molecular absorption is generally stronger in the mid-infrared than in the near-infrared. This also applies to the molecules of interest (CO_2, CO, N_2O) where absorption enhancement amounts to typically five orders of magnitude (see Figure 1). As presented in chapter 3 difference frequency generation was employed as a laser source with a tuning range covering the strongest absorption lines of these molecules and their isotopes. The drawback of the DFG laser source is its rather low power (μW-range), which impedes its use in combination with cavity ringdown (see chapter 2) or photoacoustic (PA) detection, which both require high laser power. A second aspect is that the measurements are done at low pressure (50 mbar) to avoid overlapping of the absorption lines, which again renders PA measurements less favorable as the PA signal decreases strongly at such low pressure [Cal99]. Direct absorption spectroscopy and wavelength modulation in combination with a multipass cell are detection methods that do not need high laser power but still yield high sensitivities. In this chapter these two techniques that have both been applied in our studies will be described and the different types of multipass cells be discussed. Further, the selection of the absorption lines is explained and the different experimental arrangements are shown.

4.2 Direct transmission spectroscopy

The most straightforward method of spectroscopic gas measurements is direct transmission spectroscopy. In this case the light is directed through a gas sample to a detector. When the wavelength is scanned the detector signal will vary because of the changing transmission of the light due to the absorption lines of the gases. The transmission $T(\lambda,L)$ through the gas sample is given by the Beer-Lambert law [Dem00]:

$$T(\lambda,L)=\frac{I(\lambda,L)}{I_0}=\exp(-\alpha(\lambda)L)=\exp(-N\sigma(\lambda)L) \tag{39}$$

where $I(\lambda,L)$ is the intensity of the transmitted light with wavelength λ after an absorption path length L, I_0 is the intensity of the incoming light, $\alpha(\lambda)$ is the absorption coefficient at the

wavelength λ, N is the number of absorbing molecules per volume and $\sigma(\lambda)$ is the molecular absorption cross section. As the laser power I_0 usually is not stable, a beam splitter is placed in front of the gas sample to direct a part of the light to a second detector to normalize the measured transmission.

The shape of the absorption line depends on the broadening mechanisms, e.g. Doppler broadening results in a Gaussian line shape whereas pressure broadening yields a Lorentzian line shape. At a gas pressure of 50 mbar these two effects are of the same order of magnitude therefore the total broadening results in a Voigt profile $V(\nu)$, which is a convolution between a Lorentzian curve $L(\nu)$ and a Gaussian curve $G(\nu)$:

$$V(\nu) = \int_0^\infty G(\nu')L(\nu - \nu_0 - \nu')\mathrm{d}\nu' \tag{40}$$

where ν_0 is the line center. The line strength or the spectral line intensity S_{ij} of a transition is independent of the broadening mechanisms and is given by [Dem00, Hitran96]:

$$S_{ij} = \frac{h\nu_{ij}}{c}\frac{n_i}{N}\left(1 - \frac{g_i n_j}{g_j n_i}\right)B_{ij} = \int_0^\infty \sigma_{ij}(\nu)\mathrm{d}\nu \tag{41}$$

where B_{ij} is the Einstein coefficient for induced absorption, n_i and n_j are the populations of the lower and upper states, respectively, g_i and g_j are the state statistical weights, and N is the molecular number density. S_{ij} in the units of $\mathrm{cm}^{-1}/(\mathrm{molecule}\cdot\mathrm{cm}^{-2})$ denotes the line strength for a single molecule. If the line strength is known, the molecular number density in a gas sample can be obtained by measuring the transmission, calculating the absorption coefficient $\alpha(\nu)$ from this measurement, and dividing the area under this curve by the line strength.

$$N = \frac{1}{S_{ij}}\int \alpha(\nu)\mathrm{d}\nu \tag{42}$$

The sensitivity and the precision of the measurement are mainly limited by the detector noise and fringes due to etalon effects. The latter can be reduced by using wedged windows and beam splitters. The wavelength dependent transmission of the system can also be corrected by dividing the measured spectrum by a background spectrum measured without absorbing gas. Therefore it is crucial to build a stable system with reproducible background. Low noise detectors should be used to be able to measure small changes in the transmission. An increase of the light intensity does not increase the detection limit as long as the light intensity is well above the noise level of the detector. A possibility to increase the detection limit is to modulate the light with a chopper at a certain frequency and filter out all the other frequencies of the detector signal by using a lock-in amplifier. Other possibilities to improve the sensitivity are the use of long path lengths L and of wavelengths λ with strong molecular absorption.

4.3 Frequency modulation and wavelength modulation

In direct absorption spectroscopy small changes in a large signal need to be observed (see Eq. 39) and a background needs to be subtracted. To avoid these problems other measurement techniques like frequency modulation or wavelength modulation can be used. For this the laser frequency ν is modulated at a modulation frequency ω_m with a modulation amplitude M. If the modulation frequency is high, above, say 100 MHz, and the amplitude is small it is called frequency modulation, and in the case of low modulation frequency (kHz range) and large amplitude it is called wavelength modulation. The transmitted intensity I_T trough the gas sample can be written as [App7]:

$$I_T(\nu_t) = I_T(\nu + M\sin\omega_m t) \tag{43}$$

When the wavelength is now scanned across an absorption line, the wavelength modulation is converted into an amplitude modulation at the same frequency, as shown in Figure 20. When scanning across the absorption line the amount of amplitude modulation varies with the slope of the measured absorption feature. The result of a frequency and phase sensitive detection is a curve that is similar to the derivative of the absorption line.

If the modulation amplitude M and the modulation frequency ω_m are much smaller than the spectral width Γ of the absorption line, which is the case for frequency modulation, then I_T can be expanded in a Taylor series:

$$\begin{aligned} I_T(\nu + M\sin\omega_m t) = I_T(\nu) + (M\sin\omega_m t)\frac{dI_T(\nu)}{d\nu} + \left(\frac{M^2\sin^2\omega_m t}{2!}\right)\frac{d^2I_T(\nu)}{d\nu^2} + \\ \left(\frac{M^3\sin^3\omega_m t}{3!}\right)\frac{d^3I_T(\nu)}{d\nu^3} + \ldots \end{aligned} \tag{44}$$

and combining the terms gives:

$$\begin{aligned} I_T(\nu + M\sin\omega_m t) = \left[I_T(\nu) + \frac{M^2}{4}\frac{d^2I_T(\nu)}{d\nu^2} + \ldots\right] + \\ \sin\omega_m t\left[M\frac{dI_T(\nu)}{d\nu} + \frac{M^3}{8}\frac{d^3I_T(\nu)}{d\nu^3} + \ldots\right] + \\ \cos 2\omega_m t\left[-\frac{\omega_m^{\,2}}{4}\frac{d^2I_T(\nu)}{d\nu^2} + \ldots\right] + \ldots \end{aligned} \tag{45}$$

The transmitted intensity contains a DC term, a term oscillating a frequency ω_m, a term oscillating at $2\omega_m$, and so on. If a phase sensitive measurement at the frequency ω_m is performed, e.g. by using a lock-in amplifier, the term with $\sin\omega_m t$ can be extracted. In the case of M small the coefficient of this term is essentially M multiplied with the first derivative of the transmitted intensity dI/dν.

$$S(\nu) \propto M\frac{dI_T(\nu)}{d\nu} \tag{46}$$

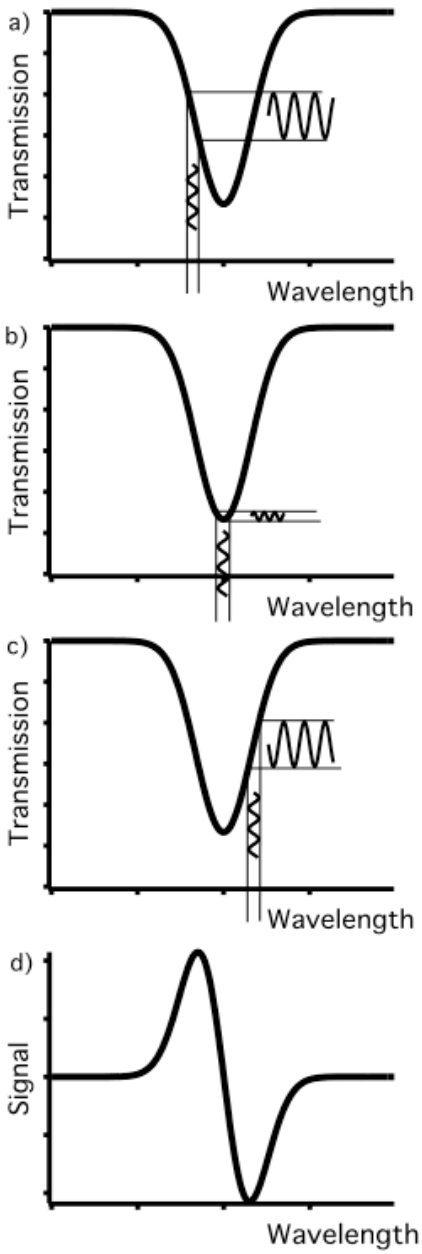

Figure 20: a) Frequency modulation (FM) spectroscopy: As the wavelength is scanned across the absorption line, the frequency modulation is converted into amplitude modulation (AM), resulting in a modulation of the optical absorption of a sample at the same frequency. b) and c) As the scan is continued across the absorption profile the amount of FM to AM conversion varies. d) The result of a frequency and phase sensitive detection is a curve that is similar to the derivative of the absorption line. [App7]

This means the detected signal increases with larger modulation amplitudes. But for large modulation amplitudes Eq. (46) is no longer valid and a more extended calculation of the detector signal must be done. The electric field of the light with a sinusoidal modulated wavelength is given by [Sup94]:

$$E(t) = E_0 \exp\left[i\left(\omega_0 t + M \sin \omega_m t\right)\right] = E_0 \exp\left(i\omega_0 t\right) \sum_{n=-\infty}^{+\infty} J_n(M) \exp\left(in\omega_m t\right) \qquad (47)$$

where the expansion into a series of nth-order Bessel functions J_n characterizes the frequency components of the modulated light spectrum. This means the modulation creates sidebands at $\omega_{\pm n} = \omega_0 \pm n\omega_m$ and their strength is given by the corresponding Bessel function J_n. For small M, which is the case for frequency modulation, it is $J_n(M) = M^n / 2^n 2!$, which means that only the terms $n = 0$ and $n = \pm 1$ need to be considered. This shows that the light spectrum essentially consists of the strong carrier and only one sideband per side at $\omega_{\pm 1} = \omega_0 \pm \omega_m$.

If now the modulation amplitude M is increased, more and stronger sidebands are generated. Therefore the signal measured at $\omega_{\pm n} = \omega_0 \pm n\omega_m$ does not anymore correspond to the derivative of nth order but it is broader and changes its shape. In Figure 21 measurements of N_2O absorption lines are shown for different modulation depths. The result of the smallest modulation amplitude is about the same as the derivative of the absorption lines (absolute values) calculated with Molspec, but for the largest M the measured curve on top is very different from the calculated one at the bottom.

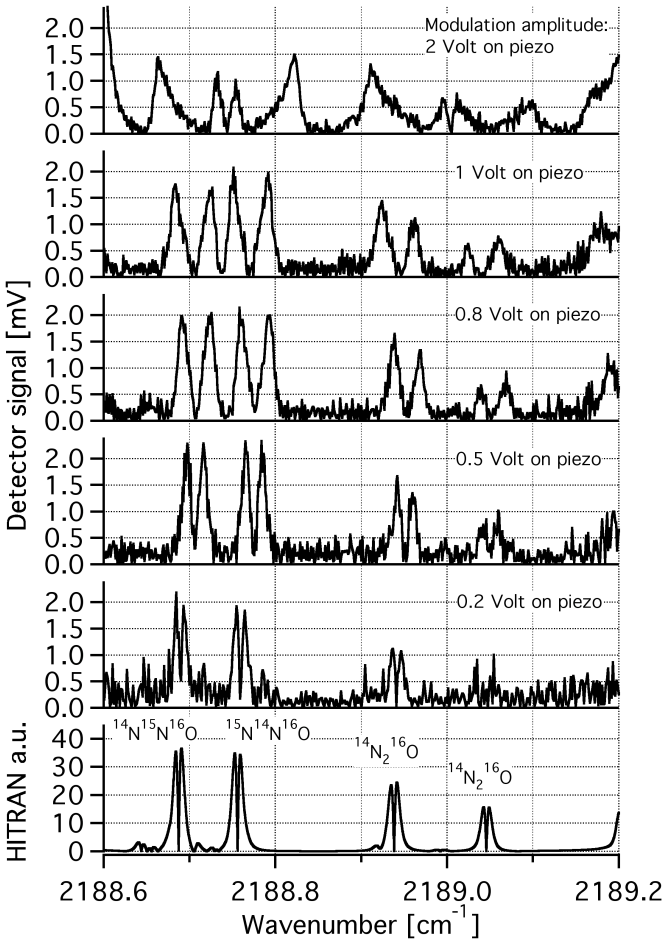

Figure 21: Wavelength modulation with different modulation depth for N_2O isotopes. The bottom curve represents the absolute value of the derivative of the calculated absorption.

For small modulation amplitudes M, the signal increases with M but for large M the signal decreases again. The optimum M depends on many parameters, e.g. on the shape of the absorption line and on the choice of the nth harmonic to detect. Silver [Sil92] calculated the optimum modulation amplitude for Gaussian and Lorentzian line shapes for different harmonics. For $n = 1$ it is $M = 1.6$ (Gaussian) and $M = 2.0$ (Lorentzian), for $n = 2$ it is $M = 2.1$ (Gaussian) and $M = 2.2$ (Lorentzian).

The instantaneous detector signal at time t is given by the transmission $T(\nu)$ at the instantaneous frequency $\nu(t) = \nu_0 + M\sin(\omega_m t)$ and the laser power P_0. A lock-in amplifier extracts the Fourier coefficient of the nth harmonic, which gives a measured signal of [Klu01, Tom06]:

$$S_n(\nu) = \eta \frac{2-\delta_{n0}}{\tau} \int_0^{\tau} P_0 T(\nu_0 + M\sin(\omega_m t))\cos(n\omega_m t - \theta_n)dt \tag{48}$$

where τ is an integration time that is $>>\omega_m^{-1}$, θ_n is the phase between the detector signal and lock-in reference, η is an instrument factor and δ_{n0} is the Kronecker delta. The transmission $T(\nu)$ is given by the Beer-Lambert law by $T(\nu) = T_0\exp(-\alpha(\nu)L)$ where $\alpha(\nu) = \alpha_0 g(\nu) = N\sigma(\nu)$ (Eq. 39) is the absorption coefficient with $g(\nu)$ as normalized line shape, and T_0 is the transmission of the whole system without absorbing gas. If the absorption is small then the transmission is given by $T(\nu) = T_0(1-\alpha(\nu)L)$ and the lock-in signal becomes:

$$\begin{aligned} S_n(\nu) &= \eta \frac{2-\delta_{n0}}{\tau} \int_0^{\tau} P_0 T_0 \exp(-\alpha(\nu_0 + M\sin(\omega_m t))L)\cos(n\omega_m t - \theta_n)\mathrm{d}t \\ &\approx -\eta \frac{2-\delta_{n0}}{\tau} \int_0^{\tau} P_0 T_0 \alpha(\nu_0 + M\sin(\omega_m t))L\cos(n\omega_m t - \theta_n)\mathrm{d}t \\ &\propto N\tilde{\sigma}_n(\nu) \end{aligned} \tag{49}$$

where $\tilde{\sigma}_n(\nu)$ is the Fourier coefficient of the absorption cross-section $\sigma(\nu_0 + M\sin(\omega_m t))$. This means that in the case of small absorption is the measured signal proportional to the molecular number density N.

This Eq. (49) is valid as long as there is no laser power modulation associated with the wavelength modulation. Often the wavelength is modulated by modulating the injection current of the laser diode, which results in laser power modulation. In this case the detector signal from the lock-in amplifiers also contains other Fourier components from lower and higher harmonics (for more detail see [Klu01, Tom06]). But in this work the wavelength is modulated by turning the grating of the external cavity diode laser (ECDL) with a piezo, resulting in much smaller power modulation. Therefore any effects of amplitude modulation are not taken into account in the evaluation of the measurements.

4.4 Multipass cells

When considering the Beer-Lambert law (Eq. 39) there are two possibilities to increase the change in transmission: Firstly the absorption coefficient can be increased by choosing strong absorption lines and secondly the path length can be increased. One often employed possibility for the latter are multipass cells, where the light beam is reflected by mirrors in the sample cell, resulting in a large number of passes through the gas. Thus, a long path length is obtained by keeping the cell volume small at the same time. The most used types of multipass cells are the White cell [Whi42], the Herriott cell [Her64, Her65] and the astigmatic Herriott cell [Man95].

4.4.1 White cell

The *White cell* consists of three mirrors with the same radius of curvature. Two mirrors A and A' are close together at one end of the absorption cell and the third mirror B is at the other end. The center of curvature of the mirrors A and A' is at the surface of mirror B and the center of curvature of mirror B is in the middle between mirror A and A' (Figure 22).

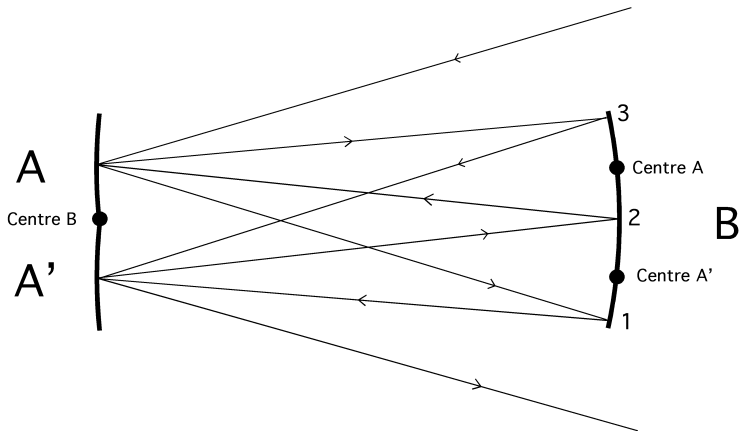

Figure 22: Setup of a White cell. It consists of three mirrors A, A' and B with the same radius of curvature arranged as shown in the figure. The light enters the cell close to mirror B, is then focused from mirror A onto mirror B (spot 1), propagates to mirror A' and is focused again onto mirror B (spot 2), from where it propagates again to mirror A and so on until the spot position after leaving mirror A' is outside of mirror B and the beam is coupled out.

In such a system all the light leaving any point on mirror A is brought to a focus by mirror B at the corresponding point on mirror A', and all the light leaving this point on mirror A' is focused back again to the original point on A. Similarly, all the light leaving any point on B and going to either A or A' is focused back to a new point on B that is somewhat offset to one side of the original one. So if light enters through a slit close to one end of B so that it

propagates to A then it returns back to B, then travels to A', back to B, then again to A and so on until the beam leaving A' exits close to the edge of mirror B. The number of passes is always a multiple of four and is determined by the separation of the centers of curvature of the mirrors A and A' compared to the diameter of the mirror B [Whi42]. The number of passes is limited by the spot diameter on mirror B, as it should be smaller than the spot separation in order to not couple out light from a previous spot. The advantage of this cell is its simple design and that it can handle strongly diverging light. The disadvantage is its relatively large volume-to-path length ratio compared to the Herriott cell type.

4.4.2 Herriott cell

A *Herriott cell* is an off-axis resonator, it consists of two spherical mirrors separated by a certain distance L and the beam is injected so that it follows a path, which fulfills a reentrance condition. The position (x_j, y_j) of the jth spot is given by [Her64, Her65]:

$$x_j = X_0 \sin(j\theta) \quad \text{and} \quad y_j = Y_0 \sin(j\theta + \varphi) \tag{50}$$

$$\cos\theta = 1 - (L/R), \tag{51}$$

where R is the curvature radius of the mirror. If $X_0 = Y_0$ and $\varphi = \pm\pi/2$ the spot pattern on the mirrors is circular, otherwise it is elliptical (see Figure 23). The reentrance condition is fulfilled when the spot after N passes is at the same position as in the beginning:

$$x_0 = x_N, y_0 = y_N \quad \Rightarrow \quad N\theta = 2\pi M, \quad M \in \mathrm{Z} \tag{52}$$

The number of passes N is determined by the mirror curvature radius R and the separation distance L (Eqs. 51 and 52). The maximum number of passes is given by the spot diameter and the spot separation on the mirror, as all the previous spots should not exit partially through the entrance hole. The angular separation of the neighboring spots on one mirror is 2θ. This multipass cell type has a better path length-to-volume ratio than the White cell but it is still worse than the astigmatic Herriott cell.

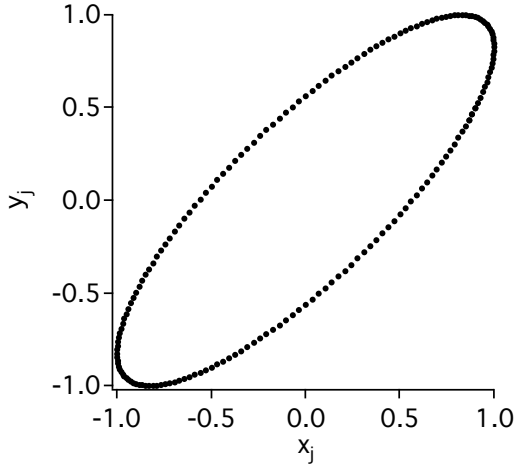

Figure 23: Spot pattern on the mirrors of a Herriott cell. The spots of both mirrors are shown in the same graph.

In an *astigmatic Herriott cell* the mirrors are slightly astigmatic, i.e. they have different curvature radii R_x and R_y in horizontal and vertical direction. Therefore the spot pattern is not anymore circular but forms a Lissajous pattern. The advantage is that this cell has a better path length-to-cell volume ratio than the normal Herriott cell or the White cell. The difference in curvature radius between R_x and R_y is about 10%. The mirrors are separated by nearly their radius of curvature and the optical beam is coupled into the cell through a hole in the center of the front mirror. With the right beam direction it travels along a reentrance path in the cell and leaves the cell after a finite number of passes through the same hole. The beam creates a Lissajous pattern that is sinusoidal in the x and y direction, but has different frequencies in the two directions [Man95]. The coordinates of the *j*th spot are given by:

$$x_j = X_0 \sin(j\theta_x) \quad \text{and} \quad y_j = Y_0 \sin(j\theta_y) \tag{53}$$

$$\theta_x = \cos^{-1}\left(1 - \frac{L}{R_x}\right) \quad \text{and} \quad \theta_y = \cos^{-1}\left(1 - \frac{L}{R_y}\right) \tag{54}$$

X_0 and Y_0 define the size of the spot pattern on the mirror. The parameter j varies from 1 to N. In a reentrance path with N passes the beam must end in the center of the mirror again, where the output hole is located. In order to leave the cell through the same mirror as entered, N must be even.

$$(x_0, y_0) = (x_N, y_N) = (0,0) \quad \Rightarrow \quad \theta_x = \pi M_x / N \quad \text{and} \quad \theta_y = \pi M_y / N \tag{55}$$

M_x and M_y are integers that define the shape of the beam spot pattern. There are a large number of spot patterns as many combinations of N, M_x and M_y can be found. For these patterns in order to be unique there must be no common factors other than 2 in this set of integers. Otherwise the pattern is degenerated and the reentrance condition is fulfilled for a lower number of passes than N. A common factor 2 is possible because there are two mirrors and in this case the beam hits the center of the second mirror without an output hole (see Figure 25).

To find an optimal pattern several aspects have to be considered. First of all a long path length is desired so N should be a large number. Also a good distribution and a good separation of the spots are required to avoid overlapping of spots, which leads to interference effects. It also allows a larger entrance hole (Figure 24), whose size is limited by the distance to the closest spot. Another important point is that the pattern should be relatively insensitive to mirror misalignment.

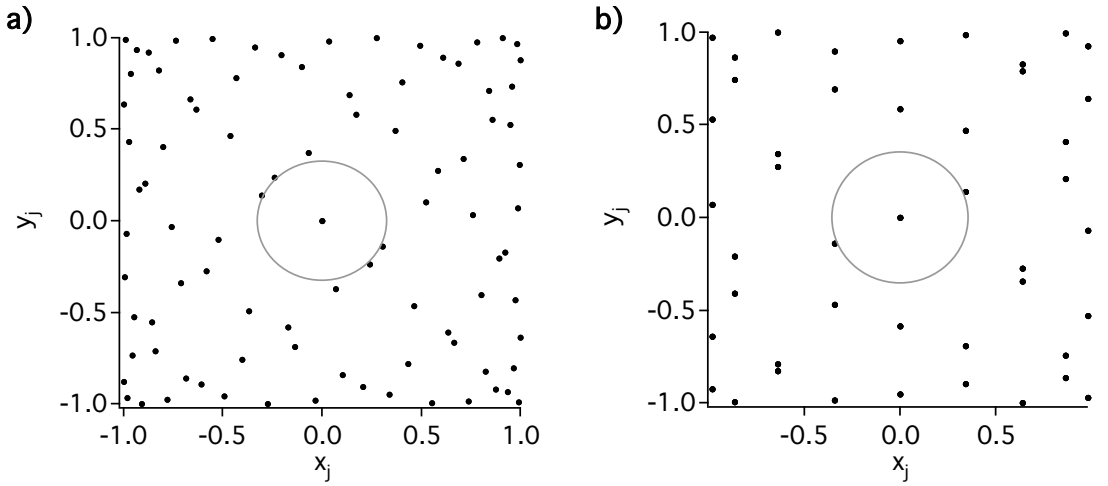

Figure 24: a) Pattern of the spots from both mirrors calculated with $X_0 = 1$, $Y_0 = 1$ and {N = 182, M_x = 80, M_y = 76}. The circle indicates the maximum size of the entrance/output hole. b) The spot pattern for {N = 90, M_x = 80, M_y = 76}

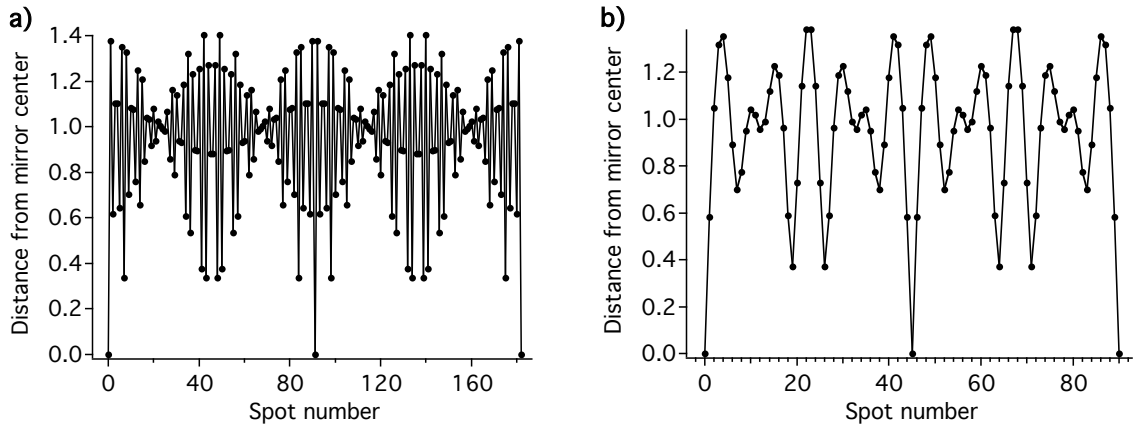

Figure 25: a) Distance $(x_j^2+y_j^2)^{1/2}$ of beam spots from mirror center on both mirrors with $X_0 = 1$ and $Y_0 = 1$ and {N = 182, M_x = 80, M_y = 76}. The beam hits the mirror in the center after 91 passes and 182 passes. The spot number 91 (odd number) is not on the entrance mirror therefore the beam is not coupled out, whereas spot number 182 (even number) is at the entrance/output hole. b) The distance of the beam spots to the mirror center for the pattern {N = 90, M_x = 80, M_y = 76}. Again spot number 45 is not on the entrance mirror (odd number) and therefore not coupled out, whereas spot number 90 (even number) is coupled out.

The multipass cell used in this work is a commercial one from Aerodyne Research (New Focus Model 5611) that has a standard alignment of $N = 182$, $M_x = 80$, $M_y = 76$ with a cell length of $L = 20$ cm. This is one of the best patterns regarding path length (36 meters) and spot separation and therefore was used for most of the measurements in this work. Another recommended pattern is $\{N = 90, M_x = 80, M_y = 76\}$ with a path length of 18 meters. But also other patterns are possible, e.g. $\{N = 50, M_x = 78, M_y = 79\}$ (see Figure 26 and Figure 27) and others with a path length of 10 meter, which was also used for some measurements in this work.

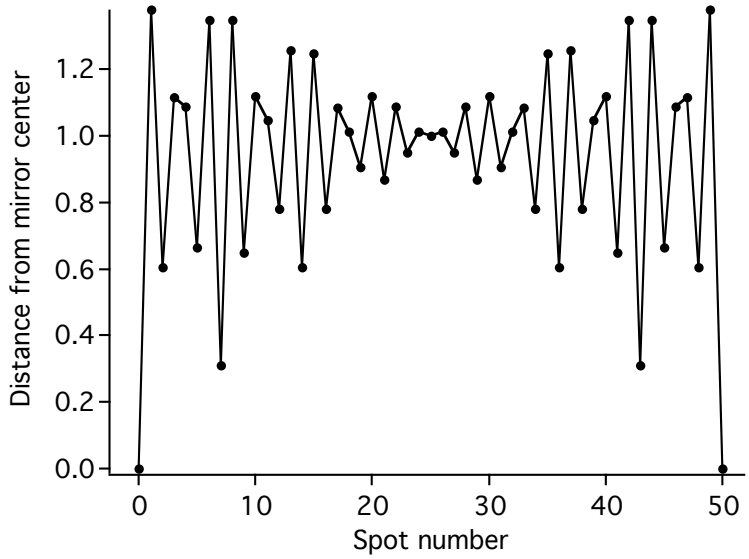

Figure 26: Distance of spots to mirror center for with $X_0 = 1$, $Y_0 = 1$ and {N = 50, $M_x = 78$, $M_y = 79$}.

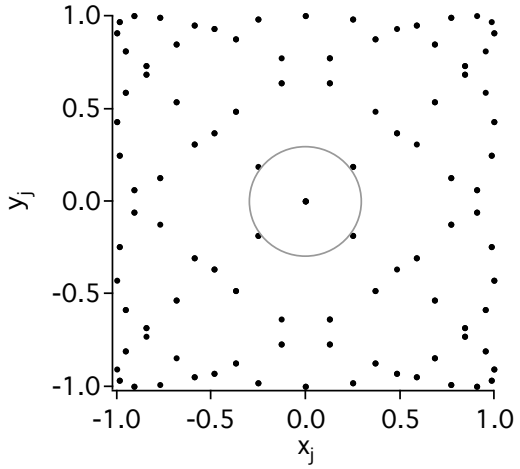

Figure 27: Spot pattern calculated with $X_0 = 1$, $Y_0 = 1$ and {N = 50, $M_x = 78$, $M_y = 79$}. The circle indicates the maximum size of the entrance hole. The spots from both mirrors are shown in one graph.

A path length of 36 m is long enough to measure CO in ambient air at a wavelength of 4.7 μm as shown in Figure 28. The measured concentration was 380 ppb, which is about the natural concentration in ambient air. The minimum change that can be measured with a signal-to-noise ratio of 3:1 is 0.48%, which correspond to a minimum detectable CO concentration of c_{min} = 38 ppb at a pressure of 50.0 mbar, or a minimum detectable absorption coefficient $\alpha_{min} = 1.3 \cdot 10^{-6}$ cm^{-1}. These measurements were made with a lock-in amplifier time constant of 300 ms, leading to a noise-limited sensitivity of this system of $7.1 \cdot 10^{-7}$ cm^{-1}Hz$^{-1/2}$.

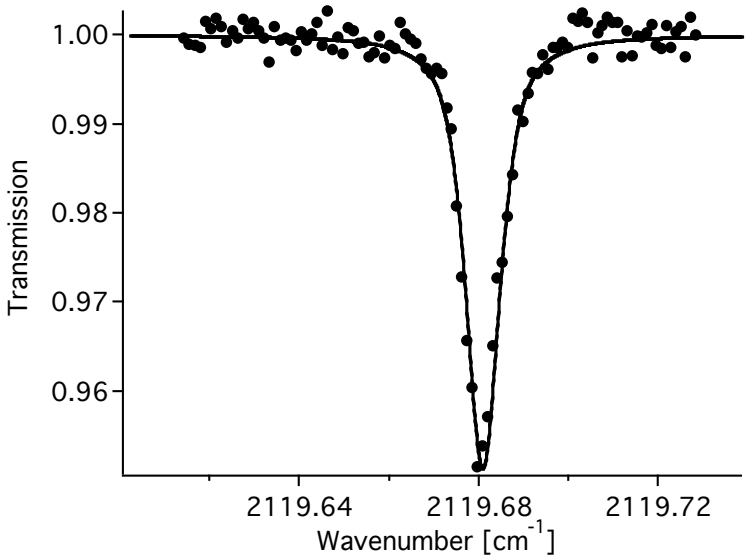

Figure 28: Measurements of CO in ambient air at a pressure of 50.0 mbar. The black line is the calculated spectrum from the HITRAN database [Hitran00].

Because the entrance hole is in the center of the mirror it is possible to send a beam into the cell at a very small angle so that the beam leaves the cell again after one reflection. This is very useful for measurements of isotope ratios, as the concentration of the main isotope is often much larger than the one of the less abundant isotopes. For measurements using very different line strengths for the main and the less abundant isotope (see chapter 4.6), we used exactly this option of balanced path lengths where the main and the rare isotopes are measured at two different path lengths. The incident beam either leaves the cell after only two passes or after the usual 182 or 50 passes, depending on the cell alignment. Thus path lengths of 36 m with 182 passes or 10 m with 50 passes for the long path and 40 cm with 2 passes for the short path are obtained. This path length ratio of 1:90 is very useful to balance the difference in abundance of the main and the rare isotopes, as it is e.g. $^{13}CO_2/^{12}CO_2$ = 1.1%. The mirrors have a protected silver surface (reflectivity: 0.99% from 3 to 10 μm, throughput: 0.99^{181} = 0.162), offering the possibility for measurements at wavelengths in the mid-IR. With a cell volume of 0.3 liter the astigmatic Herriott cell yields the best path length to volume ratio.

Such a dual path length detection scheme is not possible with a normal Herriott cell as the entrance hole is not in the center but at the edge of the mirror. With a White cell the path length is fixed as determined by the geometry of the cell. An option would be to place another mirror between the two mirrors A and A', so that the beam reflected on this mirror would leave the cell after two passes.

4.5 Infrared detectors

The detectors for infrared radiation should have a high responsivity at the desired wavelength, low noise to yield a good signal-to-noise ratio even at low powers, and a good linearity over a large power range. At wavelengths between 4 μm to 5 μm indium antimonide (InSb) detectors are a good choice as they offer a good responsivity at these wavelengths [Jud]. Another possible material is (Hg,Cd,Zn)Te semiconductor (MCT: mercury cadmium telluride), which can be used from 2 μm to 11 μm by varying the bandgap with the composition [Vig]. Detectors can be used in two different operation modes either photovoltaic or photoconductive. Photovoltaic detectors create a measurable voltage and current when illuminated with light, whereas photoconductive detectors change resistance and a low noise bias current is needed to measure this change. InSb detectors usually are used as photovoltaic devices at zero volt bias and the generated current is proportional to the intensity of the photons absorbed [Jud]. MCT detectors are available as photovoltaic and photoconductive device. The latter often have somewhat higher responsivity and sometimes slightly better signal-to noise performance but they exhibit excess noise at low frequencies (flicker noise), are often slower in frequency response, and need expensive low noise bias circuits. Therefore photovoltaic devices are preferred for most applications [Bos].

These detectors can be operated at room temperature, with thermoelectrical cooling or with liquid nitrogen cooling. For low laser power cooled detectors are needed as they exhibit a better signal-to-noise performance. A good figure of merit for comparing different detectors is the detectivity D^* [Jud, Vig]:

$$D^* = \frac{\sqrt{A \cdot \Delta f}}{NEP} \tag{56}$$

where A is the active area of the detector in cm^2, Δf is the signal bandwidth in Hz, and NEP = "Noise Equivalent Power" is the optical input power that produces a signal-to-noise ratio of 1:1. This means that the noise equivalent power increases proportional to the square root of the active area and the bandwidth. The detectivity for different detectors with different cooling methods are listed in Table 9. It can be seen that the detectivity is larger for lower temperatures.

Table 9: Detectivity and responsivity of different detectors (without preamplifier).

Detector	**Material**	**Cooling method**	**Detectivity [cm·Hz$^{1/2}$/W]**	**Responsivity [A/W]**
PVI-5 [Vig]	MCT	Room temperature	$3 \cdot 10^9$	>1.3
PVI-2TE-5 [Vig]	MCT	Thermoelectric	$3 \cdot 10^{10}$	>1.3
J10D-M204-R04M-60 [Jud]	InSb	Liquid N_2	$1 \cdot 10^{11}$	>3

Another important issue concerns the linearity of the detector response, i.e. if the light power is doubled the detector signal also should double. Deviation from this linearity leads to errors when measuring an absorption spectrum. The linearity of the two InSb detectors used in the experiment was measured by inserting thin Teflon sheets into the beam while a part of the beam before the sheets was directed to the other detector to normalize for power fluctuations. This way the linearity over a large power range was tested. The measured signal decreased exponentially with increasing number of Teflon sheets following the Beer-Lambert-law (see Figure 29). A line fitted to the logarithm of the signals manifests the good linearity of the response. Additionally not only a good linearity is important but also that the slope of the linearity should be similar in order to obtain the same voltage change for the same light power change, which is the case for the two detectors used in this experiment.

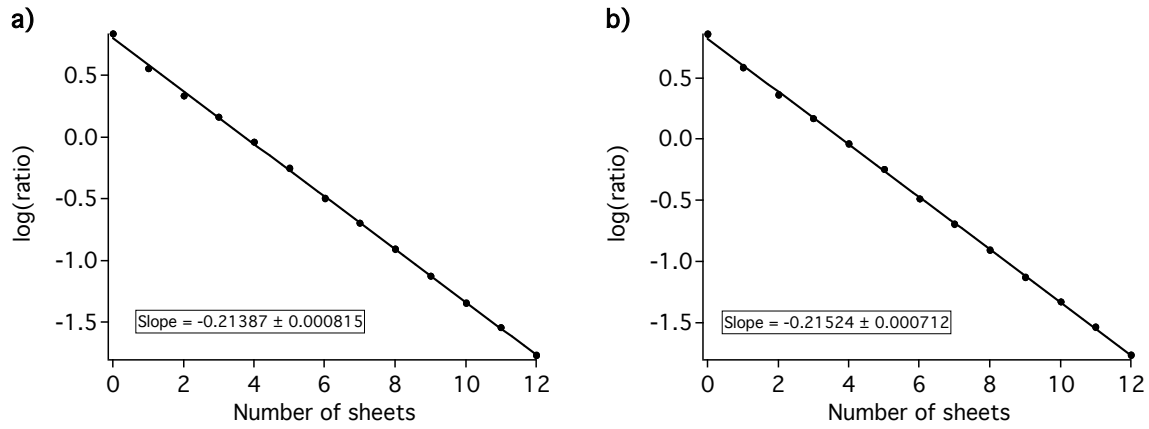

Figure 29: Linearity measurements of the two detectors used in the experiment. The power of the DFG signal is decreased by inserting thin Teflon sheets into the beam. To normalize the power regarding power fluctuations a beam splitter directs a part of the light to a reference detector. The power on the tested detector decreases exponentially with the number of Teflon sheets as expected by the Beer-Lambert-law. For both detectors a) and b) a line is fitted to the logarithm of the measured signal, both showing a good linearity of the detector response. In addition the slopes are about the same for the two detectors, which implies a similar signal change for the same change of light power.

A more precise way to measure the linearity of a detector would be to send two beams onto the detector, measure the signal generated by each beam separately, then measure the signal of both beams together. In case of good linearity, the sum of the separately measured beams should equal the signal of both beams together. In order to know the linearity over a large power range, this measurement should be repeated at different powers of one beam. The InSb are usually considered to have a very good linearity whereas the MCT detectors often show deviations from linear responses.

4.6 Absorption line selection

4.6.1 Selection criteria

For the selection of the most appropriate molecular absorption lines several important points must be considered. First of all the lines should be free of interference with other isotopes or other molecules. Another important aspect concerns the line strength. For measurements of rare isotopes at low concentrations (ppm-range or below) the absorption lines should be as strong as possible to obtain a good signal. Furthermore, the absorption should preferably be similar by using either a weak absorption line or a shorter path length for the main isotope to balance the differences in the abundance of the isotopes. Thus, the choice of absorption lines is rather limited when measuring simultaneously three isotopes (see Figure 30, Figure 31 and Figure 32 for CO, CO_2 and N_2O, respectively), as all the corresponding absorption lines should lie within the computer-controlled tuning range of the laser.

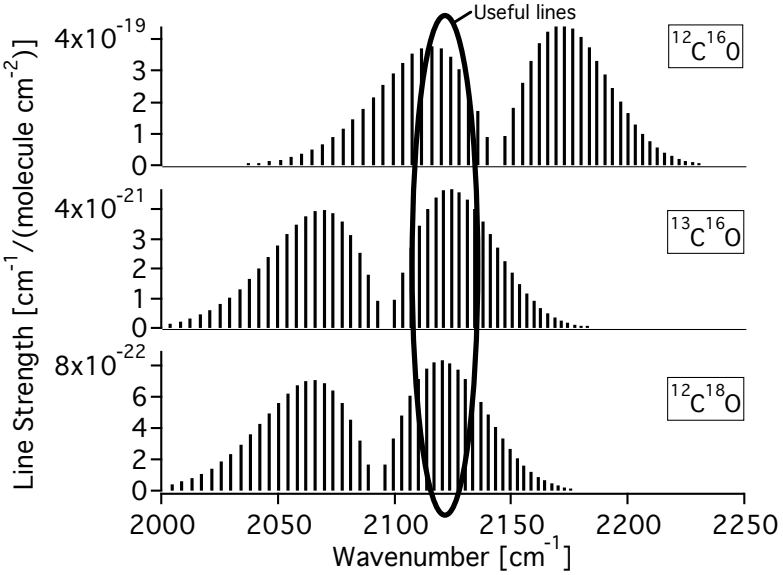

Figure 30: Absorption lines of CO for different isotopes: $^{12}C^{16}O$, $^{13}C^{16}O$ and $^{12}C^{18}O$ [Hitran05]. Only the absorption lines within the marked part yield sufficient line strength to be used.

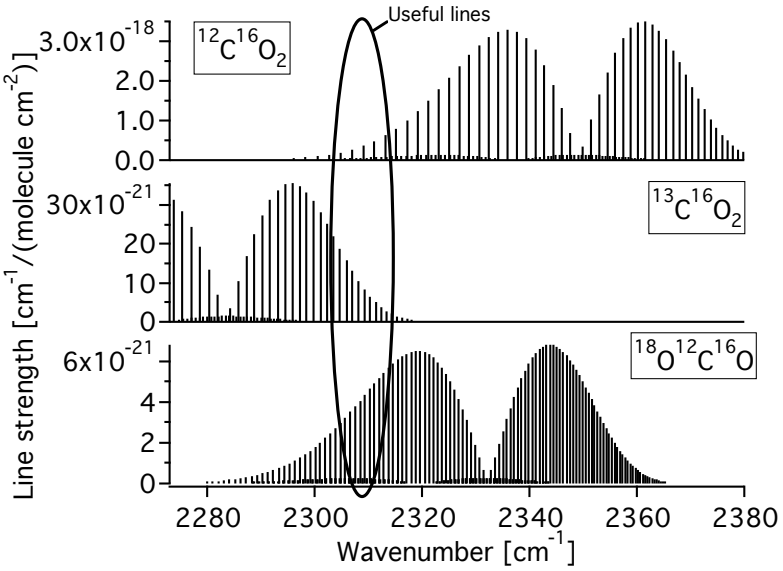

Figure 31: Absorption lines of CO_2 for different isotopes: $^{12}C^{16}O_2$, $^{13}C^{16}O_2$ and $^{18}O^{12}C^{16}O$ [Hitran05]. The marked part yields absorption lines that fulfill the requirements the best.

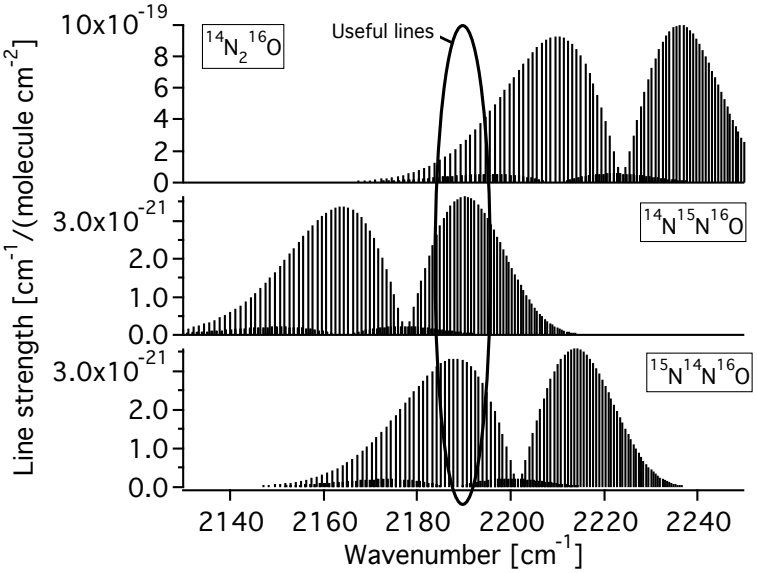

Figure 32: N_2O absorption lines for different isotopes. There is only a small wavelength range where the strong absorption lines from $^{14}N^{15}N^{16}O$ and $^{15}N^{14}N^{16}O$ overlap [Hitran05].

4.6.2 Temperature sensitivity

The problem that the concentration of the main isotope is often considerably higher than that of the less abundant isotope (e.g. $^{13}CO_2/^{12}CO_2$ = 1.1%) can be solved in two ways, either by measuring two lines of similar strength or by choosing two lines with about the same lower energy level but with very different line strength. The first option has the disadvantage that

the measurements usually will be very temperature sensitive because the temperature sensitivity of the isotopic ratio Δδ/ΔT is proportional to the difference of the ground-state energies ΔE of the corresponding transitions [Ber94]:

$$\frac{\Delta\delta}{\Delta T} \approx \frac{\Delta E}{kT^2} \tag{57}$$

where k is the Boltzmann constant, T is the absolute temperature and δ has been defined in Eq. (2) in chapter 1. As an example the temperature sensitivity $\Delta\delta^{13}C/\Delta T$ of CO_2 can be calculated taking the $^{13}CO_2$-line at 2310.347 cm^{-1} (line strength: $6.447 \cdot 10^{-21}$ $cm^{-1}/(molecule \cdot cm^{-2})$, corrected with the natural abundance) paired with the $^{12}CO_2$-line at 2310.002 cm^{-1} (line strength: $4.664 \cdot 10^{-21}$ $cm^{-1}/(molecule \cdot cm^{-2})$, weak line) or, alternatively, paired with the $^{12}CO_2$-line at 2311.106 cm^{-1} (line strength: $4.731 \cdot 10^{-19}$ $cm^{-1}/(molecule \cdot cm^{-2})$, strong line) [Hitran05]. The lower energy level of the $^{13}CO_2$-line is $E_{13} = 639.6309$ cm^{-1} and the one of the weak $^{12}CO_2$-line is $E_{12} = 1454.9687$ cm^{-1}. This line pair has similar line strength but the temperature sensitivity $\Delta\delta^{13}C/\Delta T = 13.5‰$ K^{-1} is very large. When using a balanced path length setup the strong $^{12}CO_2$-line can be used instead with a lower energy level $E_{12} = 704.3005$ cm^{-1}, resulting in a temperature sensitivity of only $\Delta\delta^{13}C / \Delta T = 1.1‰$ K^{-1}. For most applications the required precision is $\Delta\delta = 1‰$ or less, so either the gas cell needs to be very well temperature stabilized, as this is done e.g. by Castrillo et al. [Cas04], Tuzson et al. [Tuz07] and Erdélyi et al. [Erd02], or a balanced path length setup should be used, as e.g. implemented by McManus et al. [Man05] and Saleska et al. [Sal06]. In Table 12 the different absorption lines are listed and in Table 13 the temperature sensitivity for all combinations are shown.

For N_2O the chosen absorption lines are at 2188.6876 cm^{-1} ($^{14}N^{15}N^{16}O$), 2188.7560 cm^{-1} ($^{15}N^{14}N^{16}O$), 2188.9384 cm^{-1} ($^{14}N_2{}^{16}O$, weak line) and 2188.1894 cm^{-1} ($^{14}N_2{}^{16}O$, strong line), as listed in Table 11 [Hitran05]. These lines fulfill above requirements, with the only exception of the lower energy level E_{low} of the strong line ($E_{low} = 588.8$ cm^{-1}) of the main isotope, which is not as close to the lower energy levels of the other isotopes ($^{14}N^{15}N^{16}O$: $E_{low} = 76.2$ cm^{-1} and $^{15}N^{14}N^{16}O$: $E_{low} = 97.2$ cm^{-1}) as it could be, but it is still better than the weak line of the main isotope $^{14}N_2{}^{16}O$ ($E_{low} = 1198.4$ cm^{-1}). The absorption line of $^{14}N_2{}^{16}O$ at 2211.3982 cm^{-1} would fit better (lower energy level at $E_{low} = 87.98$ cm^{-1}) but it was outside the piezo scan range of the ECDL and therefore could not be reached computer controlled. In Figure 33 it can be seen that it is not possible to choose a strong line (corrected with the natural abundance) from the less abundant isotope and a comparable weak line from the main isotope with similar lower energy level.

For CO the absorption lines listed in Table 10 were chosen. These combinations of absorption lines fulfill the requirements and have a temperature sensitivity lower than 0.06‰/K for $\delta(^{13}C^{16}O)$ and lower than 0.4‰/K for $\delta(^{12}C^{18}O)$. CO is a diatomic molecule end has therefore a simpler spectrum than N_2O and CO_2. But this also means that there are no weak absorption lines with line strength comparable to the strong one of the less abundant

isotopes within the piezo scan range of the laser. Therefore it is not possible to measure all isotopes with the same path length and a balanced path length setup is required.

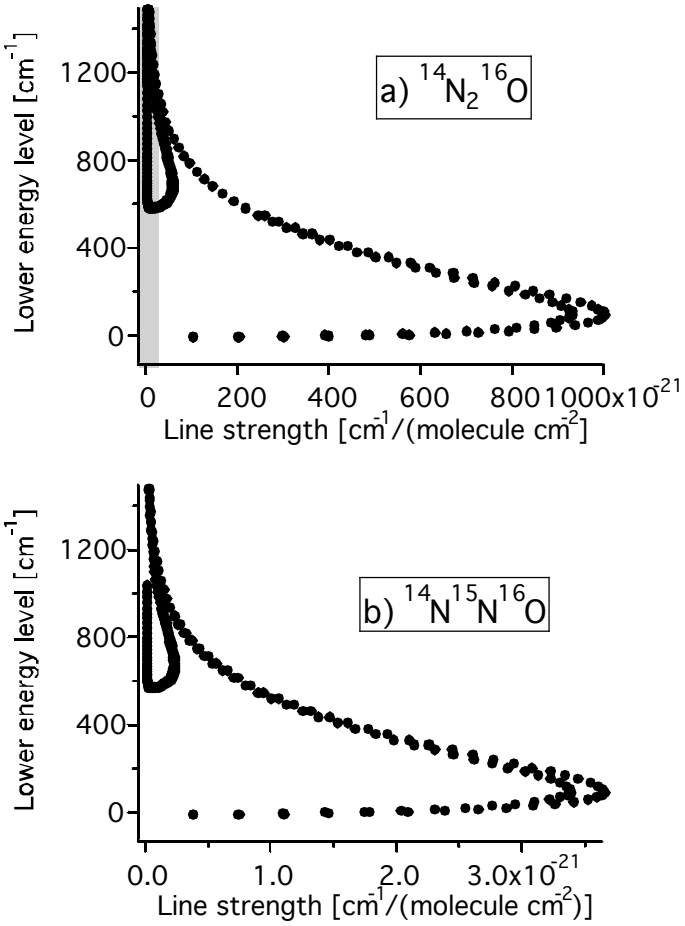

Figure 33: Relation between line strength (corrected with the natural abundance) and lower energy level for the main and a less abundant isotope of N_2O [Hitran05] (compare also Figure 32). The grey part indicates the region where the line strength of the main isotope is not more than ten times higher than the one from the less abundant. It can be seen that it is not possible to choose a strong line from the rare isotope and a comparable weak line from the main isotope with similar lower energy level.

Table 10: Absorption lines of different CO isotopes used in these measurements and the corresponding temperature sensitivity of the δ-value [Hitran05].

Isotope	**Wavenumber [cm^{-1}]**	**Line strength [cm^{-1}/(molecule·cm^{-2})]**	**Lower energy-level [cm^{-1}]**	**Temperature sensitivity of d-value [‰/K]**
$^{12}C^{16}O$	2119.6810	$3.694 \cdot 10^{-19}$	80.7354	–
$^{13}C^{16}O$	2120.8747	$4.618 \cdot 10^{-21}$	77.1850	0.058
$^{12}C^{18}O$	2120.2349	$8.289 \cdot 10^{-22}$	102.5175	0.36

Table 11: Absorption lines of different N_2O isotopes used in these measurements and the corresponding temperature sensitivity of the δ-value [Hitran05].

Isotope	**Wavenumber [cm^{-1}]**	**Line strength [cm^{-1}/ (molecule·cm^{-2})]**	**Lower energy-level [cm^{-1}]**	**Temperature sensitivity of δ-value compared to (1) [‰/K]**	**Temperature sensitivity of δ-value compared to (2) [‰/K]**	**Temperature sensitivity of δ-value compared to (3) [‰/K]**
$^{14}N_2{}^{16}O$ (1)	2188.9384	$2.473 \cdot 10^{-21}$	1198.4	–	–	–
$^{14}N_2{}^{16}O$ (2)	2188.1894	$2.143 \cdot 10^{-19}$	588.8	–	–	–
$^{14}N_2{}^{16}O$ (3)	2211.3982	$9.178 \cdot 10^{-19}$	88.0	–	–	–
$^{14}N^{15}N^{16}O$	2188.6876	$3.581 \cdot 10^{-21}$	76.2	18	8.5	0.20
$^{15}N^{14}N^{16}O$	2188.7560	$3.315 \cdot 10^{-21}$	97.2	18	8.1	0.15

Table 12: Absorption lines of different CO_2 isotopes used in measurements [Hitran05].

Isotope	**Wavenumber [cm^{-1}]**	**Line strength [cm^{-1}/ (molecule·cm^{-2})]**	**Lower energy-level [cm^{-1}]**
$^{12}CO_2$ (w1)	2308.2247	$4.73 \cdot 10^{-21}$	1483.94
$^{12}CO_2$ (w2)	2309.1166	$4.80 \cdot 10^{-21}$	1469.06
$^{12}CO_2$ (w3)	2310.0024	$4.85 \cdot 10^{-21}$	1454.97
$^{12}CO_2$ (w4)	2310.6860	$6.07 \cdot 10^{-21}$	1449.38
$^{12}CO_2$ (s1)	2306.9257	$2.69 \cdot 10^{-19}$	843.03
$^{12}CO_2$ (s2)	2308.5703	$5.91 \cdot 10^{-20}$	1080.39
$^{12}CO_2$ (s3)	2309.0276	$3.62 \cdot 10–^{19}$	772.11
$^{12}CO_2$ (s4)	2309.5960	$6.48 \cdot 10^{-20}$	1054.76
$^{12}CO_2$ (s5)	2310.5059	$7.03 \cdot 10^{-20}$	1031.13
$^{12}CO_2$ (s6)	2311.1056	$4.80 \cdot 10^{-19}$	704.30
$^{13}CO_2$ (1)	2308.1711	$1.05 \cdot 10^{-20}$	519.56
$^{13}CO_2$ (2)	2309.2712	$8.36 \cdot 10^{-21}$	578.04
$^{13}CO_2$ (3)	2310.3470	$6.53 \cdot 10^{-21}$	639.63
$^{18}O^{12}C^{16}O$ (1)	2308.4164	$4.07 \cdot 10^{-21}$	320.23
$^{18}O^{12}C^{16}O$ (2)	2309.3139	$4.36 \cdot 10^{-21}$	298.89
$^{18}O^{12}C^{16}O$ (3)	2310.2056	$4.64 \cdot 10^{-21}$	278.28

Table 13: Temperature sensitivity of δ-value for different absorption lines. The values marked in bold are the lowest temperature sensitivity for the corresponding isotopes indicating the best combination.

Temperature sensitivity [‰/K]	**$^{12}CO_2$ (w1)**	**$^{12}CO_2$ (w2)**	**$^{12}CO_2$ (w3)**	**$^{12}CO_2$ (w4)**	**$^{12}CO_2$ (s1)**	**$^{12}CO_2$ (s2)**	**$^{12}CO_2$ (s3)**	**$^{12}CO_2$ (s4)**	**$^{12}CO_2$ (s5)**	**$^{12}CO_2$ (s6)**
$^{13}CO_2$ (1)	16.1	15.8	15.6	15.5	5.38	9.34	4.20	8.91	8.52	3.08
$^{13}CO_2$ (2)	15.1	14.8	14.6	14.5	4.41	8.36	3.23	7.94	7.54	2.10
$^{13}CO_2$ (3)	14.1	13.8	13.6	13.5	3.39	7.34	2.21	6.91	6.52	**1.08**
$^{18}O^{12}C^{16}O$ (1)	19.4	19.1	18.9	18.8	8.70	12.7	7.52	12.2	11.8	**6.39**
$^{18}O^{12}C^{16}O$ (2)	19.7	19.5	19.2	19.1	9.06	13.0	7.88	12.6	12.2	6.75
$^{18}O^{12}C^{16}O$ (3)	20.1	19.8	19.6	19.5	9.40	13.4	8.22	12.9	12.5	7.09

4.7 Experimental arrangements

4.7.1 Single-cell setup and balanced path length detection

As discussed in the previous section 4.6.2, we chose the optimum of minimum temperature sensitivity $\Delta\delta / \Delta T$ and hence the balanced path length configuration. The astigmatic multipass Herriott cell (New Focus 5611) offers the possibility to enter the cell at another angle than usual, so that the beam leaves the cell after only two passes (Figure 34). This enables measurements at two lines of very different line strength by using two different path lengths (balanced path length detection scheme) [Man05]. In this setup the 50-pass configuration was used (see chapter 4.4.2), resulting in path lengths of 10 m and 40 cm.

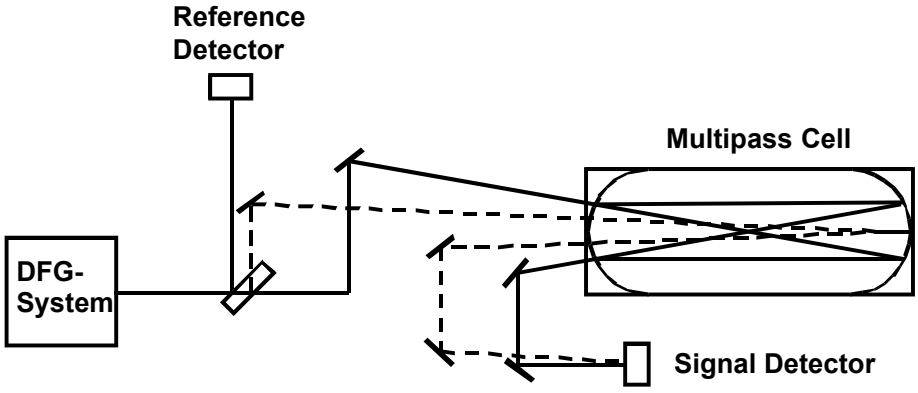

Figure 34: Setup for transmission spectroscopy. In the astigmatic Herriott cell there are two paths, one of 10 m (solid line) and one of 40 cm (dashed line).

As laser source the DFG-system described in chapter 3.3.1.2 is used. Before the cell a beam splitter directs part of the light to a reference detector to record the DFG power. After the multipass cell there is another detector to record the transmitted light. We use InSb detectors with liquid nitrogen cooling (Judson Technologies J10D-M204-R04M-60) with an active area of 4x4 mm^2. The light is modulated with a chopper at a frequency of 2 kHz. The detector signals are measured with lock-in amplifiers with a time constant of 100 ms. The measurements were made at a pressure of 50 mbar to avoid overlapping of the absorption lines.

Figure 35 shows an example of isotope measurements with this setup. The isotope ratios $^{13}C/^{12}C$ and $^{18}O/^{16}O$ of 450 ppm CO_2 in ambient indoor air were measured with balanced path lengths (40 cm and 10 m) and only long path (10 m only). The measured absorption lines are depicted in Figure 35. The background noise is dominated by detector noise and is identical for both path lengths, but because the absorption of the $^{12}C^{16}O_2$ line is stronger, the signal-to-noise ratio is four times better for this line.

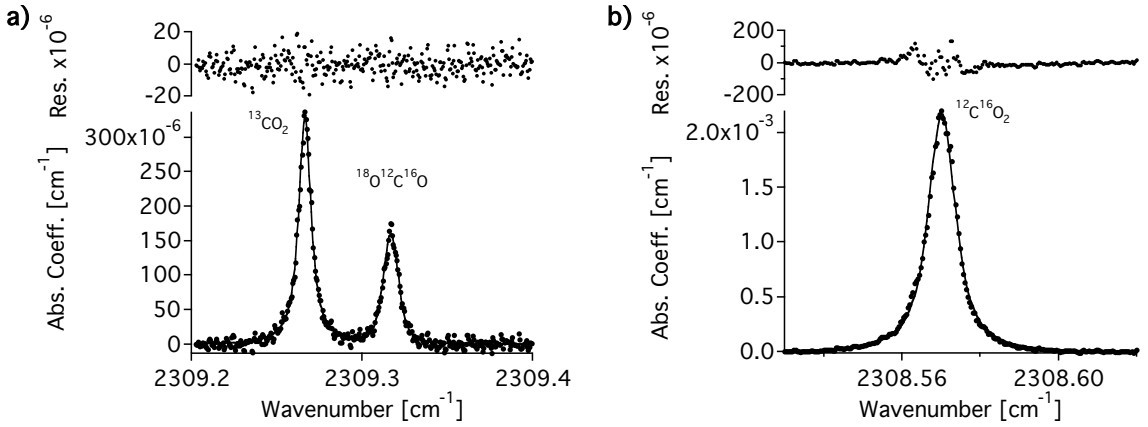

Figure 35: Absorption lines of different isotopes of 450 ppm CO_2 in ambient indoor air. Experimental data (dots) and Voigt fit (solid line) for 10 m path length, residuals on top.

For analyzing the measurements a Voigt function is fitted to the absorption lines. Then the concentration is determined by using the area under the Voigt line and the known line strength. By comparing the concentrations of the main and the less abundant isotope the isotopic ratio can be calculated. Our results for the various CO_2 isotopes are listed in Table 14. They are in good agreement with the natural abundance ($^{13}CO_2/^{12}CO_2$ = 1.1%, $^{16}O^{12}C^{18}O/^{12}C^{16}O_2$ = 0.39%) [Hitran05], but the precision still needs to be improved. The concentrations were in the ppm range which is sufficient for measurements of CO_2 in ambient air, yet not for N_2O and CO.

Table 14: Measurements of isotopic ratios and δ-values in different trace gases with our DFG system and multipass cell.

Gas	Concentration	Isotope ratio: single path length	Isotope ratio: balanced path length
CO_2	Laboratory air:	$^{13}C/^{12}C$: 1.3% ± 0.2%	$^{13}C/^{12}C$: 1.4% ± 0.3%
	450 ppm CO_2	$^{18}O/^{16}O$: 0.44% ± 0.06%	$^{18}O/^{16}O$: 0.47% ± 0.11%

Other laser spectroscopic instruments reported in literature often used high concentrations or alternatively low precisions were obtained and many groups only measured one isotope ratio, mainly $^{13}C/^{12}C$ and not two or more as presented here. However, the best results were obtained by McManus et al. [Man05] with ±0.18‰ for $^{13}C/^{12}C$ and by Tuzson et al. [Tuz07] with ±0.16‰ for $^{13}C/^{12}C$ and ±0.28‰ for $^{18}O/^{16}O$, both at ambient concentration of CO_2. They both used a single-cell with a astigmatic Herriott cell like for our measurements. McManus et al. implemented a balanced path length detection scheme, whereas Tuzson et al. employed an only long path configuration. Both used a pulsed quantum cascade laser as laser source and the data evaluation required deconvolution of the absorption line shape and the laser line shape. Their results are better than the ones reported here, but both systems are much more sophisticated. They are equipped with a high-precision temperature stabilization and a complicated data evaluation, which includes measured temperature and pressure changes. Their results demonstrate the large potential of laser spectroscopy for isotope measurements. By using a stronger light source, e.g. by implementing a waveguide PPLN, and implementing better pressure and temperature control, similar precisions are expected for the setup presented here.

4.7.2 Dual-cell setup: Sample cell and reference cell

The concentration of the measured gas is given by the area under the absorption line divided by the line intensity. To measure differences in concentrations of less than 1‰ a precise measurement of the wavelength is required and the line intensities should be known exactly. To avoid these problems a reference cell is used to measure a sample gas and the reference gas simultaneously. We designed and built a single pass cell that offers two different path lengths. It consists of a tube (stainless steel) and AR-coated CaF_2 windows. No Brewster windows were used to avoid path length changes if the beam position was shifted slightly. The long path of 50 cm is along the tube and the short path of 1 cm is perpendicular to the tube. This yields a path length ratio of 1:50 compared to 1:91 for the multipass cell. The long path of the reference cell could be doubled to 100 cm by having two passes yielding a path length ratio of 1:100. But the short path length of 1 cm demands a narrow tube (diameter 6 mm), so for a second pass along the long path the beam would need to be refocused by using a curved mirror making this setup rather complex.

As sample cell we used again the astigmatic multipass Herriott cell, this time in the configuration yielding path lengths of 36 m (182 passes) and 40 cm (2 passes), respectively. This balanced path length approach enables the measurement of two lines of very different line strength.

The experimental arrangement is presented in Figure 36. After the DFG-system (section 3.3.1.2) a beam splitter (CaF_2-plate) directs part of the light to the reference cell. The second reflection of the plate is used for the short path in the multipass cell. In front of the reference cell is a second beam splitter to direct a part along the short path through the reference cell. Again, the InSb detectors with liquid nitrogen cooling were used.

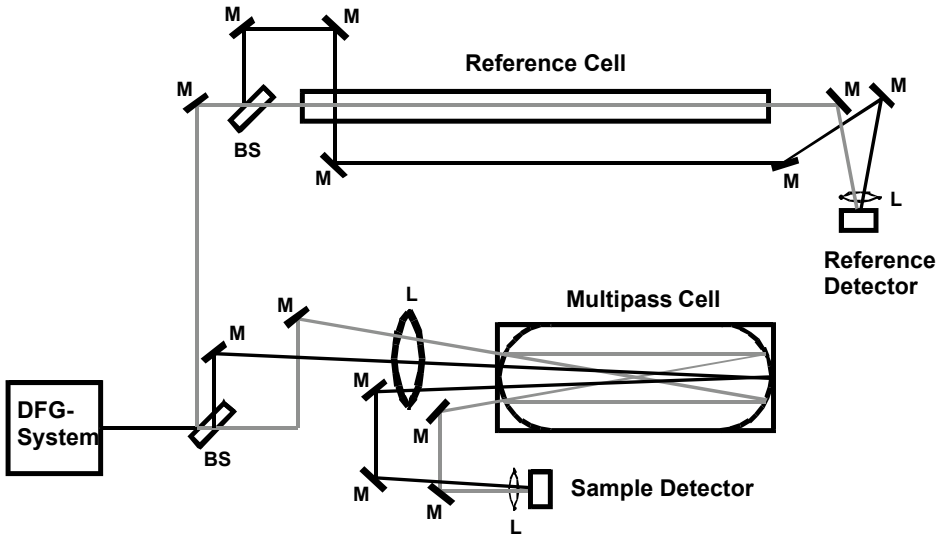

Figure 36: Setup for the balanced path length detection scheme consisting of an astigmatic Herriott cell and a single pass reference cell. If the beam enters the multipass cell at a small angle the beam leaves the cell after only two passes (40 cm) instead of 182 (36 m). Also the reference cell has two different path lengths, along the tube (50 cm) and perpendicular to the tube (1 cm). (BS: beam splitter (CaF_2-plate), M: mirror, L: lens)

When measuring simultaneously in two different cells and evaluating the measurements by comparing point by point instead of comparing the area under the lines, it is very important that the measured absorption lines have the same shape. This shape is influenced by pressure, temperature, line strength and concentration. As the same absorption line is measured in both cells, the line strength is the same. In order to have identical gas pressure, the same pressure meter with a precision of ±0.1 mbar is used for filling the cells. After the filling a waiting time of one hour before starting the measurements ensures that both cells are at room temperature. For equal absorption the concentration multiplied by the path length should be the same in the two cells. So if the path length in the multipass cell is 36 m and in the reference cell 50 cm then the concentration in the reference cell should be 72 times larger than in the sample gas cell, e.g. 0.72% and 100 ppm, respectively.

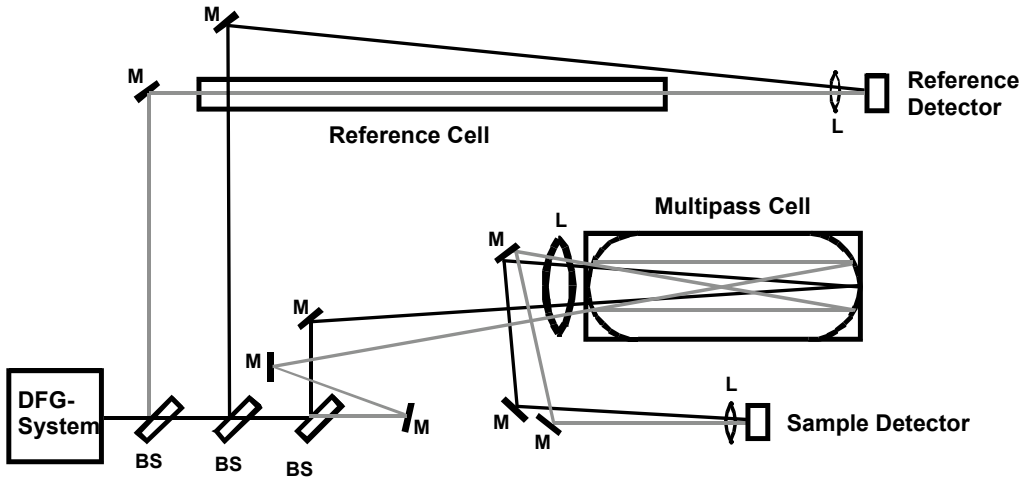

Figure 37: Setup for the balanced path length detection scheme used with the fiber-coupled DFG-system. (BS: beam splitter (CaF_2-plate), M: mirror, L: lens)

For the fiber coupled DFG-system (section 3.3.1.3) the setup of the balanced path length detection scheme was slightly changed (Figure 37). Three beam splitters in series are inserted into the beam to split it into four beams. In contrast to the first setup where the second reflection of the beam splitter was used for the short path in the multipass cell and where the beam to the reference cell was split up again for the two path lengths, more power is directed along the short paths in the reference and sample cells with this setup resulting in a better signal-to-noise ratio. The signals after the long and short path in the reference cell and after the long path in the sample cell have about the same amplitude, the signal after the short path in the multipass cell is about two times smaller. This configuration was found not to be a problem as the InSb-detectors usually have a linear response over a large range, as discussed in chapter 4.5.

5. Nitrous oxide (N_2O) isotope measurements

5.1 Single cell configuration: Setup, method and results

The first measurements of N_2O isotopes were made using only one cell and direct absorption spectroscopy with the setup described in chapter 4.7.1. The isotopic ratio $^{15}N/^{14}N$ of N_2O (2040 ppm in synthetic air) was determined by using the balanced path length method as well as using only long path detection. For analyzing the measurements a Voigt function is fitted to the absorption lines (see Figure 38). Then the concentration is determined by using the area under the Voigt line and the known line strength. By comparing the concentrations of the main and the less abundant isotope the isotopic ratio is calculated.

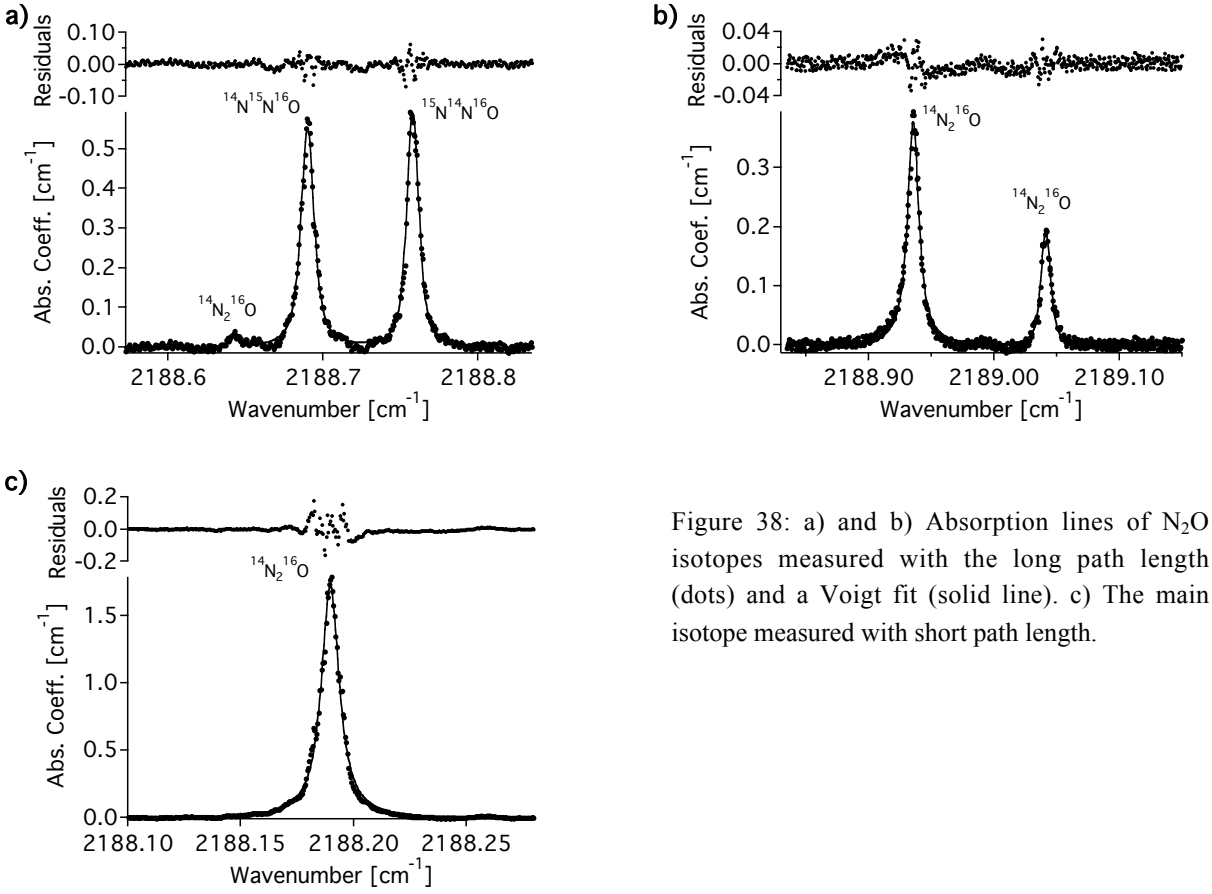

Figure 38: a) and b) Absorption lines of N_2O isotopes measured with the long path length (dots) and a Voigt fit (solid line). c) The main isotope measured with short path length.

The results for the isotope ratios are listed in Table 15. They are in good agreement with the natural abundance ($^{14}N^{15}N^{16}O/^{14}N_2{}^{16}O$ = $^{15}N^{14}N^{16}O/^{14}N_2{}^{16}O$ = 0.36%) [Hitran05], but the precision is not yet satisfactory. The concentrations of the gases were in the ppm range which is sufficient for measurements of CO_2 in ambient air, yet not for N_2O and CO. Nevertheless, the concentrations used in this study are lower than for all other previous N_2O studies [Ueh03a, Ueh03b, Gag05] where pure N_2O samples were used but higher precisions were achieved (0.3‰).

Table 15: Measurements of isotopic ratios in different trace gases with our DFG system and multipass cell. To calculate the δ-value, the measured isotope ratios were compared to the natural abundance.

	Only long path	**Balanced path length**
Isotope ratios	$^{14}N^{15}N^{16}O/^{14}N_2{}^{16}O$: 0.30% ± 0.01%	$^{14}N^{15}N^{16}O/^{14}N_2{}^{16}O$: 0.35% ± 0.08%
	$^{15}N^{14}N^{16}O/^{14}N_2{}^{16}O$: 0.34% ± 0.02%	$^{15}N^{14}N^{16}O/^{14}N_2{}^{16}O$: 0.39% ± 0.08%
δ-value	$\delta(^{14}N^{15}N^{16}O)$: –170‰ ± 30‰	$\delta(^{14}N^{15}N^{16}O)$: –28‰ ± 220‰
	$\delta(^{15}N^{14}N^{16}O)$: –56‰ ± 60‰	$\delta(^{14}N^{15}N^{16}O)$: 83‰ ± 220‰

5.2 Dual-cell configuration: Setup, methods and results

5.2.1 Experimental arrangement and gas samples

To improve the measurement precision, a setup with a sample and a reference cell was used as described in chapter 4.7.2. Experiments were done with wavelength modulation as well as with direct absorption spectroscopy in combination with balanced path length detection or only long path detection. All four versions were tested and the results are compared regarding both the precision of a single measurement and the long-term stability.

The measurements were performed at room temperature and at a total gas pressure of 50 mbar to avoid overlapping of the absorption lines. The N_2O concentration in the reference cell was 5% taken from a certified mixture. The concentration in the sample cell was either 825 ppm, obtained by diluting the gas from the 5% mixture with room air (8.0 mbar 5% N_2O mixed with room air to 900 mbar) or 100 ppm from another certified mixture. The concentration of the mixture with room air was about two times higher than expected because of adsorption and desorption effects of the N_2O molecules to the cell walls during the diluting process.

5.2.2 Methods

Two different measurement methods were tested, namely wavelength modulation (WM) with first harmonic detection (chapter 4.3) and direct absorption spectroscopy (chapter 4.2). For wavelength modulation the wavelength of the ECDL was modulated across the absorption line with a frequency of 1 kHz and a modulation index of M = 2 (see chapter 4.3). The detector signals were recorded with lock-in amplifiers (Stanford Research Systems, SR830 DSP) with a time constant of 100 ms for long path measurements and 300 ms for short path measurements. A measurement of all three N_2O isotopes ($^{14}N^{15}N^{16}O$, $^{15}N^{14}N^{16}O$, $^{14}N_2{}^{16}O$) takes about 20 minutes. The measured spectrum is similar to the derivative of the absorption line. The advantage of WM is its zero background, i.e. no signal is generated without absorption. But any wavelength-depending change of laser power produces a signal on the detector, e.g. interference fringes caused by optical elements result in a wavelength-dependent background.

For direct absorption spectroscopy the wavelength was scanned across the absorption lines of all three isotopes and the detector signal was recorded by a data acquisition card (CompuScope14100, 14 bit resolution, 100 MS/s). The scans were performed by applying a sinusoidal voltage at 500 Hz to the piezo of the ECDL. To improve the signal-to-noise ratio 1000 scans were averaged for long path measurements and 5000 scans for short path measurements. From these measurements a moving average over 21 points was taken. For only long path measurements it takes 15 seconds for three different isotopes and 1.4 minutes for balanced path length detection.

5.2.3 Data evaluation

At low concentrations the detector signal measured with wavelength modulation is proportional to the concentration of the gas (see chapter 4.3). Therefore the δ-value (Eq. 2) can be obtained by taking the ratio of the measured signals of the sample and the reference gas for both isotopes and by comparing these ratios for the absorption lines of the main and the less abundant isotope.

To evaluate the data from our measurements we did not take the ratios mentioned above directly but plotted the detector signal ${}^{I}S_{sample}(\tilde{\nu})$ at frequency $\tilde{\nu}$ recorded after the sample gas versus the detector signal ${}^{I}S_{ref}(\tilde{\nu})$ recorded after the reference cell, for the isotope I. The fitted curve is a linear relation between sample signal and reference signal. A second order baseline is added to take a background (fringes caused by windows etc.) into account:

$$ {}^{I}S_{sample}(\tilde{\nu}) = {}^{I}a \cdot {}^{I}S_{ref}(\tilde{\nu}) + b_0 + b_1\tilde{\nu} + b_2\tilde{\nu}^2 \qquad (58) $$

By repeating this procedure for each isotope *I* and comparing the slopes ${}^{I}a$ of these curves of the main and the less abundant isotope, the difference of the isotopic composition between the sample and the reference gas can be calculated [Gag03]:

$$\delta = \left(\frac{{}^{minor}C_{sample} / {}^{main}C_{sample}}{{}^{minor}C_{ref} / {}^{main}C_{ref}} - 1 \right) \cdot 1000‰ = \left(\frac{{}^{minor}C_{sample} / {}^{minor}C_{ref}}{{}^{main}C_{sample} / {}^{main}C_{ref}} - 1 \right) \cdot 1000‰ \qquad (59)$$

$$\delta = \left(\frac{{}^{minor}ratio}{{}^{main}ratio} - 1 \right) \cdot 1000‰ = \left(\frac{{}^{minor}a}{{}^{main}a} - 1 \right) \cdot 1000‰ .$$

Here ${}^{main}C_{ref,sample}$ and ${}^{minor}C_{ref,sample}$ are the concentrations of the main and the less abundant (minor) isotope of the reference and the sample gas, respectively, and the ratios are given by ${}^{main}ratio = {}^{main}C_{sample} / {}^{main}C_{ref}$ and ${}^{minor}ratio = {}^{minor}C_{sample} / {}^{minor}C_{ref}$. The advantage of this method is that there is no need for correcting constant backgrounds. Figure 39 shows the result for wavelength modulation with only long path detection.

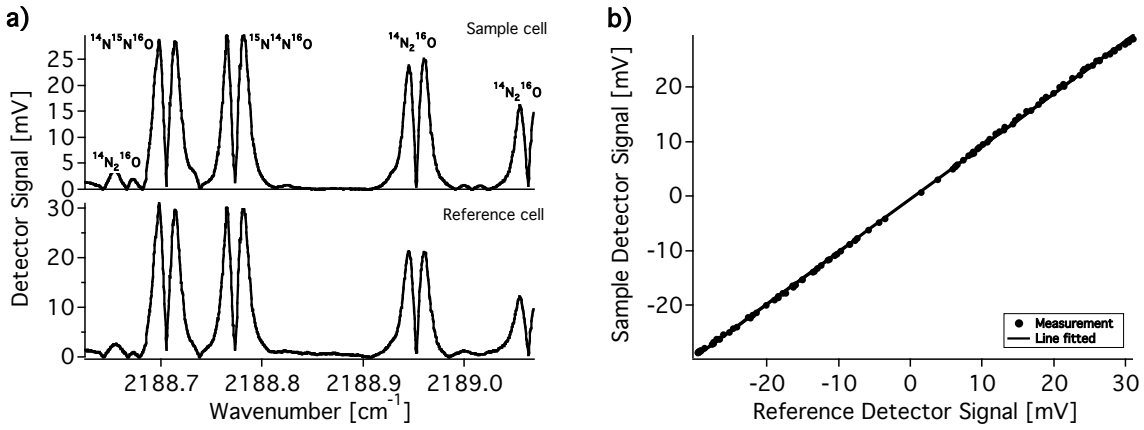

Figure 39: a) Absorption lines of N_2O isotopes measured with wavelength modulation (WM) and only long path detection. b) The WM measurements are evaluated by plotting the detector signal from the sample versus the detector signal from the reference gas, here shown for $^{14}N^{15}N^{16}O$. By comparing the slopes of these lines of each isotope, the δ-values can be calculated.

The measurements using direct absorption spectroscopy and recording the signals with the data acquisition card were evaluated similarly. A baseline was received by fitting the part between the absorption lines with a polynomial of tenth order. This baseline was subtracted and the detector signal of each absorption line was plotted versus the detector signal of the corresponding reference absorption line. Then the slope was determined as described in Eq. (58) for each isotope and the δ-value was calculated by comparing the slopes.

5.2.4 Results and discussion

Wavelength modulation in combination with only long path detection yields the best precision for a single measurement (3‰) and good reproducibility (6‰) as long as the temperature of the gas is stable. The influence of a temperature change can be seen in Figure 40 when the sample gas was cooled down when refilling the detector with liquid nitrogen standing next to the sample cell. If the measurements during the temperature change are included, the reproducibility increases to 18‰ for $\delta(^{14}N^{15}N^{16}O/^{15}N^{14}N^{16}O)$ and $\delta(^{15}N^{14}N^{16}O/^{14}N_2{}^{16}O)$. However, $\delta(^{14}N^{15}N^{16}O/^{15}N^{14}N^{16}O)$ is not influenced by the temperature change because the ratio of the absorption line strengths involved is nearly temperature independent in this case ($\Delta\delta / \Delta T$ = 8‰ compared to $\Delta\delta / \Delta T$ = 18‰, see Table 11). In addition to the temperature sensitivity, a further disadvantage of this method is that it takes about 20 minutes to record one spectrum leading to a low time resolution.

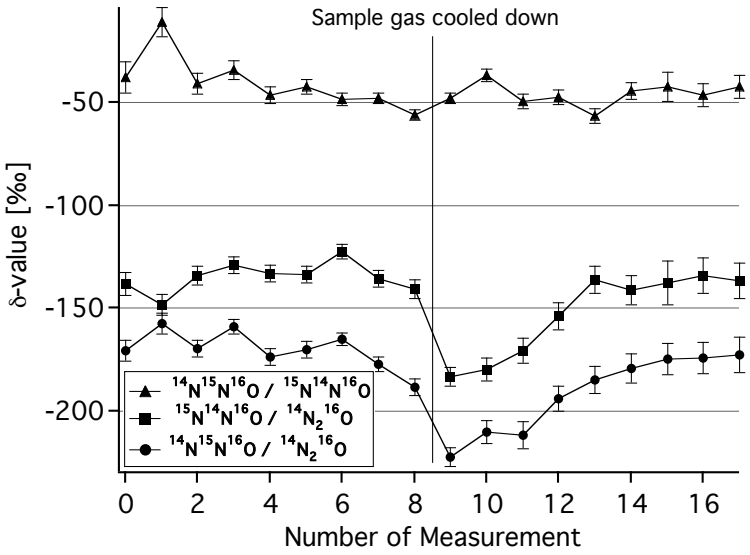

Figure 40: δ-value for different isotopes of N_2O measured with wavelength modulation combined with only long path detection. There is a strong change in $\delta(^{15}N^{14}N^{16}O/^{14}N_2{}^{16}O)$ and $\delta(^{14}N^{15}N^{16}O/^{14}N_2{}^{16}O)$ when the temperature of the sample gas changed because of refilling the detector with liquid nitrogen standing next to the cell. The $\delta(^{14}N^{15}N^{16}O/^{15}N^{14}N^{16}O)$ did not change because it is nearly temperature independent.

Wavelength modulation combined with balanced path length detection is less temperature dependent than only long path measurements. But it yields a worse precision of a single measurement (12‰) and accordingly a reproducibility of 14‰, which is still better than before with only long path detection. The precision, though, is worse than before because only a small part of the light is directed along the short path yielding a reduced signal-to-noise ratio on the detector. Again the recording of a spectrum takes 20 minutes.

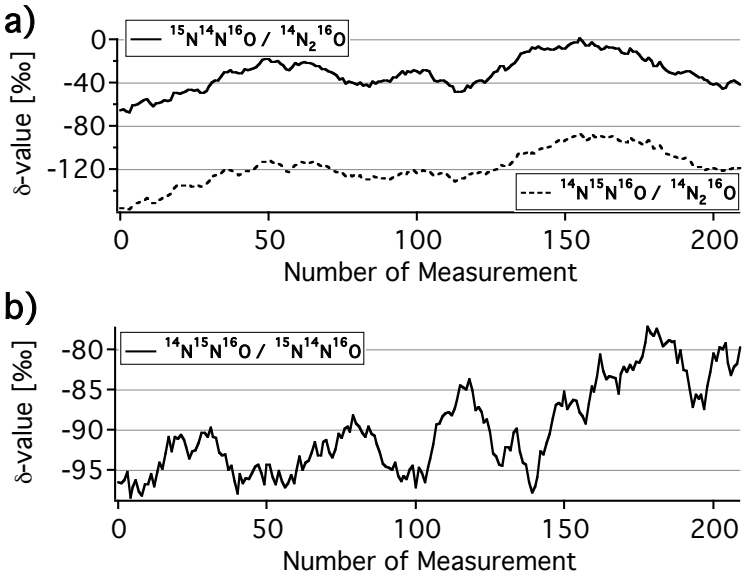

Figure 41: a) δ-value for different isotopes of N_2O measured with direct absorption spectroscopy and recording the data with a data acquisition card. Also here the temperature sensitivity of $\delta(^{14}N^{15}N^{16}O/^{14}N_2{}^{16}O)$ and $\delta(^{15}N^{14}N^{16}O/^{14}N_2{}^{16}O)$ can be observed. b) The stability of $\delta(^{14}N^{15}N^{16}O/^{15}N^{14}N^{16}O)$ is higher because this ratio is nearly temperature independent.

Direct absorption spectroscopy measured with the data acquisition card in combination with only long path detection scheme yields a good precision of a single measurement (5‰) but the reproducibility (15‰) is worse than the precision because of the temperature sensitivity of this method as seen in Figure 41 a). The reproducibility of the $^{14}N^{15}N^{16}O/^{15}N^{14}N^{16}O$ ratio is 6‰, because it is much less temperature sensitive (see Figure 41 b). The advantage of this method is its improved time resolution, it takes only 15 seconds for measuring three different isotopes.

When the spectrum is recorded with the data acquisition card in combination with the balanced path length detection scheme the reproducibility is improved (10‰). The precision (6‰) is better than the reproducibility but it is worse than with only long path detection because of the reduced signal-to-noise ratio for the short path. The low laser power along the short path also requires more averaging of scans, resulting in a lower time resolution. It takes 1.4 minutes for three different isotopes, which is still much better than when using wavelength modulation (20 minutes). All the results are listed in Table 16.

Table 16: Results of isotope ratio measurements for N_2O isotopes obtained with different measurement techniques combined with balanced path length or only long path detection schemes for different concentrations. (WM: wavelength modulation; DAQ: data acquisition card, definition of δ see Eq. (2))

Method	Concentration	Isotope ratios	δ-value average	Precision of a single measurement	Reproducibility	Number of measurements
WM only long path	825 ppm sample 5% reference	$\frac{^{14}N^{15}N^{16}O}{^{14}N_2{}^{16}O}$	–184‰	3.3‰	8.6‰ with temperature change: 18‰	19
		$\frac{^{15}N^{14}N^{16}O}{^{14}N_2{}^{16}O}$	–145‰	3.5‰	5.9‰ with temperature change: 18‰	
		$\frac{^{14}N^{15}N^{16}O}{^{15}N^{14}N^{16}O}$	–45.9‰	2.3‰	6.0‰	
WM only long path old reference cell (10 cm long)	100 ppm sample 5% reference	$\frac{^{14}N^{15}N^{16}O}{^{14}N_2{}^{16}O}$	49.4‰	4.8‰	6.4‰	10
		$\frac{^{15}N^{14}N^{16}O}{^{14}N_2{}^{16}O}$	80.5‰	5.3‰	6.9‰	
		$\frac{^{14}N^{15}N^{16}O}{^{15}N^{14}N^{16}O}$	–28.8‰	4.1‰	6.6‰	
WM balanced path length	825 ppm sample 5% reference	$\frac{^{14}N^{15}N^{16}O}{^{14}N_2{}^{16}O}$	230‰	11‰	17‰	10
		$\frac{^{15}N^{14}N^{16}O}{^{14}N_2{}^{16}O}$	274‰	12‰	14‰	
		$\frac{^{14}N^{15}N^{16}O}{^{15}N^{14}N^{16}O}$	–35.2‰	10‰	10‰	
DAQ only long path	825 ppm sample 5% reference	$\frac{^{14}N^{15}N^{16}O}{^{14}N_2{}^{16}O}$	–119‰	4.5‰	16‰	210
		$\frac{^{15}N^{14}N^{16}O}{^{14}N_2{}^{16}O}$	–31.5‰	5.0‰	15‰	
		$\frac{^{14}N^{15}N^{16}O}{^{15}N^{14}N^{16}O}$	–89.9‰	3.8‰	5.6‰	
DAQ balanced path length	825 ppm sample 5% reference	$\frac{^{14}N^{15}N^{16}O}{^{14}N_2{}^{16}O}$	145‰	6.4‰	11‰	203
		$\frac{^{15}N^{14}N^{16}O}{^{14}N_2{}^{16}O}$	172‰	6.3‰	9.5‰	
		$\frac{^{14}N^{15}N^{16}O}{^{15}N^{14}N^{16}O}$	–22.7‰	5.6‰	12‰	

When the same gas, though at different concentrations, is present in the reference cell and the multipass cell the δ-value is expected to be zero. But our measurements yield an offset depending on the measurement method and path length ratios (Table 16). Such an offset has also been observed by other authors [Gag03, Erd02, Ker99]. It may be explained by path length ratios not known precisely enough, by pressure or temperature differences between

sample and reference gas, or by nonlinearities in the detector response. When the day-to-day reproducibility is good enough this offset can be measured once and then subtracted for subsequent measurements. For measurements with wavelength modulation it also needs to be considered that Eq. (59) is only valid for small absorptions, for higher absorption this equation must be corrected otherwise the evaluation produces an offset [Cas05].

When comparing the different methods it can be concluded that recording the spectrum with the data acquisition card in combination with balanced path length detection is the most promising method because of its good time resolution and low temperature sensitivity (Table 17). But the best results are obtained with wavelength modulation in combination with only long path detection because of the best signal-to-noise ratio (Table 16). The main advantages and drawbacks of the four schemes employed are summarized in Table 17.

Table 17: Advantages and disadvantages of different measurement methods in combination with different detection schemes. (WM: wavelength modulation; DAQ: data acquisition card)

Method	**Advantage**	**Disadvantage**
WM and only long path	+ Signal-to-noise ratio	– Temperature sensitivity – Time resolution
WM and balanced path lengths	+ Temperature sensitivity	– Time resolution – Signal-to-noise ratio
DAQ and only long path	+ Time resolution + Signal-to-noise ratio	– Temperature sensitivity
DAQ and balanced path lengths	+ Time resolution + Temperature sensitivity	– Signal-to-noise ratio

A reason for the bad reproducibility might be the degradation of the ECDL, whose side-mode suppression was not sufficient anymore, yielding additional noise to the measurement. An indication for this is that previous measurements taken at lower concentrations (100 ppm) have about the same precision and the same reproducibility than the more recent measurements with 8 times higher concentrations (Table 16). Those measurements were repeated later and gave worse results than originally. Another problem might be the detectors because, depending on the quality of the vacuum, an ice layer is built on the surface of the nitrogen cooled detectors and their windows. This layer changes the transmission of the light to the detector because ice absorbs in the mid-IR and the layer acts as a dielectric coating changing the reflectivity of the window and the detector. Variation of the thickness of this ice layer may cause variations in the measurements and this way reducing the reproducibility. To reduce this problem the detectors should be evacuated regularly [The05, The06].

5.3 Fiber-coupled system

5.3.1 Results and discussion

The fiber-coupled DFG-system combined with the modified balanced path length detection scheme (Chapter 4.7.2) was evaluated with respect to long-term reproducibility and day-to-day reproducibility. At the same time different experimental parameters were tested and first harmonic detection is compared to second harmonic detection (Table 18). For all measurements a calibrated gas mixture of 100 ppm N_2O in synthetic air was used as sample gas and 1% of N_2O in air as reference gas. The measurements were made with wavelength modulation with a modulation frequency of 1 kHz and a modulation index of about two (see chapter 4.3). The measured data (see Figure 42) were evaluated as it was done in the free-space system in section 5.2.3.

Table 18: Experimental parameters of the different measurements

	Time constant [ms]	**Step size [mV]**	**Averaged over x δ-values**	**n^{th} harmonic detection**
Measurement A	1000	6	1	1
Measurement B	300	6	3	1
Measurement C	1000	3	1	1
Measurement D	1000	6	1	2

In measurement A a long time constant and a large step size were used, in measurement B a shorter measurement time was used but then averaged over three δ-values. In measurement C a smaller step size was tested and in measurement D second-harmonic detection was used instead of first harmonic (Table 18). One measurement of the δ-value of three different isotope took about 12 minutes. The results are listed in Table 19.

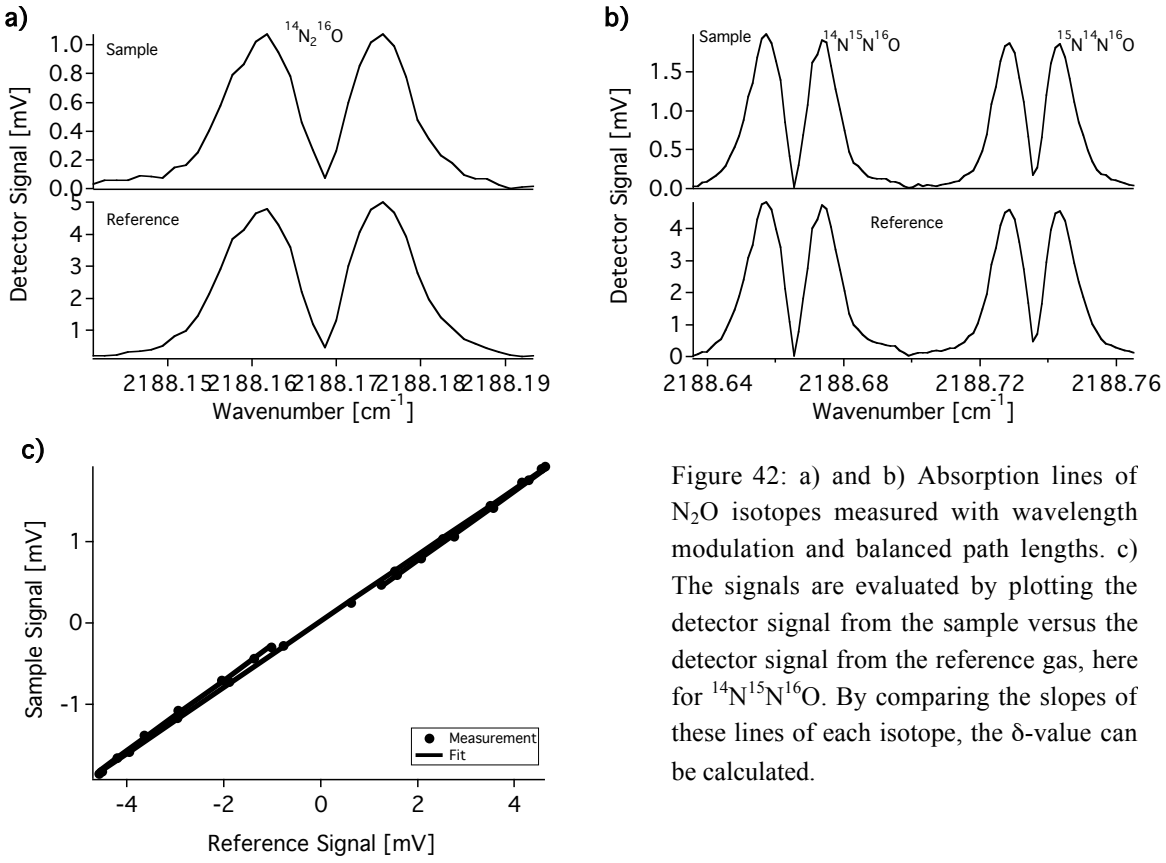

Figure 42: a) and b) Absorption lines of N_2O isotopes measured with wavelength modulation and balanced path lengths. c) The signals are evaluated by plotting the detector signal from the sample versus the detector signal from the reference gas, here for $^{14}N^{15}N^{16}O$. By comparing the slopes of these lines of each isotope, the δ-value can be calculated.

Table 19: Averages of d-values of measurements on different days within one week, with different experimental parameters as listed in Table 18.

	δ_1 [‰]	δ_2 [‰]	δ_3 [‰]
Measurement A	171.3 ± 9.1	171.0 ± 10.6	0.1 ± 6.0
Measurement B	172.0 ± 11.8	171.4 ± 8.5	2.0 ± 4.6
Measurement C	182.3 ± 21	176 ± 16.5	4.7 ± 8.9
Measurement D[a]	163.0 ± 57.5	183.1 ± 50.5	-16.0 ± 36.3
Average	172 ± 10	176 ± 6	-2.6 ± 10

[a] Wavelength modulation with second harmonic detection

Measurement A yields the best reproducibility (±9‰), therefore these experimental parameters are the preferred ones. The day-to-day reproducibility over one week is 6‰, even when using different experimental parameters. This reproducibility is comparable to the reproducibility during one day. This represents a considerable improvement with respect to with the free-space DFG-system, where the day-to-day reproducibility was about 30‰. The fiber-coupled systems enables the calibration of the spectrometer and the correcting of the offset of the δ-value. In Figure 43 measurement A is shown after the offset correction.

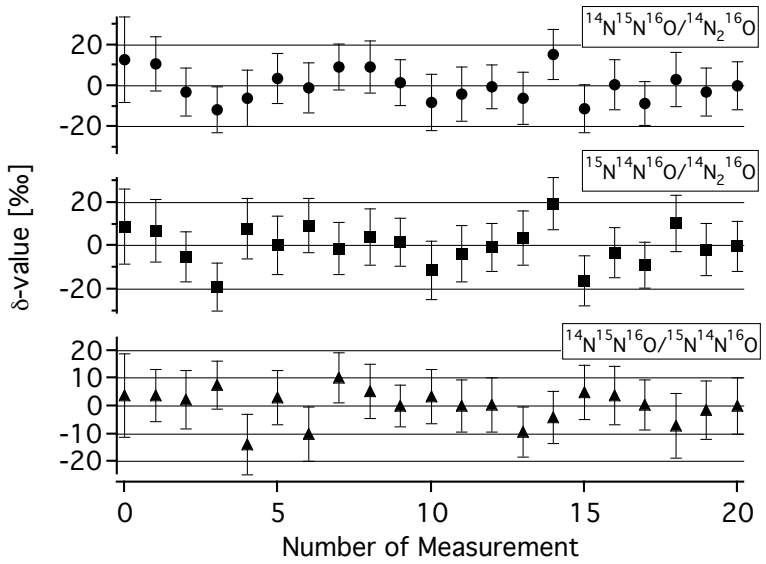

Figure 43: δ-values of measurement A. As the day-to-day reproducibility is good enough, it was possible to correct the offset to zero.

5.3.2 Enriched Samples

In order to test the accuracy of the laser spectrometer with the offset correction, isotopically enriched samples where measured. By comparing the obtained δ-value with the theoretically expected one the accuracy of the system can be determined. Traditionally N_2O is produced by thermal decomposition of ammonium nitrate (Figure 44) at temperatures between 170°C to 260°C. Unfortunately this method yields a high risk of explosion of overheated ammonium nitrate [Mat00, Nei97].

$$NH_4NO_3(aq) \rightarrow N_2O(g) + 2\,H_2O(l) \qquad (60)$$

There is another method though, which does not have the risk of explosion, but also produces rather pure N_2O. The ammonium nitrate is dissolved in a nitric acid (Figure 45) solution together with a small amount of chloride followed by a gentle heating to less than 80°C [Mat00]. The reaction is still the same as before (Eq. 60).

To produce the samples 5 ml 6 M HNO_3, 1 g NH_4NO_3 and 0.05 g NaCl were placed in a test tube and heated until small bubbles appeared (80°C or below). Larger bubbles attributed to boiling water will occur if the solution is overheated. After about ten minutes the gas in the test tube is expected to be more or less pure N_2O, but a slightly brown colour of the gas indicates that also some NO_2 was produced. With a syringe 0.25 ml to 0.5 ml of gas were filled into a glass bottle with air (2 l) to obtain a concentration of about 100 ppm of N_2O in air.

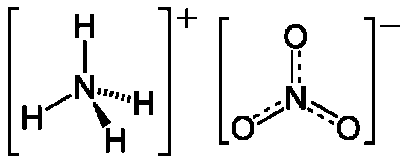

Figure 44: Ammonium nitrate is a chemical compound of NH_4 and NO_3. At room temperature and standard pressure it usually is a white powder.

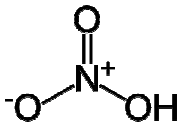

Figure 45: Nitric acid is very similar to one of the compounds of ammonium nitrate.

In order to realize enrichment with respect to the heavy isotope, ammonium nitrate with an increased amount of $^{14}NH_4{}^{15}NO_3$ was used. This is expected to produce preferentially $^{14}N^{15}N^{16}O$ [Nei97], as the ^{15}N sticks to the oxygen atom in the chemical reaction. The ammonium nitrate has 10% of ^{15}N and in order to produce different isotopic compositions this ammonium nitrate was mixed with ammonium nitrate with natural isotopic composition (see Table 20).

Table 20: Isotopic composition of the ammonium nitrate used for N_2O production, calculated and measured δ-value of N_2O. (n.a.: not available)

	Natural abundance [mg]	**^{15}N (10%) [mg]**	**Concentration measured**	**$^{14}N^{15}N^{16}O/^{14}N_2{}^{16}O$ calculated**	**$^{14}N^{15}N^{16}O/^{14}N_2{}^{16}O$ calculated including HNO_3**	**$^{14}N^{15}N^{16}O/^{14}N_2{}^{16}O$ measured**
Sample 1	n.a.	n.a.	74 ppm	n.a.	n.a.	1549‰ ± 67‰
Sample 2	883.2	78.8	93 ppm	2180‰	315‰	316‰ ± 60‰

The sample gas was filled into the multipass cell with a pressure of 50.0 mbar and the isotopic composition was measured with wavelength modulation. After these measurements the multipass cell was filled with natural abundance N_2O (100 ppm) to calibrate the spectrometer. With this calibration the offset of the δ-value was corrected to be zero. The results are listed in Table 20 and shown in Figure 46 and Figure 47.

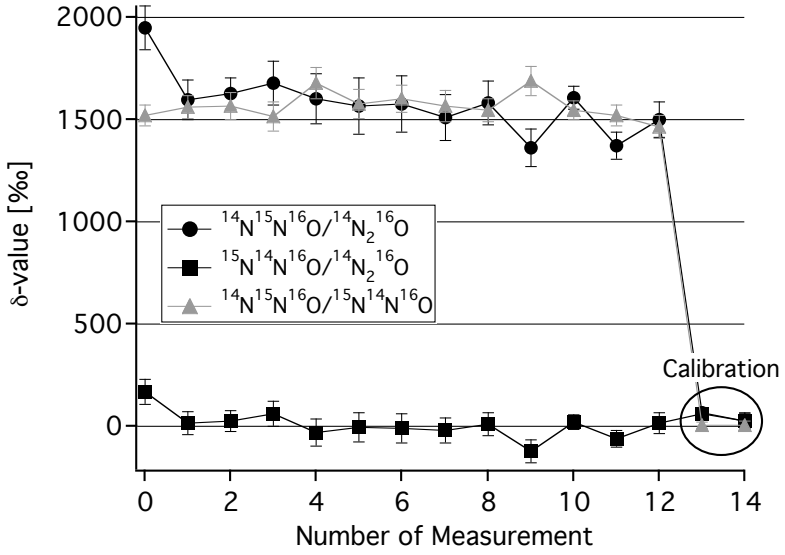

Figure 46: δ-value of enriched sample No. 1. The offset was corrected by measuring the δ-value of a gas sample with natural abundance (data points within circle).

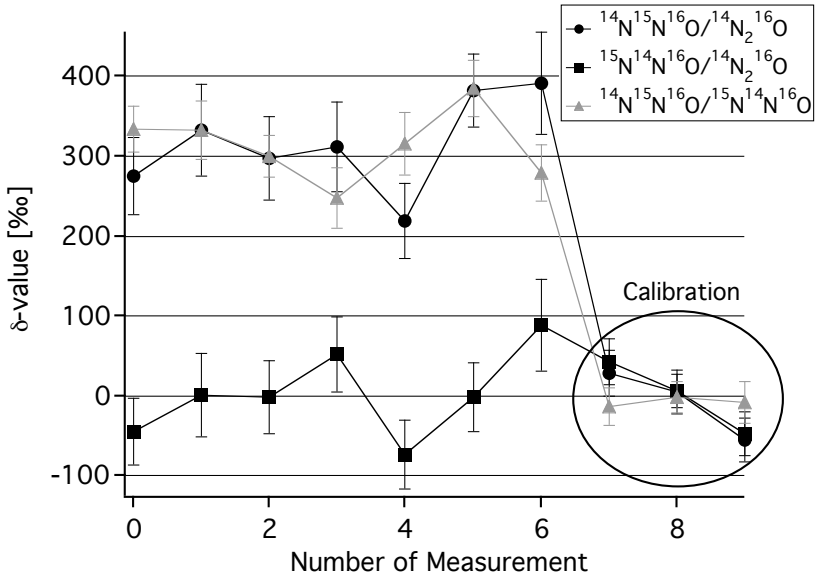

Figure 47: δ-value of enriched sample No. 2. The offset was corrected by measuring the δ-value of a gas sample with natural abundance (data points within circle). The measured enrichment of 316‰ ± 60‰ is in good agreement with the calculations (315‰).

An enrichment only in $^{14}N^{15}N^{16}O$ and not in $^{15}N^{14}N^{16}O$ is observed as expected. The enrichment, however, is about ten times smaller than calculated, when assuming that the N_2O is only produced by the ammonium nitrate (see Table 20). But when ammonium nitrate (NH_4NO_3) is dissolved in nitric acid (HNO_3), the NO_3 part from the latter cannot be distinguished from the first one (compare Figure 44 to Figure 45). This results in a lower

enrichment. When including the nitric acid into the calculations, the calculated δ-value of 315‰ correspond very well with the measured one of 316‰±60‰. The precision of the measurement is worse than before because the power of the Nd:YAG laser has decreased by a factor five caused by degradation.

5.4 Comparison of methods

Different methods were tested in regard of reproducibility of the measured results during one day, day-to-day reproducibility and time resolution (Table 21). The free-space-DFG-system with only sample cell and no reference cell has the worst reproducibility. By using a sample and a reference cell the reproducibility is strongly improved. The only long path systems are rather sensitive to temperature changes, whereas the balanced path length detection schemes are much less prone to temperature changes but have a worse signal-to-noise ratio because the power needs to be split into four beams instead of two. The free-space and the fiber-coupled DFG-systems, both with reference cell, have comparable reproducibilites, but the latter yields a much better day-to-day reproducibility. This is important to correct for the offset. The free-space direct absorption spectroscopy method has the shortest measurement time, yet unfortunately it cannot be used with fiber-coupling because of its low power.

Table 21: Comparison of the different measurement methods. The δ-values of the rare isotope to the main isotope are listed. If it is different for $^{14}N^{15}N^{16}O$ and $^{15}N^{14}N^{16}O$ then the better reproducibility is chosen. (WM: wavelength modulation, direct: direct absorption spectroscopy)

N_2O	Concentration [ppm]	Reproducibility	Day-to-day reproducibility	Measurement time
Free-space, one cell, direct	2040	220‰	200‰	20 min
Free-space, only long path, WM	825	6‰ with temperature change: 18‰	30‰	20 min
Free-space, balanced, WM	825	10‰	40‰	20 min
Free-space, only long path, direct	825	15‰	28‰	15 sec to 6 min
Free-space, balanced, direct	825	6‰	–	15 sec to 6 min
Fiber coupled, WM	100	9‰	6‰	12 min

5.5 Conclusion

For the first time the isotopic composition of N_2O was measured with laser spectroscopy at trace gas level. Until now laser spectroscopic isotope measurements of N_2O were only performed in pure samples. Gagliardi et al. [Gag05] obtained a precision of ±9‰ with a cryogenically cooled quantum cascade laser at 8 μm. This precision is worse than what has been achieved in this thesis. Uehara et al. [Ueh03a, Ueh03b] obtained a precision of ±0.3‰ with a diode laser at 2 μm. This is better than the precision obtained in our studies. However, the absorption lines at those wavelengths are rather weak, which limits the measurement to high concentrations, whereas concentrations in the ppm-range are accessible with our setup.

Two different measurement methods, wavelength modulation and direct absorption spectroscopy, were tested in combination with two different detection schemes, namely balanced path length and only long path detection. On the one hand, direct absorption spectroscopy with balanced path length detection was the most promising method owing to its low temperature sensitivity and its good time resolution, but its precision was not sufficient. On the other hand, wavelength modulation with only long path detection yielded a good precision (3‰) and a good reproducibility (6‰), but was strongly temperature sensitive and needed a long measurement time. The fiber-coupled system with balanced path length detection and wavelength modulation yields the best day-to-day reproducibility (6‰) and a precision (8‰) comparable to the free-space system. Now it is possible to correct the offset of the measured δ-values and compare measurements from different days. Enriched samples were produced from enriched ammonium nitrate and were measured with the offset-corrected system. The measured δ-values correspond very well to the calculated ones within the measurement precision.

There are two main problems, which currently limit the precision and reproducibility. The first is related to the external cavity diode laser (ECDL) whose side-mode suppression was not sufficient anymore. This caused sudden mode-hops and deteriorated the reproducibility of the measurements.

The second problem is related to the low signal-to-noise ratio of the detector signals, which is related to the low laser power available. Hence, the precision and reproducibility could be substantially improved by higher laser powers preferentially in the mW range and stable laser emission. Future near-room-temperature cw QCLs around 4.6 μm with broader tunability appear very promising in this respect. Another possibility would be DFG with a waveguide nonlinear crystal, offering much higher conversion efficiency because of better confinement of the laser beams, once they become commercially available for the needed wavelengths.

The measurements presented here are performed at ppm concentration of N_2O. For e.g. CO_2 this would be sufficient for ambient air experiments but not for N_2O, as the ambient concentration is about 314 ppb. Higher laser power and more sensitive detection schemes,

e.g. cavity ringdown, are required to achieve such low detection limits in combination with improved precisions.

Some of the results presented here are published in [Wae06] and [Wae07a].

6. Carbon Monoxide (CO) isotope measurements

6.1 Single cell configuration: Setup, method and results

First measurements of CO isotopes were made with the setup described in chapter 4.7.1. We determined the isotope ratios $^{13}C/^{12}C$ and $^{18}O/^{16}O$ of CO in a sample collected from the exhaust of a scooter by using balanced path length detection. The CO concentration amounted to 200 ppm and the results are shown in Figure 48. The measurements were again done at a reduced gas pressure of 50 mbar to avoid overlapping of the absorption lines. For analyzing the measurements a Voigt function is fitted to the absorption lines. The concentration is again determined by using the area under the Voigt line and the known line strength. By comparing the concentrations of the main and the less abundant isotope the isotopic ratio is calculated.

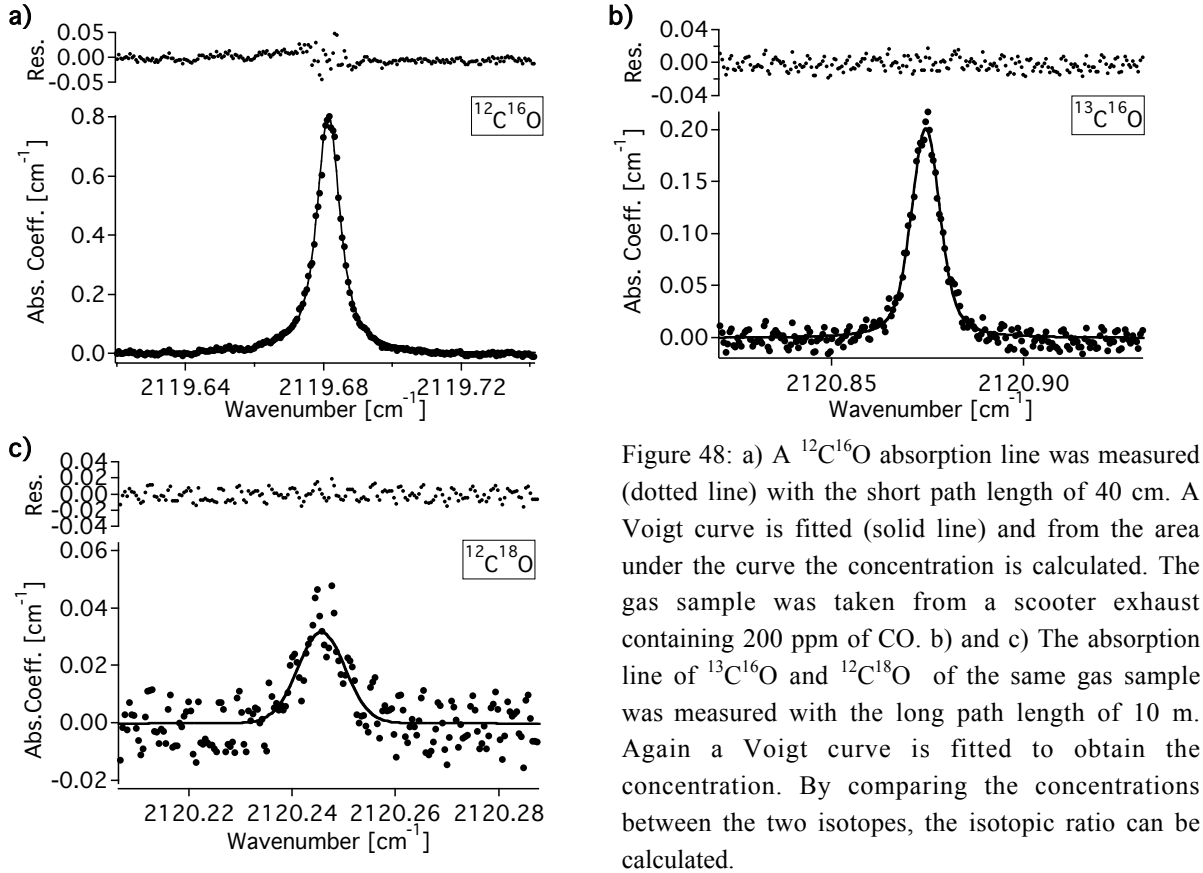

Figure 48: a) A $^{12}C^{16}O$ absorption line was measured (dotted line) with the short path length of 40 cm. A Voigt curve is fitted (solid line) and from the area under the curve the concentration is calculated. The gas sample was taken from a scooter exhaust containing 200 ppm of CO. b) and c) The absorption line of $^{13}C^{16}O$ and $^{12}C^{18}O$ of the same gas sample was measured with the long path length of 10 m. Again a Voigt curve is fitted to obtain the concentration. By comparing the concentrations between the two isotopes, the isotopic ratio can be calculated.

The results for the isotope ratios are listed in Table 22. They agree with the natural abundance ($^{13}C^{16}O/^{12}C^{16}O$ = 1.1%, $^{12}C^{18}C/^{12}C^{16}O$ = 0.20%) [Hitran05]. The measurement precision, however, is not sufficient to distinguish, e.g., between CO of natural origin or of CO originating from a combustion process like in this example. For fossil fuel combustion a δ-value of $\delta^{13}C$ = –27.8‰ and $\delta^{18}O$ = 23.5‰ is expected [Gro02]. With high-precision measurements even different fuels can be distinguished, e.g. for gasoline automobiles $\delta^{13}C$ = –23.8‰ and $\delta^{18}O$ = 25.3‰ have been reported, compared to diesel automobiles with $\delta^{13}C$ = –19.5‰ and $\delta^{18}O$ = 15.1‰ [Tsu03].

Table 22: Measurements of isotopic ratios and δ-values in different trace gases with our DFG system and multipass cell. To calculate the δ-values the measured isotope ratios are compared to the natural abundances.

	Only long path	**Balanced path length**
Isotope ratios	—	$^{13}C^{16}O/^{12}C^{16}O$: 1.1% ± 0.2% $^{12}C^{18}O/^{12}C^{16}O$: 0.16% ± 0.03%
δ-value	—	$\delta(^{13}C^{16}O)$: 0‰ ± 180‰ $\delta(^{12}C^{18}O)$: –200‰ ± 150‰

6.2 Dual cell configuration: Setup, methods and results

6.2.1 Experimental arrangement and gas samples

Since the line strengths of the selected lines of the main isotope and the less abundant one are also very different in the case of CO as for N_2O, we used balanced path lengths where the main and the rare isotopes are measured at two different path lengths. In contrast to N_2O measurements with only long path length are not feasible (see chapter 4.6). To improve the precision of the measurement the isotopes were again measured simultaneously in the sample cell and in a single pass reference cell as described in chapter 4.7.2.

The measurements were all made at room temperature and at a total gas pressure of 50 mbar. The CO concentration in the reference cell was 2% whereas the CO concentration in the sample cell was 300 ppm, both taken from another certified mixture.

6.2.2 Methods

As for N_2O, two different measurement methods were compared, wavelength modulation with first harmonic detection and direct absorption spectroscopy by recording the spectrum with a data acquisition card. The measurement parameters were the same as for N_2O except that 10^3 scans were averaged for long path measurements of $^{13}C^{16}O$, $5 \cdot 10^4$ scans for long path measurements of $^{12}C^{18}O$ and 10^4 scans for short path measurements of $^{12}C^{16}O$, which is more than for N_2O because of the lower laser power at the longer wavelengths (see chapter 3.3.1). From these measurements a moving average over 11 data points was taken.

6.2.3 Data evaluation

The wavelength modulation measurements were evaluated the same way as for N_2O (see section 5.2.3). Figure 49 shows an example of such a measurements and a plot of the sample detector signal versus the reference detector signal with a fit as defined in Eq. (58).

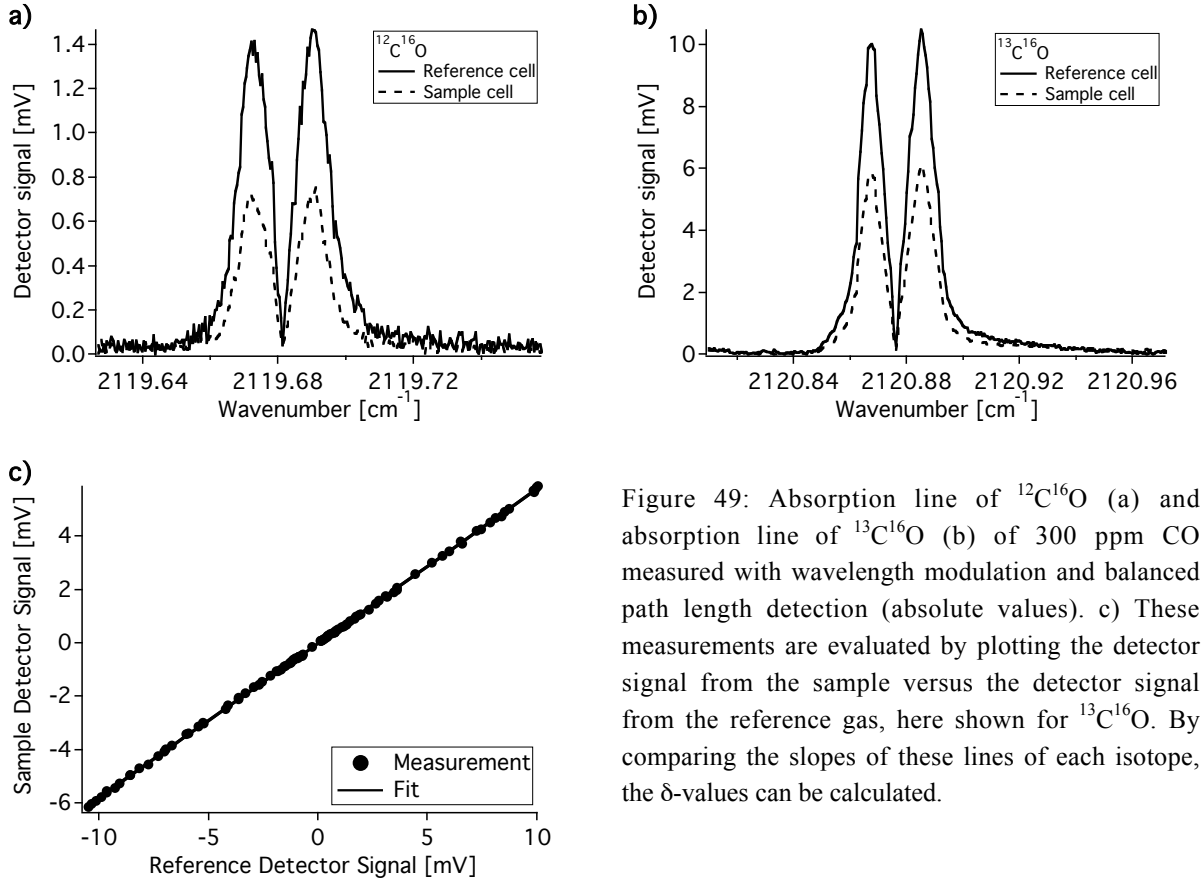

Figure 49: Absorption line of $^{12}C^{16}O$ (a) and absorption line of $^{13}C^{16}O$ (b) of 300 ppm CO measured with wavelength modulation and balanced path length detection (absolute values). c) These measurements are evaluated by plotting the detector signal from the sample versus the detector signal from the reference gas, here shown for $^{13}C^{16}O$. By comparing the slopes of these lines of each isotope, the δ-values can be calculated.

To evaluate the measurements with the data acquisition card the dark current or voltage and the background must also be measured. Normally this is done before or after the actual gas measurement, as it was done for the N_2O measurements. However for these CO measurements, since the detectors exhibit a strong drift in the dark current, a chopper was used to block the beam after the wavelength was swept across the absorption line (see Figure 50). This way the dark current and the laser power can be measured simultaneously with the spectrum and an improvement of the precision is expected and actually also achieved. To obtain the background a polynomial of fourth order was fitted to the measured spectrum by leaving out the absorption line.

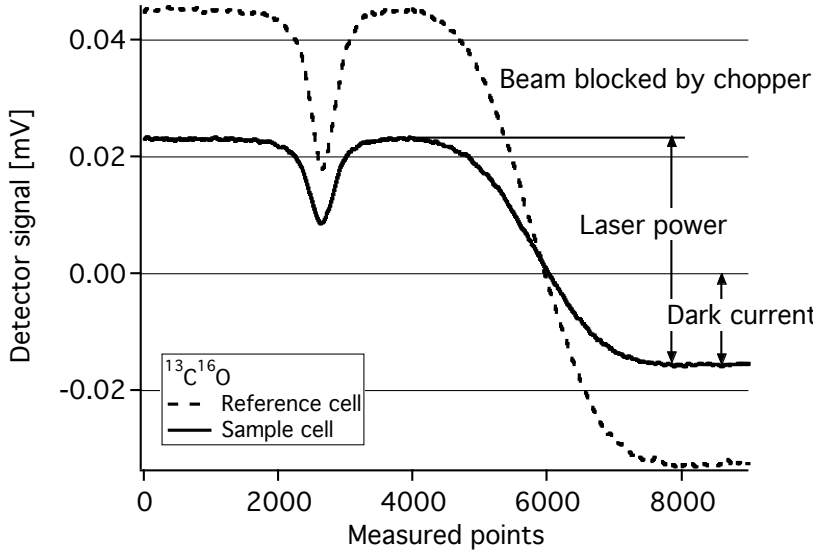

Figure 50: Detector signals of sample and reference cell at wavelength for $^{13}C^{16}O$ (300 ppm CO in synthetic air), recorded with a data acquisition card and averaged over 1000 scans. The wavelength is scanned over the absorption line and simultaneously the laser power is modulated with a chopper. This way the dark voltage and the laser power are measured simultaneously.

After normalizing the spectrum with the background the absorption coefficient was calculated. By comparing the peaks of the absorption lines the isotope ratio was determined. These measurements were repeated 100 times and a moving average over 11 points was taken.

6.2.4 Results and discussion

Both measurement methods were tested regarding the reproducibility and measurement time. A short-term reproducibility of 5‰ for $^{13}C^{16}O/^{12}C^{16}O$ and 11‰ for $^{12}C^{18}O/^{12}C^{16}O$ were achieved at a CO concentration of 300 ppm (Figure 51), when using wavelength modulation

and balanced path length detection. With direct absorption spectroscopy a short-term reproducibility of the δ-value of 12‰ for $^{13}C^{16}O/^{12}C^{16}O$ and 11‰ for $^{12}C^{18}O/^{12}C^{16}O$ were obtained for the same concentration (Figure 52). The results are shown in Table 23. The wavelength modulation technique has the better reproducibility but it takes 20 minutes to measure all three isotopes. In comparison, direct absorption spectroscopy with the data acquisition card is much faster, it takes only about 6 minutes to measure three different isotopes. The disadvantage of this method is its worse reproducibility compared to wavelength modulation. The reasons for the bad reproducibility are the same as in the case of the N_2O measurements: Low signal-to-noise ratio, variation in the detector response because of ice-layer build-up and insufficient side-mode suppression of the external cavity diode laser.

Another problem concerns the accuracy of the δ-value. It is expected to be close to zero because the gas in the sample cell and in the reference cell are both from certified gas mixtures from the same company, and therefore the isotopic composition should be about the same for the two gas mixtures. Like for N_2O (see Table 23), there is a large offset, which also depends on the measurement method. Explanations for this offset are described in section 5.2.4. When the day-to-day reproducibility is good enough this offset can be measured once and then subsequent measurements can be corrected as it was done for N_2O measurements presented in chapter 5.3.

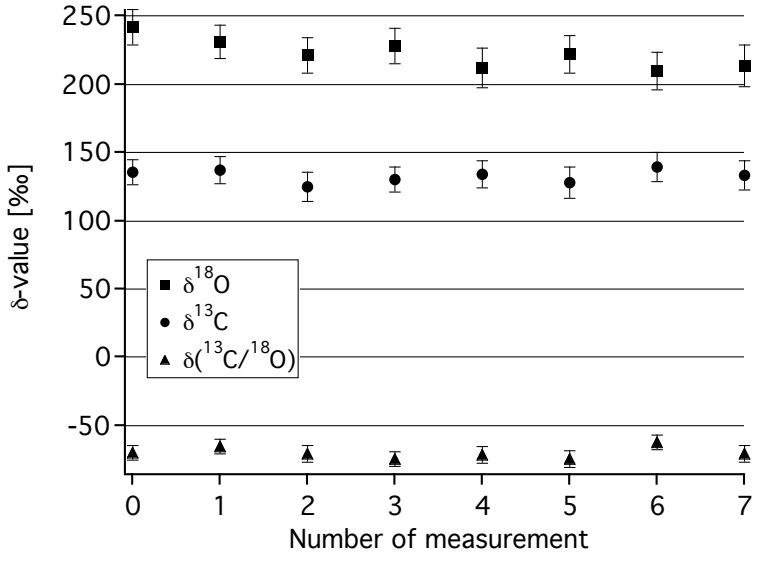

Figure 51: δ-value of $^{13}C^{16}O$ and $^{12}C^{18}O$ measured with wavelength modulation.

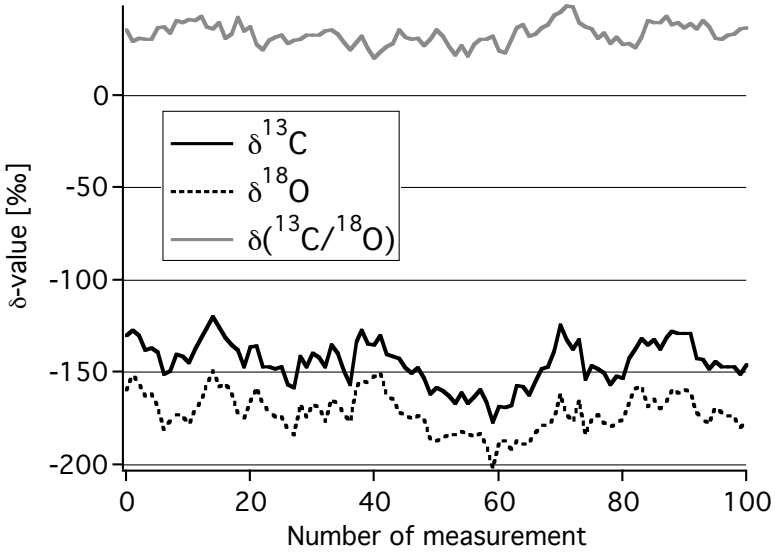

Figure 52: δ-value of $^{13}C^{16}O$ and $^{12}C^{18}O$ measured with the data acquisition card (DAQ) smoothed with a moving average over 11 points.

Table 23: Results of isotope ratio measurements of CO using wavelength modulation (WM) or direct absorption spectroscopy.

Method	**δ(^{13}C) [‰]**	**Repr. δ(^{13}C) [‰]**	**δ(^{18}O) [‰]**	**Repr. δ(^{18}O) [‰]**	**δ(^{13}C/^{18}O) [‰]**	**Repr. δ(^{13}C/^{18}O) [‰]**
Direct absorption spectroscopy	–145	12	–172	11	33.1	5.7
Wavelength modulation	133	4.7	222	11	–70.0	4.2

6.3 Comparison of methods

Different methods were compared regarding the reproducibility of the measurements during one day, the day-to-day reproducibility and time resolution, an overview of the results is listed in Table 24. The free-space-DFG-system with only a sample cell and no reference cell has the worst reproducibility. By using a sample and a reference cell the reproducibility is improved considerably. Measurements using only the long path are not possible for CO (see chapter 4.6), therefore only the balanced path length detection scheme was tested. Direct absorption spectroscopy yields the best performance regarding reproducibility, day-to-day reproducibility and time resolution.

Table 24: Comparison of the different measurement methods. The d-values for the rare isotope to the main isotope are listed. If they are different for $^{13}C/^{16}O$ and $^{18}O/^{16}O$ then the better reproducibility is chosen. (WM: wavelength modulation, direct: direct absorption spectroscopy)

CO	Concentration [ppm]	Reproducibility	Day-to-day reproducibility	Measurement time
Free-space, single cell, balanced, direct	200	150‰	160‰	20 min
Free-space, reference cell, balanced, WM	300	11‰	30‰	20 min
Free-space, reference cell, balanced, direct	300	4.7‰	15‰	6 min

6.4 Conclusions and outlook

For the first time laser spectroscopic measurements with precisions of a few ‰ were made with isotopes of CO at ppm concentrations. The laser spectrometer is based on difference-frequency generation as laser source and a balanced path-length detection scheme using a multipass cell and a single pass reference cell, each offering two different path lengths. The temperature sensitivity of the δ-value is less than 0.058‰/K for $^{13}C/^{12}C$ and less than 0.36‰/K for $^{18}O/^{16}O$, therefore no active temperature stabilization is needed. Two different measurement methods were compared, wavelength modulation and direct absorption spectroscopy. Wavelength modulation yields the better reproducibility (4‰) but needs longer measurement times. Direct absorption spectroscopy is faster but the reproducibility is worse (11‰).

Until now laser spectroscopic measurements of CO isotopes were only performed by Lee et al. [Lee91] at a lower concentration (2.4 ppm) but with much worse precision (±450‰). Their system is based on a lead salt diode laser, which needs cryogenic cooling, whereas the system presented here operates at room temperature, except for the liquid nitrogen cooled detectors, which could be replaced by thermoelectric cooled ones.

The two main problems limiting the reproducibility are the degradation of the external cavity diode laser (ECDL) and the low signal-to-noise ratio of the detectors. The side-mode suppression of the ECDL is not sufficient anymore, which causes sudden mode hops and lowers the reproducibility. The cw DFG-system generates only low power and when splitting the beam into four beams, which are needed for the two different path lengths in the sample and the reference cell, the signal-to-noise ratio of the detectors is decreased even more, which

results in a bad reproducibility. Hence by increasing the laser power the performance of the spectrometer can certainly be substantially improved.

The results presented here are published in [Wae06] and [Wae07b].

7. General discussion

The reproducibility of the δ-value of the instrument presented in this thesis is not yet good enough to measure the differences in isotopic composition in nature. The reproducibility of the δ-value is often worse than the precision of a single measurement indicating a large potential for improvements. In addition to this, some other effects have been observed also reducing the reproducibility and accuracy of the instrument. For example, the δ-value exhibits sometimes a drift (Figure 53) and sudden changes in the background signals were observed (Figure 54). In this chapter possible explanations will be discussed and further improvements will be proposed.

First of all there is sometimes a strong drift in the δ-value, which stabilizes after a while (see Figure 53). The drift is the strongest for CO isotope measurements and much smaller in the case of N_2O and CO_2 isotope measurements. It cannot be explained by temperature changes of the gas because for CO the temperature sensitivity is negligible ($\Delta\delta / \Delta T = 0.06‰/K$ for $^{13}C/^{12}C$, see chapter 4.6.2) and considerably smaller than for N_2O and CO_2.

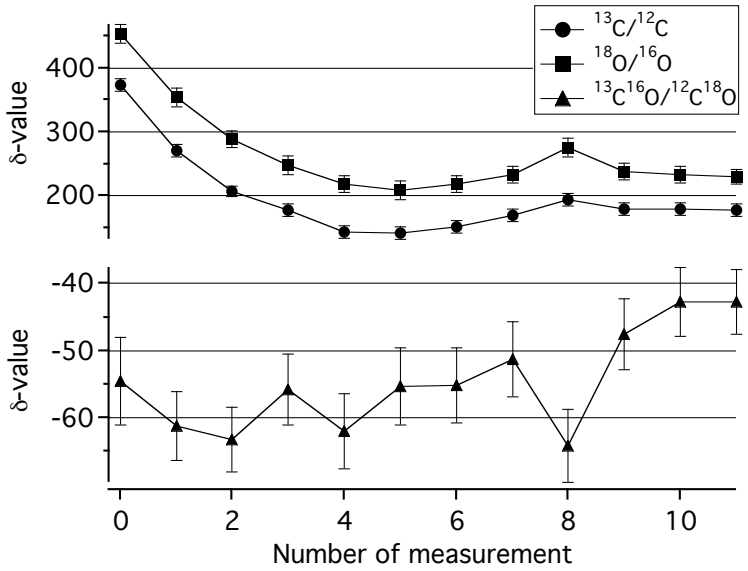

Figure 53: Repeated measurements of δ-value of CO. It has a strong drift and then stabilizes on a certain value. Wavelength modulation and balanced path length was implemented for these measurements and the sample gas concentration was 300 ppm CO.

In contrast to CO_2, CO is a polar molecule and therefore adsorption and desorption of the gas molecules on the walls of the cell might influence the measurement. Another explanation are pressure and the concentration changes during the measurement due to leakage of the gas

cells. Variation in concentration (leakage, adsorption-desorption processes) can be expected to be the same for all CO isotopes, and should therefore cancel out and not influence the δ-value. Pressure changes are also the same for all CO isotopes but the line shape of different absorption lines may be affected differently resulting in a drift of the δ-value, especially when the pressure changes in the reference and sample cell are not the same.

As all these processes are rather slow and only moving in one direction, strong drifts in the measured δ-value as shown in Figure 53 can be explained but not sudden changes in the background and signal ratio as depicted in Figure 54. Such abrupt changes are not only observed in the δ-value and in background measurements (Figure 54) but also in concentration measurements of atmospheric CO (Figure 55). To test the reproducibility of the background measurements, the detector signals were recorded during five hours while keeping the wavelength fixed (Figure 54). The power fluctuations look the same on both detectors resulting in a stable ratio of the two signals, except for a sudden change by 1.5%. Apart from this change the ratio is stable. This change in the ratio is not correlated to any wavelength change of the laser, as there is only a very small wavelength drift of 2 pm during 5 hours (see lowest part of Figure 54).

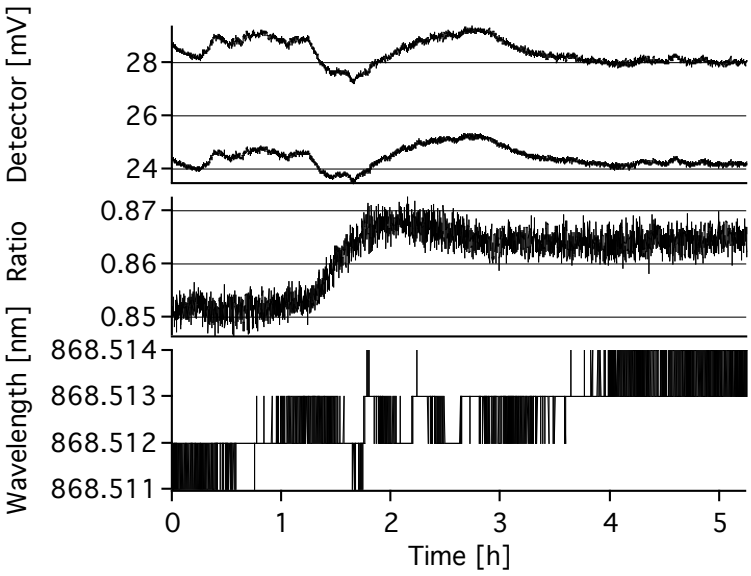

Figure 54: Signals on detectors is recorded during five hours while keeping the wavelength of the laser fixed. The power fluctuations on the detectors look the same but the ratio of the signals yields a sudden change of 1.5%.

A similar effect was observed during a measurement of CO in ambient air. The absorbance of the same sample was measured several times and after six measurements the value suddenly changed (see Figure 55). This effect has probably the same origin as the sudden change in the detector signal ratio.

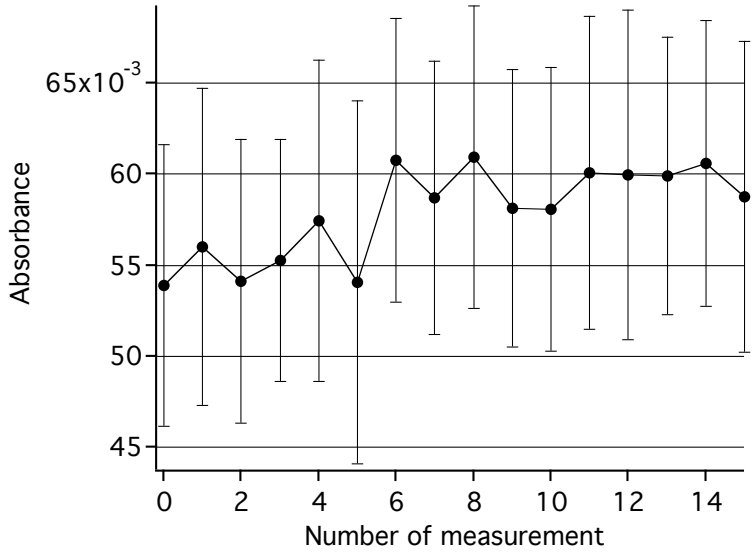

Figure 55: Measurements of the absorbance of CO in ambient air. The measured value makes a sudden change after the sixth measurement.

A possible explanation is the degradation of the external cavity diode laser (ECDL). New mode-hops appeared from time to time and there were more and more wavelength regions where it ran multimode indicating an insufficient side-mode suppression. A suddenly increasing side-mode could explain changes in the ratio (Figure 54) and in the measured absorbance (Figure 55) because a side-mode exhibits another wavelength and therefore the etalon effect from beam splitters, windows and lenses is different for the side-mode. To solve this problem the laser diode has been replaced but unfortunately the new diode had an even worse side-mode suppression than the previous one.

Also the quality of the infrared detectors has a strong influence on the reproducibility of the measurements. The detectors are liquid nitrogen cooled and if the vacuum inside is not good enough, an ice layer can build up. This layer acts as a dielectric coating on the windows and the detector itself resulting in changes of the transmission of the light to the detector due to etalon effects and the strong absorption of mid-infrared light in ice. Variation of the thickness of this ice layer may therefore cause variations in the measurements reducing the reproducibility. To avoid this problem the detectors should be evacuated regularly [The05, The06]. However, even when this was done, the reproducibility was not improved. If higher laser power was available this problem could be circumvented by using thermoelectrically cooled detectors, where no ice layer builds up.

8. Conclusion and Outlook

The aim this thesis was to develop a laser spectrometer to measure isotope ratios ($^{13}C/^{12}C$, $^{18}O/^{16}O$ and $^{15}N/^{14}N$) of CO_2, CO and N_2O at trace concentrations with precisions better than 1‰. It should be a single instrument for all three gases, several isotopes should be measurable for each molecule and no pretreatment should be needed.

The molecules of interest have their strongest absorption lines in the mid-infrared between 4.3 μm and 4.7 μm. As there is no commercial laser system available covering the needed wavelength range with one instrument, a laser source was built on the basis of difference frequency generation (DFG). MgO-doped periodically poled $LiNbO_3$ was used as nonlinear crystal, an external cavity diode laser (ECDL, 820 nm – 870 nm, 120 mW) as pump laser and a Nd:YAG laser as signal laser (1064 nm, 2 W). Theoretical calculations were performed to determine the optimal beam parameters and the optimal crystal lengths with respect to the wavelength dependent absorption of the crystal. This system covers the desired wavelength range, delivers a laser power of 23 μW to 5 μW and has a narrow line width of 1 MHz. A second, fiber-coupled DFG-system was built to have a more compact and robust system. Its advantage is the better beam shape of the idler beam yielding a better stability of the spectrometer, yet on cost of a reduced power (0.26 μW) because of fiber-coupling losses.

Two different setups were tested: A single-cell setup and a dual-cell setup where the isotopes were measured simultaneously in a sample and a reference cell. These setups were used in two configurations, an only long path detection scheme, which is more temperature sensitive but yields the better signal-to-noise ratio, and a balanced path length detection, which is less temperature sensitive but has a lower signal-to-noise ratio because the light is split into four beams instead of two. Two different measurement techniques were compared, direct absorption spectroscopy and wavelength modulation. Also two different DFG systems were tested, free-space and fiber-coupled. Various combinations of setups, detection schemes and measurement methods were evaluated by measuring the isotopic composition of N_2O, CO and CO_2 in the ppm-range.

Nitrous oxide (N_2O) is of special interest for laser spectroscopy because the two isotopes $^{14}N^{15}N^{16}O$ and $^{15}N^{14}N^{16}O$ cannot be measured with mass-spectrometry directly, as they have the same mass. In contrast, laser spectroscopy can easily differentiate between them, as the positions of their absorption lines are very different. Laser spectroscopic determination of isotope ratios was done with N_2O concentrations between 100 ppm and 2040 ppm. The best precision was obtained by using the dual cell arrangement. As long as there was no large temperature change the results for only long path detection (direct absorption spectroscopy: ±5‰, wavelength modulation: ±6‰) and balanced path length detection (direct absorption spectroscopy: ±11‰, wavelength modulation: ±6‰) were similar. But small temperature

changes have a strong influence when using only long path detection. This reduces the precision of the measurement, e.g., for wavelength modulation it increases to ±18‰. The best day-to-day reproducibility (±6‰) was obtained by using the fiber-coupled DFG-system in combination with balanced path length detection and wavelength modulation. The precision (±9‰, wavelength modulation, balanced path lengths) of this system was comparable to the dual cell configuration in combination with the free-space DFG laser source. With this system measurements on isotopically enriched samples were performed and the results were in good agreement with calculations (measured 316‰±60‰, calculated: 315‰). The time resolution is better for direct absorption spectroscopy in combination with the data acquisition card (15 sec to 6 min) than for wavelength modulation (20 min). The worst precision (±220‰) was obtained by using a single gas cell and balanced path length detection, when using only long path detection the precision was considerably better (±30‰).

The reasons for the bad precision may be the limited resolution of the wavemeter and the limited accuracy of the line strengths reported in literature. These problems could be solved by using an etalon for wavelength measurements and by determining the line strength by a high-precision measurement of a calibrated gas sample. Another point is that temperature variations have a much stronger influence for this setup than for the dual-cell setup because in the latter case the temperature difference between the cells is important, whereas in the first case it is the temperature difference from one measurement to the next one. The precision is much better for the dual-cell arrangements but still not as good as required for field measurements (±0.1‰). Reasons for this shortcoming might be the low signal-to-noise ratio on the detectors, pressure changes and temperature changes during the measurements. The last point should have less influence in the case of balanced path length detection, but as the optimum absorption line combination could not be chosen because of the limited computer controlled tuning range of the laser, the temperature sensitivity is still $\Delta\delta / \Delta T = 8‰$. This value is comparable to the precision of the dual-cell measurement and to the day-to-day reproducibility of the fiber-coupled system. A possible improvement of the precision would be high precision measurements of pressure and temperature for correcting the evaluation of the measured isotope ratios. A further problem that also reduces the reproducibility is that the external cavity diode laser had an insufficient side-mode suppression due to degradation.

Until now laser spectroscopic isotope measurements of N_2O were only performed in pure samples. Gagliardi et al. [Gag05] obtained a precision of ±9‰ with a cryogenically cooled quantum cascade laser at 8 μm. This precision is worse than that reached in this thesis. Uehara et al. [Ueh03a, Ueh03b] obtained a precision of ±0.3‰ with a diode laser at 2 μm. This is better than the precision achieved in our studies. However, the absorption lines at these wavelengths are rather weak, which limits the measurement to high concentrations, whereas concentrations in the ppm-range are accessible with our setup.

Carbon monoxide (CO) can only be measured with balanced path length detection because CO does not have suitable weak absorption lines close to the strong absorption lines of the less abundant isotopes. Measurements of $^{13}C/^{12}C$ and $^{18}O/^{16}O$ were done again with different combinations of setups and measurement methods with CO concentrations of 200 ppm and 300 ppm. The best precision (±5‰) was obtained with the dual-cell setup and direct absorption spectroscopy, with wavelength modulation the precision was slightly worse (±11‰). The worst precision (±150‰) was obtained when using the single cell arrangement. The gas sample for this measurement was taken from an exhaust of a scooter, but the precision was not good enough to recognize any deviations in the isotope ratio to the natural abundance.

The reasons for the bad precision are essentially the same as for N_2O. A considerable difference to N_2O is the much lower temperature sensitivity ($\Delta\delta / \Delta T < 0.4‰$), which makes the measurement nearly temperature independent. This might be an explanation why the precision for CO is similar or even better than for N_2O, despite the lower idler power and weaker absorption lines.

Until now laser spectroscopic measurements of CO isotopes were only performed by Lee et al. [Lee91] at a lower concentration (2.4 ppm) but with much worse precision (±450‰). Their system was based on a lead salt diode laser, which needs cryogenic cooling, whereas the system presented here operates at room temperature, except for the liquid nitrogen cooled detectors, which could be replaced by thermoelectric cooled ones.

Carbon dioxide (CO_2) isotope ratios were measured in the near infrared with cavity ringdown detection and in the mid-infrared with the single cell setup. As the absorptions lines in the near-infrared are rather weak, high concentrations of 50% CO_2 in air were needed. With this detection scheme a precision of ±45‰ was obtained. In the mid-infrared the absorption lines are much stronger and therefore ambient indoor air with a CO_2 concentration of 450 ppm was used. With the single cell setup a precision of ±180‰ for only long path and ±270‰ for balanced path length were obtained. Measurements with the dual-cell arrangement were not performed, because the absorption in the air surrounding the gas cells is rather strong and influences the measurement. In the case of the single cell, the path lengths outside the cell was the same for the beam passing through the sample gas and the beam propagating directly to the reference detector. Therefore the influence of the outside air is cancelled out. For the dual-cell configuration, however, the path lengths outside the cells were very different which would require the building of a box around the beams paths flushed with CO_2-free air. With this configuration, similar or even better precision as for N_2O and CO can be expected because of higher idler power and stronger absorption lines. Furthermore, the problem of adsorption and desorption processes is less pronounced for CO_2 than for N_2O and CO owing to the lack of a molecular dipole moment.

For CO_2, many isotope measurements with laser spectroscopy are reported in literature, but again often high concentrations were needed or low precisions were obtained and many groups only measured one isotope ratio, mainly $^{13}C/^{12}C$ and not two or more as it is

performed in this thesis. However, the best results were obtained by McManus et al. [Man05] with ±0.18‰ for $^{13}C/^{12}C$ and by Tuzson et al. [Tuz07] with ±0.16‰ for $^{13}C/^{12}C$ and ±0.28‰ for $^{18}O/^{16}O$, both at ambient concentration of CO_2. This is better than the results reported here, but both systems are much more sophisticated. They are equipped with a high-precision temperature stabilization and a complicated data evaluation, which includes measured temperature and pressure changes. At the same time this shows the potential of the setup presented here. By using a stronger light source, e.g. by implementing a waveguide PPLN, and implementing better pressure and temperature control, similar precisions should be possible.

Another important issue is the accuracy of isotope measurements. Even for isotope-ratio mass-spectrometry (IRMS), the standard method, different results are obtained by different instruments for the same samples [Cop06]. Also for laser spectroscopic measurements the accuracy needs to be determined, because depending on setup, measurement method and data evaluation there can exist a considerable offset between instruments. Also our setup has a large offset, but the day-to-day reproducibility of the fiber-coupled version is good enough to correct it. Measurements with enriched samples are in good agreement with calculations demonstrating a good accuracy within the measurement precision.

In conclusion, we presented isotope measurements with laser spectroscopy of $^{15}N/^{14}N$ in N_2O, of $^{13}C/^{12}C$ and $^{18}O/^{16}O$ in CO and CO_2, all at ppm concentrations. It is the first time that the isotope ratios of N_2O and CO were measured with laser spectroscopy at ppm concentrations with a precision of a few ‰. In contrast to other setups, where only one molecule and often only one isotope ratio can be measured, it is possible to measure three different molecules (CO_2, CO, N_2O) with at least two different isotope ratios for each with a single device. As our measurements with different detection methods, cell configurations, data acquisition, etc. imply there is no optimum arrangement that fulfills all requirements in terms of precision, reproducibility and time resolution simultaneously. The best time resolution is obtained with direct absorption spectroscopy and recording the data with the data acquisition card and the smallest temperature sensitivity with balanced path length detection. The best precision in δ-value is obtained with the dual-cell setup, direct absorption spectroscopy and only long path, if there is no gas temperature change, else with balanced path length detection (CO). In general, the detection limit and precision still need to be improved for field measurements, as concentrations in the ppb-range and precisions smaller than ±0.1‰ are required. To reach lower concentrations, more sensitive detection schemes like cavity ringdown would be preferable. Its successful implementation, however, would require higher laser power.

One possibility for higher power would be difference frequency generation with a waveguide nonlinear crystal yielding enhanced conversion efficiency because of better confinement of the laser beams. However, PPLN waveguides are not yet commercially available for the needed wavelength ranges. Other crystals like stoichiometric Lithium Tantalate (SLT) or GaAs have lower or no absorption at the desired wavelengths and would

therefore be an interesting alternative once periodic poling (SLT) or orientation patterning (GaAs) is available. Since shortly continuous wave quantum cascade laser with external cavity (EC-QCL) operating at room temperature are becoming available, such an EC-QCL around 4.7 μm also represents a promising alternative. Another possibility is an optical parametric oscillator (OPO), as recent developments extended the mode-hop free and computer controlled wavelength range [Nga06]. But the wavelength range of the commercially available devices is usually limited to wavelengths shorter than 4.4 μm because of the strong absorption of $LiNbO_3$ at longer wavelengths making it difficult to reach the pump threshold.

References

[Ada99] J.J. Adams, C. Bibeau, R.H. Page, D.M. Krol, L.H. Furu, and S.A. Payne, *4.0–4.5 μm lasing of Fe:ZnSe below 180 K, a new mid-infrared laser material*, Opt. Lett. **24**, 1720-1722 (1999)

[Ama05] A. Amann and D. Smith, Eds., *Breath Analysis for Clinical Diagnosis and Therapeutic Monitoring*, World Scientific (Singapore, 2005)

[And84] D.Z. Anderson, J.C. Frisch and C.S. Masser, *Mirror reflectometer based on optical cavity decay time*, Appl. Opt. **23** (8), 1238-1245 (1984)

[App7] *Application note 7: FM Spectroscopy with Tunable Diode Lasers*, New Focus, San Jose, www.newfocus.com (2007)

[Bak04] Y.A. Bakhirkin, A.A. Kosterev, C. Roller, R.F. Curl and F.K. Tittel, *Mid-infrared quantum cascade laser based off-axis integrated cavity output spectroscopy for biogenic nitric oxide detection*, Appl. Opt. **43**, 2257-2266 (2004)

[Bar06] T. le Barbu, B. Parvitte, V. Zeninari, I. Vinogradov, O. Korablev and G. Durry, *Diode laser spectroscopy of H_2O and CO_2 in the 1.877-μm region for the in situ monitoring of the Martian atmosphere*, Appl. Phys. B **82**, 133-140 (2006)

[Ber94] P. Bergamaschi, M. Schupp and G.W. Harris, *High-precision direct measurements of $^{13}CH_4/^{12}CH_4$ and $^{12}CH_3D/^{12}CH_4$ ratios in atmospheric methane sources by means of a long-path tunable diode laser absorption spectrometer*, Appl. Opt. **33** (33), 7704-7716 (1994)

[Ber00] G. Berden, R. Peeters and G. Meijer, *Cavity ring-down spectroscopy: Experimental schemes and applications*, Int. Rev. Phys. Chem. **19** (4), 565-607 (2000)

[Bli06] D.F. Bliss, C. Lynch, D. Weyburne, K. O'Hearn and J.S. Bailey, *Epitaxial growth of thick GaAs on orientation-patterned wafers for nonlinear optical applications*, J. Cryst. Growth **287**, 673-678 (2006)

[Blu02] T. Blunier, B. Barnett, M.L. Bender and M.B. Hendricks, *Biological oxygen productivity during the last 60,000 years from triple oxygen isotope measurements*, Glob. Biochem. Cycle **16** (3), 1029 (2002)

[Bor03] S. Borri, P. Cancio, P. de Natale, G. Giusfredi, D. Mazzotti and F. Tamassis, *Power-boosted difference-frequency source for high-resolution infrared spectroscopy*, Appl. Phys. B **76**, 473-477 (2003)

[Bos] Boston Electronics, Brookline MA, USA, *http://www.boselec.com/products/detir.html*

[Bow01] D.R. Bowling, P.P. Tans and R.K. Monson, *Partitioning net ecosystem carbon exchange with isotopic fluxes of CO_2*, Glob. Change Biol. **7**, 127-145 (2001)

[Bow03] D.R. Bowling, S.D. Sargent, B.D. Tanner and J.R. Ehleringer, *Tunable diode laser absorption spectroscopy for stable isotope studies of ecosystem-atmosphere CO_2 exchange*, Agri. Forest Meteo. **118**, 1-19 (2003)

[Boy68] G.D. Boyd and D.A. Kleinman, *Parametric Interaction of Focused Gaussian Light beams*, J. Appl. Phys. **36**, 3597-3639 (1968)

[Bre99] C.A.M. Brenninkmeijer, T. Röckmann, M. Bräunlich, P. Jöckel and P. Bergamaschi, *Review of progress in isotope studies of atmospheric carbon monoxide*, Chemos.: Glob. Change Sci. **1**, 33-52 (1999)

[Bus99] K.W. Busch and M.A. Busch (Eds.), *Cavity Ringdown Spectroscopy*, ACS Symp. Ser. **720**, American Chemical Society, Washington DC (1999), pp. 7-19

[Bye77] R.L. Byer and R.L. Herbst: Parametric oscillation and mixing, in *Nonlinear Infrared Generation*, Topics Appl. Phys. 16, Y.R. Shen (Ed.) (Springer, Berlin, Heidelberg 1977) pp. 81-137

[Cal99] I.G. Calasso and M.W. Sigrist, *Selection criteria for microphones used in pulsed nonresonant gas-phase photoacoustics*, Rev. Sci. Instrum. **70**, 4569-4578 (1999)

[Cas04] A. Castrillo, G. Casa, M. van Burgel, D. Tedesco, and L. Gianfrani, *First field determination of the $^{13}C/^{12}C$ isotope ratio in volcanic CO_2 by diode-laser spectrometry*, Opt. Exp. **12**, 6515-6523 (2004)

[Cas05] A. Castrillo, G. Casa, E. Kerstel and L. Gianfrani, *Diode laser absorption spectrometry for $^{13}CO_2/^{12}CO_2$ isotope ratio analysis: Investigation on precision and accuracy levels*, Appl. Phys. B **81**, 863-869 (2005)

[Che01] W. Chen, G. Mourat, D. Boucher, and F.K. Tittel, *Mid-infrared trace gas detection using continuous-wave difference frequency generation in periodically poled $RbTiOAsO_4$*, Appl. Phys. B **72**, 873-876 (2001)

[Che05] W. Chen, E. Poullet, J. Burie, D. Boucher M.W. Sigrist, J.J. Zondy, L. Isaenko, A. Yèlisseyev and S. Lobanov, *Widely tunable continuous-wave mid-infrared radiation (5.5–11 μm) by difference-frequency generation in $LiInS_2$ crystal*, Appl. Opt. **44**, 4123-4129 (2005)

[Cho72] M.M. Choy and R.L. Byer, *Accurate second-order susceptibility measurements of visible and infrared nonlinear crystals*, Phys. Rev. B **14**, 1693-1705 (1972)

[Chu68] T.B. Chu and M. Broyer, *Intracavity single resonance optical parametric oscillator*, J. Physique **45**, 1599-1616 (1968)

[Cla04] H.Y. Clark, L. Corner, W. Denzer, G. Hancock, A. Hutchinson, M. Islam, R. Peverall and G.D.A. Ritchie, *Difference frequency generation in periodically poled lithium niobate and its use in the detection of atmospheric methane*, Chem. Phys. Lett. **399**, 102-108 (2004)

[Cop06] T.B. Coplen, W.A. Brand, M. Gehre, M. Grönig, H.A.J. Meijer, B. Toman and R.M. Verkouteren, *New guidelines for $\delta^{13}C$ measurements*, Anal. Chem. **78**, 2439-2441 (2006)

[Cra57] H. Craig, *Isotopic standards for carbon and oxygen and correction factors for mass-spectrometric analysis of carbon dioxide*, Geochim. et Cosmochim. Acta **12**, 133-149 (1957)

[Cro02] E.R. Crosson, K.N. Ricci, B. Richman, F.C. Chilese, T.G. Owano, R.A. Provencal, M.W. Todd, J. Glasser, A.A. Kachanov, B.A. Paldus, T.G. Spence and R.N. Zare, *Stable isotope ratios using cavity ring-down spectroscopy: Determination of C-13/C-12 for carbon dioxide in human breath*, Anal. Chem. **74**, 2003-2007 (2002)

[Cry06a] Crystal Technology Inc.: Datasheet (Crystal Technology Inc., Palo Alto, California, USA, 2006), *http://www.crystaltechnology.com*

[Cry06b] Crystech Inc.: Datasheet (Crystech Inc., Shandong, Taiwan, 2005) *http:// www.crystech.com*

[Dah01] H. Dahnke, D. Kleine, W. Urban, P. Hering and M. Muertz, *Isotopic ratio measurement of methane in ambient air using mid-infrared cavity leak-out spectroscopy,* Appl. Phys. **B 72**, 121-125 (2001)

[Daw02] T.E. Dawson, S. Mambelli, A.H. Plamboek, P.H. Templer and K.P. Tu, *Stable Isotopes in Plant Ecology*, Annu. Rev. Ecol. Syst. **33**, 507-559 (2002)

[Dem00] W. Demtröder, *Laserpektroskopie: Grundlagen und Techniken*, Springer (Berlin, Heidelberg, 2000)

[Dmi93] V.G. Dmitriev, G.G. Gurzadyan and D.N. Nikogosyan, *Handbook of Nonlinear Optical Crystals*, (Springer, Berlin, Heidelberg, 1993)

[Dmi99] V. G. Dmitriev, G.G. Gurzadyan and D.N. Nikogosyan, *Handbook of Nonlinear Optical Crystals* 3rd Ed., Springer Ser. Opt. Sci., vol. 64, (Springer Berlin Heidelberg, 1999)

[Erd02] M. Erdélyi, D. Richter and F.K. Tittel, *$^{13}CO_2/^{12}CO_2$ isotopic ratio measurements using a difference frequency-based sensor operating at 4.35μm*, Appl. Phys. B **75**, 289-295 (2002)

[Esl00a] M.B. Esler, D.W. Griffith, S.R. Wilson and L.P. Steele, *Precision trace gas analysis by FT-IR spectroscopy. 1. Simultaneous analysis of CO_2, CH_4, N_2O, and CO in air*, Anal. Chem. **72**, 206-215 (2000)

[Esl00b] M.B. Esler, D.W. Griffith, S.R. Wilson and L.P. Steele, *Precision trace gas analysis by FT-IR spectroscopy. 2. The $^{13}C/^{12}C$ isotope ratio of CO_2*, Anal. Chem. **72**, 216-221 (2000).

[Esl00c] M.B. Esler, D.W.T. Griffith, F. Turatti, S.R. Wilson, T. Rahn and H. Zhang, *N_2O concentration and flux measurements and complete isotopic analysis by FTIR spectroscopy*, Chem. Glob. Change Sci. **2**, 445-454 (2000)

[Fai06] J. Faist, *Continuous-wave, room-temperature quantum cascade lasers*, Opt. Phot. News (OPN*)* **17**(5), 32-36 (2006)

[Fei02] K.L. Feilberg, S.R. Sellevag, C.J. Nielsen, D.W.T. Griffith and M.S. Johnson, *$CO + OH \rightarrow CO_2 + H$: The relative reaction rate of five CO isotopologues*, Phys. Chem. Chem. Phys. **4**, 4687-4693 (2002)

[Fis02] C. Fischer and M.W. Sigrist, *Trace-gas sensing in the 3.3-μm region using a diode-based difference-frequency laser photoacoustic system*, Appl. Phys. B **75**, 305-310 (2002)

[Fis03] C. Fischer, and M.W. Sigrist: Mid-IR Difference Frequency Generation, in *Solid-State Mid-Infrared Laser Sources*, Topics in Appl. Phys. **89**, I.T. Sorokina and K.L. Vodopyanov (Eds.) (Springer, Berlin, Heidelberg, 2003), pp. 97-140

[Fla98] L.B. Flanagan and J.R. Ehleringer, *Ecosystem-atmosphere CO_2 exchange: interpreting signals of change using stable isotope ratios*, Trends Ecol. Evol. **13**, 10-14 (1998)

[Fra99] K. Fradkin, A. Arie and G. Rosenman, *Tunable midinfrared source by difference frequency generation in bulk periodically poled $KTiOPO_4$*, Appl. Phys. Lett. **74**, 914-916 (1999)

[Fra00] K. Fradkin-Kashi, A. Arie, P. Urenski and G. Rosenman, *Mid-infrared difference-frequency generation in periodically poled KTiOAsO4 and application to gas sensing*, Opt. Lett. **25**, 743-745 (2000)

[Gag02] G. Gagliardi, F. Tamassia, P. de Natale, C. Gmachl, F. Capasso, D.L. Sivco, J.N. Baillargeon, A.L. Hutchinson and A.Y. Cho, *Sensitive detection of methane and nitrous oxide isotopomers using a continuous wave quantum cascade laser*, Eur. Phys. J. D **19**, 327-331 (2002)

[Gag03] G. Gagliardi, A. Castrillo R.Q.Iannone, E.R.T. Kerstel and L. Gianfrani, *High-precision determination of the $^{13}CO_2/^{12}CO_2$ isotope ratio using a portable 2.008-μm diode-laser spectrometer*, Appl. Phys. B **77**, 119-124 (2003)

[Gag05] G. Gagliardi, S. Borri, F. Tamassia, F. Capasso, C. Gmachl, D.L. Sivco, J.N. Baillargeon, A.L. Hutchinson and A.Y. Cho, *A frequency-modulated quantum-cascade laser for spectroscopy of CH_4 and N_2O isotopomers*, Iso. Environ. Health Stud. **41**, 313-321 (2005)

[Gho03] P. Ghosh and W.A. Brand, *Stable isotope ratio mass spectrometry in global climate change research*, Int. J. Mass Spectrom. **228**, 1-33 (2003)

[Gri00] D.W.T. Griffith, G.C. Toon, B. Sen, J.-F. Blavier and R.A. Toth, *Vertical profiles of nitrous oxide isotopomer fractionation measured in the stratosphere*, Geophys. Res. Lett. **27** (16), 2485-2488 (2000)

[Gri04] T.J. Griffis, J.M. Baker, S.D. Sargent, B.D. Tanner and J. Zhang, *Measuring field-scale isotopic CO_2 fluxes with tunable diode laser absorption spectroscopy and micrometeorological techniques*, Agricultural and Forest Meteorology **124**, 15-29 (2004)

[Gro02] V. Gros, P. Jöckel, C.A.M. Brenninkmeijer, T. Röckmann, F. Meinhardt and R. Graul, *Characterization of pollution events observed at Schauinsland, Germany, using CO and its stable isotopes*, Atmos.Environ. **36**, 2831-2840 (2002)

[Gsä] Gsänger Optoelektronik GmbH: Datasheet (Gsänger Optoelektronik GmbH, Planegg) *http://www.linos-photonics.de/en/homefr2.html*

[Hal04] D. Halmer, G. von Basum, P. Hering and M. Mürtz, *Fast exponential fitting algorithm for real-time instrumental use*, Rev. Sci. Instr. **75** (6), 2187-2191 (2004)

[Hal05] D. Halmer, G. von Basum, M. Horstjann, P. Hering and M. Mürtz, *Time resolved simultaneous detection of ^{14}NO and ^{15}NO via mid-infrared cavity leak-out spectroscopy*, Iso. Environ. Health Stud. **41**, 303-311 (2005)

[Han94] P.L. Hanst and S.T. Hanst, Gas measurements in the fundamental infrared region, in *Air Monitoring by Spectroscopic Techniques,* M.W. Sigrist (Ed.), Chemical Analysis Series, Vol. **127** (Wiley, New York, 1994), pp.335-470.

[Her64] D. Herriott, H. Kogelnik and R. Kompfner, *Off-Axis Paths in Spherical Mirror Interferometers*, Appl. Opt. **3**, 523-526 (1964)

[Her65] D.R. Herriott and H.J. Schulte, *Folded optical delay lines*, Appl. Opt. **4**, 883-891 (1965)

[Her80] J.M. Herbelin, J.A. McKay, M.A. Kwok, R.H. Uenten, D.S. Urevig, D.J. Spencer and D.J. Benard, *Sensitive measurement of photon lifetime and true reflectances in an optical cavity by a phase-shift method*, Appl. Opt. **19** (1), 144-147 (1980)

[Hitran96] L.S. Rothman, C.P. Rinsland, A. Goldman, S.T. Massie, D.P. Edwards, J.-M. Flaud, A. Perrin, C. Camy-Peyret, V. Dana, J.-Y. Mandin, J. Schroeder, A. McCann, R.R. Gamache, R.B. Wattson, K. Yoshino, K.V. Chance, K.W. Jucks, L.R. Brown, V. Nemtchinov and P. Varanasi, *The HITRAN Molecular Spectroscopic Database and HAWKS (HITRAN Atmospheric Workstation): 1996 Edition*, J. Quant. Spectrosc. Rad. Transf. **60**, 665 (1996)

[Hitran00] L.S. Rothman, A. Barbe, D. Chris Benner, L.R. Brown, C. Camy-Peyret, M.R. Carleer, K. Chance, C. Clerbaux, V. Dana, V.M. Devi, A. Fayt, J.-M. Flaud, R.R. Gamache, A. Goldman, D. Jacquemart, K.W. Jucks, W.J. Lafferty, J.-Y. Mandin, S.T. Massie, V. Nemtchinov, D.A. Newnham, A. Perrin, C.P. Rinsland, J. Schroeder, K.M. Smith, M.A.H. Smith, K. Tang, R.A. Toth, J. Vander Auwera, P. Varanasi and K. Yoshino, *The HITRAN molecular spectroscopic database: edition of 2000 including updates through 2001*, J. Quant. Spectr. Rad. Transf. **82**, 5-44 (2003)

[Hitran05] L.S. Rothman, D. Jacquemart, A. Barbe, D.C. Benner, M. Birk, L.R. Brown, M.R. Carleer, C. Chackerian Jr., K. Chance, L.H. Coudert, V. Dana, V.M. Devi, J.-M. Flaud, R.R. Gamache, A. Goldman, J.-M. Hartmann, K.W. Jucks, A.G. Macki, J.-Y. Mandin, S.T. Massie, J. Orphal,

A Perrin, C.P. Rinsland, M.A.H. Smith, R.N. Tolchenov, R.A. Toth, J. Vander Auwera, P. Varanasi and G. Wagner, *The HITRAN 2004 molecular spectroscopic database*, J. Quant. Spectrosc. Radiat. Transf., **96,** 139 (2005)

[Hör04] G. Hörner, S. Lau, Z. Kantor and H.-G. Löhmannsröben, I*sotope selective analysis of CO_2 with tunable diode laser (TDL) spectroscopy in the NIR*, Analyst **129**, 772-778 (2004)

[Hsu06] Y.K. Hsu, C.W. Chen, J.Y. Huang and C.L. Pan, *Erbium doped GaSe crystal for mid-IR applications*, Opt. Exp. **14**, 5484-5491 (2006)

[IPCC] Intergovernmental Panel on Climate Change (2001), *Climate Change 2001: The Scientific Basis*, Cambridge Univ. Press, New York, *http://www.grida.no/climate/ipcc_tar/*

[Iso07a] ChemiCool, *http://www.chemicool.com/definition/isotopologue.html* (2007)

[Iso07b] ChemiCool, *http://www.chemicool.com/definition/isotopomer.html* (2007)

[Jud] Judson Technologies LLC, Montgomeryville, USA, *http://www.judsontechnologies.com*

[Jun97] D.H. Jundt, *Temperature-dependent Sellmeier equation for the index of refraction, n_e in congruent lithium niobate*, Opt. Lett. **22**, 1553-1555 (1997)

[Kai06] J. Kaiser, A. Engel, R. Borchers and T. Röckmann, *Probing stratospheric transport and chemistry with new balloon and aircraft observations of the meridional and vertical N_2O isotope distribution*, Atmos. Chem. Phys. **6**, 3535-3556, 2006

[Ker99] E.R.Th. Kerstel, R. van Trigt, N. Dam, J. Reuss and H.A.J. Meijer, *Simultaneous Determination of the $^2H/^1H$, $^{17}O/^{16}O$ and $^{18}O/^{16}O$ isotope abundance ratios in water by means of laser spectrometry*, Anal. Chem. **71**, 5297-5303 (1999)

[Ker05] E.R.T. Kerstel, L.G. van der Wel and H.A.J Meije, *First real-time measurement of the evolving $^2H/^1H$ ratio during water evaporation from plant leaves*, Iso. Environ. Health Stud. **41**, 207-216 (2005)

[Kho03] A. Khorsandi, U. Willer, P. Geiser and W. Schade, *External short-cavity diode-laser for MIR difference-frequency generation*, Appl. Phys. B **77**, 509-513 (2003)

[Klu01] P. Kluczynski, J. Gustafsson, A.M. Lindberg and O. Axner, *Wavelength modulation absorption spectrometry – an extensive scrutiny of the generation of signals*, Spectrochim. Acta B **56**, 1277-1354 (2001)

[Kol95] S. Koletzko, M. Haisch, I. Seeboth, B. Braden, K. Hengels, B. Koletzko and P. Hering, *Isotope-selective non-dispersive infrared spectrometry for detection of Helicobacter pylori infection with ^{13}C-urea breath test*, Lancet **345**, 961 (1995)

[Kos05] A.A. Kosterev, Y.A. Bakhirkin and F.K. Tittel, *Ultrasensitive gas detection by quartz-enhanced photoacoustic spectroscopy in the fundamental molecular absorption bands region*, Appl. Phys. B **80**, 133-138 (2005)

[Kuo06] P.S. Kuo, K.L. Vodopyanov, M.M. Fejer, D.M. Simanovskii, X. Yu, J.S. Harris, D. Bliss and D. Weyburne, *Optical parametric generation of a mid-infrared continuum in orientation-patterned GaAs*, Opt. Lett. **31**, 71-73 (2006)

[Lal98] E. Lallier, M. Brevignon and J. Lehoux, *Efficient second-harmonic generation of a CO_2 laser with a quasi-phase-matched GaAs crystal*, Opt. Lett. **23**, 1511-1513 (1998)

[Lau06] T. Laurila, H. Cattaneo, T. Pöyhönen, V. Koskinen, J. Kauppinen and R. Hernberg, *Cantilever-based photoacoustic detection of carbon dioxide using a fiber-amplified diode laser*, Appl. Phys. B **83**, 285-228 (2006)

[Lee91] P.S. Lee, R.F. Majkowski and T.A. Perry, *Tunable diode laser spectroscopy for isotope analysis – Detection of isotopic carbon monoxide in exhaled breath*, IEEE Tran. Biomed. Engin. **38**, 966-973 (1991)

[Lev02] O. Levi, T.J. Pinguet, T. Skauli, L.A. Eyres, K.R. Parameswaran, J.S. Harris, Jr., M.M. Fejer, T.J. Kulp, S.E. Bisson, B. Gerard, E. Lallier and L. Becouarn, *Difference frequency generation of 8-μm radiation in orientation-patterned GaAs*, Opt. Lett. **27**, 2091-2093 (2002)

[Mad05] P. Maddaloni, G. Gagliardi, P. Malara and P. de Natale, *A 3.5-mW continuous-wave difference-frequency source around 3 μm for sub-Doppler molecular spectroscopy*, Appl. Phys. B **80**, 141-145 (2005)

[Mak03] J.E. Mak, G. Kra, T. Sandomenico and P. Bergamaschi, *The seasonally varying isotopic composition of the sources of carbon monoxide at Barbados, West Indies*, J. Geophys. Research, **108**, 4635 (2003)

[Man95] J.B. McManus, P.L. Kebabian and M.S. Zahniser, *Astigmatic mirror multipass absorption cells for long-path-length spectroscopy*, Appl. Opt. 34, 3336-3348 (1995)

[Man02] J.B. McManus, M.S. Zahniser, D.D. Nelson, L.R. Williams and C.E. Kolb, *Infrared laser spectrometer with balanced absorption for measurement of isotopic ratios of carbon gases*, Spectrochimica Acta, Part A **58**, 2465-2479 (2002)

[Man05] J.B. McManus, D.D. Nelson, J.H. Shorter, R. Jimenez, S. Herndon, S. Saleska and M. Zahniser, *A high precision pulsed quantum cascade laser spectrometer for measurements of stable isotopes of carbon dioxide*, J. Mod. Opt. **52**, 2309-2321 (2005)

[Mat00] B. Mattson, P. Sullivan, J. Fujita, K. Pound, W. Cheng, S. Eskestrand and V. Obenauf, *Microscale Gas Chemistry, Chapter Experiments with nitrous oxide*, (2000) *http://mattson.Creighton.edu/Microscale_Gases_Chemistry.html*

[Mau05] R. Maulini, D.A. Yarekha, J.-M. Bulliard, M. Giovannini, J. Faist, and E. Gini, *Continuous-wave operation of a broadly tunable thermoelectrically cooled external cavity quantum-cascade laser*, Opt. Lett. **30**, 2584-2586 (2005)

[Mil64] R.C. Miller, *Optical second harmonic generation in piezoelectric crystals*, Appl. Phys. Lett. **5**, 17-19 (1964)

[Moh07] J. Mohn, R.A. Werner, B. Buchmann and L. Emmenegger, *High-precision $\delta^{13}CO_2$ analysis by FTIR spectroscopy using a novel calibration strategy*, J. Mol. Struct. **834-836**, 95-101 (2007)

[Mol06] MolTech Molecular Technology GmbH: datasheet (MolTech, Berlin, 2006) *http://wwwmt-berlin.com*

[Moo00] W.G. Mook (Ed.), *Environmental Isotopes in the Hydrological Cycle: Principles and applications, Volume I: Introduction: Theory, Methods, Review*, International Hydrological Program IHP-V, Technical Documents in Hydrology, No.**39**, Vol.1, UNESCO, Paris (2000), *http://www.iaea.org/programmes/ripc/ih/volumes/volume1.htm*

[Moo01] W.G. Mook (Ed.), *Environmental Isotopes in the Hydrological Cycle: Principles and applications, Volume II: Atmospheric water*, International Hydrological Programme IHP-V, Technical Documents in Hydrology, No.**39**, Vol.2, UNESCO, Paris (2001), *http://www.iaea.org/programmes/ripc/ih/volumes/volume2.htm*

[Mos96] G.P. Moss, *Basic terminology of stereochemistry (IUPAC recommendations 1996)*, Pure & Appl. Chem **68** (12), 2193-2222 (1996)

[Mur94] D.E. Murnick and B.J. Peer, *Laser-based analysis of carbon isotope ratios*, Science **262**, 945-947 (1994)

[Mye96] L.E. Myers, R.C. Eckhardt, M.M. Feyer, R.L. Byer and W.R. Bosenberg, *Multigrating quasi-phase-matched optical parametric oscillator in periodically poled $LiNbO_3$*, Opt. Lett. **21**, 591-593 (1996)

[Nak04] F. Nakagawa, U. Tsunogai and T. Gamo, *Stable isotopic compositions and fractionations of carbon monoxide at coastal and open ocean stations in the Pacific*, J. Geophys. Res. **109**, C06016 (2004)

[Nei97] J.H. MacNeil, H.T. Zhang, P. Berseth and W.C. Trogler, *Catalytic Decomposition of Ammonium Nitrate in Superheated Aqueous Solutions*, J. Am. Chem. Soc. **119**, 9738-9744 (1997)

[Nel04] D.D. Nelson, B. McManus, S. Urbanski, S Herndon and M.S. Zahniser, *High precision measurements of atmospheric nitrous oxide and methane using thermoelectrically cooled mid-infrared quantum cascade lasers and detectors*, Spectrochimica Acta Part A **60**, 3325-3335 (2004)

[Nga06] A.K.Y. Ngai, S.T. Persijn, G. von Basum and F.J.M. Harren, *Automatically tunable continuous-wave optical parametric oscillator for high-resolution spectroscopy and sensitive trace-gas detection*, Appl. Phys B **85** (3), 173-180 (2006)

[Oke88] A. O'Keefe and D.A.G. Deacon, *Cavity ring-down optical spectrometer for absorption measurements using pulsed laser sources*, Rev. Sci. Instr. **59** (12), 2544-2551 (1988)

[Opp98] C. Oppenheimer, P. Francis, M. Burton, A.J.H. Maciejewski and L. Boardman, *Remote measurements of volcanic gases by Fourier transform infrared spectroscopy*, Appl. Phys. B **67**, 505-515 (1998)

[Pin74] A.S. Pine, *Doppler-limited molecular spectroscopy by difference-frequency mixing*, J. Opt. Soc. Am. **64**, 1683-1690 (1974)

[Rah97] T. Rahn and M. Wahlen, *Stable isotope enrichment in stratospheric nitrous oxide*, Science **278**, 1776-1778 (1997)

[Rai06] Raicol Crystals Ltd.: Datasheet (Raicol Crystals, Yehud, Israel, 2006) *http://www.raicol.com*

[Ric02] D. Richter, M. Erdélyi, R.F. Curl, F.K. Tittel, C. Oppenheimer, H.J. Duffell and M. Burton, *Field measurements of volcanic gases using tunable diode laser based mid-infrared and Fourier transform infrared spectrometers*, Opt. Lasers Engin. **37**, 171-186 (2002)

[Rob92] D.A. Roberts, *Simplified Characterization of Uniaxial and Biaxial Nonlinear Crystals: A Plea for Standardization of Nomenclature and Conventions*, IEEE J. Quantum Electron. **28**, 2057-2074 (1992)

[Röc01] T. Röckmann, J. Kaiser, C.A.M. Brenninkmeijer, J.N. Crowley, R. Borchers, W.A. Brand and P.J. Crutzen, *Isotopic enrichment of nitrous oxide ($^{15}N^{14}NO$, $^{14}N^{15}NO$, $^{14}N^{14}N^{18}O$) in the stratosphere and in the laboratory*, J. Geophys. Res. **106**, 10403-10410 (2001)

[Röc02] T. Röckmann, P. Jöckel, V. Gros, M. Bräunlich, G. Possnert and C.A.M. Brenninkmeijer, *Using ^{14}C, ^{13}C, ^{18}O and ^{17}O isotopic variations to provide insights into the high northern latitude surface CO inventory*, Atmos. Chem. Phys. **2**, 147-159 (2002)

[Röc03a] T. Röckmann, J. Kaiser and C.A.M. Brenninkmeijer, *The isotopic fingerprint of the pre-industrial and the anthropogenic N_2O source*, Atmos. Chem. Phys. **3**, 315-323 (2003)

[Röc03b] T. Röckmann, J. Kaiser, C.A.M. Brenninkmeijer and W.A. Brand, *Gas chromatography/isotope-ratio mass spectrometry method for high-precision position-dependent ^{15}N and ^{18}O measurement of atmospheric nitrous oxide*, Rap. Commun. Mass. Spectrom. **17**, 1897-1908 (2003)

[Sal06] S.R. Saleska, J.H. Shorter, S. Herndon, R. Jimenez, J.B. McManus, J.W. Munger, D.D. Nelson and M.S. Zahnizer, *What are the instrumentation requirements for measuring the isotopic composition of net ecosystem exchange of CO2 using eddy covariance methods?,* Iso. Environ. Health Stud. **42** (2), 115-133 (2006)

[Sch49] M. Schütze, *Ein neues Oxidationsmittel für die quantitative Überführung von Kohlenmonoxyd in Kohlendioxyd. Ein Beitrag zur Chemie des Jodpentoxids*, Ber. Dtsch. Chem. Ges. **77**, 484-487 (1949)

[Sch97] J.J. Scherer, J.B. Paul, A. O'Keefe and R.J. Saykally, *Cavity Ringdown Laser Absorption Spectroscopy: History, Development, and Application to Pulsed Molecular Beams*, Chem. Rev. **97**, 25-51 (1997)

[She97] Y.R. Shen, R.L. Aggarwal, B. Lax, R.L. Byer, R.L. Herbst, V.T. Nguyen, T.J. Bridges, J.J. Wynne, P.P. Sorokin and T.Y. Chang, *Nonlinear Infrared Generation, Topics in Appl. Phys.* (Springer, Berlin, Heidelberg, 1997)

[Sie86] A.E. Siegman, *Lasers*, University Science Books, Mill Valley, California (1986)

[Sig94] M.W. Sigrist (Ed.), *Air Monitoring by Spectroscopic Techniques,* Chemical Analysis Series, Vol. **127,** Wiley, New York (1994)

[Sil92] J.A. Silver, *Frequency-modulation spectroscopy for trace species detection: theory and comparison among experimental methods*, Appl. Opt. **31**, 707, 1992

[Smi65] W.G. Smiley, *Note on a reagent for oxidation of carbon monoxide*, Nucl. Sci. Abstr. **3**, 391 (1965)

[Sor01] I.T. Sorokina, E. Sorokin, A. Di Lieto, M. Tonelli, R.H. Page and K.I. Schaffers, *Efficient broadly tunable continuous-wave Cr^{2+}:ZnSe laser*, J. Opt. Soc. Am B **18**, 926-930 (2001)

[Sor03] I.T. Sorokina and K.L. Vodopyanov (Eds.), *Solid-State Mid-Infrared Laser Sources*, Topics in Applied Physics, Vol. **89** (Springer, Berlin, Heidelberg, 2003)

[Ste03] L.Y. Stein and Y.L. Yung, *Production, isotopic composition, and atmospheric fate of biologically produced nitrous oxide*, Annu. Rev. Plant. Sci. **31**, 329-356, 2003

[Str02] S. Stry, P. Hering and M. Mürtz, *Portable difference-frequency laser-based cavity leak-out spectrometer for trace-gas analysis*, Appl. Phys. B **75**, 297-303 (2002)

[Sup94] J.M. Supplee, E.A. Whittaker and W. Lenth, *Theoretical description of frequency modulation and wavelength modulation spectroscopy*, Appl. Opt. **33**, 6294, 1994

[Sut03] R.L. Sutherland, *Handbook of Nonlinear Optics 2^{nd} Ed.* (Marcel Dekker Inc., New York, 2003)

[Ted99] T. Tedesco and P. Sarsi, *Chemical (He, H_2, CH_4, Ne, Ar, N_2) and isotopic (He, Ne, Ar, C) variations at the Solfatara crater (southern Italy): mixing of different sources in relation to seismic activity,* Earth and Planet Sci. Lett. **171**, 465-480 (1999)

[The05] E. Theocharous, *Stability of the spectral responsivity of cryogenically cooled InSb infrared detectors*, Appl. Opt. **44**, 6087-6092 (2005)

[The06] E. Theocharous, *On the stability of the spectral responsivity of cryogenically cooled photoconductive HgDcTe infrared detectors*, Infra. Phys. Technol. **48**, 175 (2006)

[Thi02] M.H. Thiemens, *Mass-Independent Isotope Effects and their Use in Understanding Natural Processes*, Israel J. Chem. **42**, 43-54 (2002)

[Tit06] F.K. Tittel, D. Weidmann, C. Oppenheimer and L. Gianfrani, *Laser absorption spectroscopy for volcano monitoring*, Opt. Phot. News (OPN) **17**(5), 24-31 (2006)

[Tom06] E. De Tommasi, G. Casa and L. Gianfrani, *High precision determination of NH_3 concentrations by means of diode laser spectroscopy at 2.005 micron*, Appl. Phys. B **85**, 257 (2006)

[Trä07] H. Waechter and M.W. Sigrist, Generation of Coherent Mid-Infrared Radiation by Difference-Frequency Mixing, in *Springer Handbook of Lasers and Optics*, F. Träger (Ed.), Springer, Berlin Heidelberg (2007), pp. 801-814

[Tsu03] U. Tsunogai, Y. Hachisu, D.D. Komatsu, F. Nakagawa, T. Gamo and K. Akiyama, *An updated estimation of the stable carbon and oxygen isotopic compositions of automobile CO emissions*, Atmos. Environ. **37**, 4901-4910 (2003)

[Tur00] F. Turatti, D.W.T. Griffith, S.R. Wilson, M.B. Esler, T. Rahn, H. Zhang and G.A. Blake, *Positionally dependent ^{15}N fractionation factors in the UV photolysis of N_2O determined by high resolution FTIR spectroscopy*, Geophys. Res. Lett. **27** (16), 2489-2492 (2000)

[Tuz07] B. Tuzson, M.J. Zeeman, M.S. Zahniser and L. Emmenegger, *Quantum cascade laser based spectrometer for in-situ stable carbon dioxide isotope measurements*, Infra. Phys. Technol. (2007) doi: 10.1016/j.infrared.2007.05.006

[Ueh03a] K. Uehara, K. Yamamoto, T. Kikugawa. S. Toyoda, K. Tsuji and N. Yoshida, *Precise isotope abundance ratio measurement of nitrous oxide using diode lasers*, Sens. Actuat. B **90**, 250-255 (2003)

[Ueh03b] K. Uehara, K. Yamamoto, T. Kikugawa and N. Yoshida, *Site-selective nitrogen isotopic ratio measurement of nitrous oxide using 2 μm diode lasers*, Spectrochim. Acta A **59**, 957 (2003)

[Vig] VIGO System S.A., Warsaw, Poland, *http://www.vigo.com.pl*

[Vog06] D.E. Vogler and M.W. Sigrist, *Near-infrared laser based cavity ringdown spectroscopy for applications in petrochemical industry*, Appl. Phys. B **85**, 349-354 (2006)

[Wae06] H. Waechter and M.W. Sigrist: Trace gas analysis with isotopic selectivity using DFG-sources, in *Mid-Infrared Coherent Sources and Applications*, M. Ebrahimzadeh and I.T. Sorokina (Eds.), Nato Science Series II: Mathematics, Physics and Chemistry, (Springer, Berlin, Heidelberg, 2006)

[Wae07a] H. Waechter and M.W. Sigrist, *Mid-infrared laser spectroscopic determination of isotope ratios of N_2O at trace levels using wavelength modulation and balanced path length detection*, Appl. Phys. B **87** (3), 539-546 (2007)

[Wae07b] H. Waechter and M.W. Sigrist, Determination of $^{13}C/^{12}C$ and $^{18}O/^{16}O$ isotopic composition of carbon monoxide at trace level by using mid-infrared laser spectroscopy, Iso. Environ. Health Stud., submitted (2007)

[Web05] M.E. Webber, T. MacDonald, M.B. Pushkarsky, C.K.N. Patel, Y. Zhao, N. Marcillac and F.M. Mitloehner, *Agricultural ammonia sensor using diode lasers and photoacoustic spectroscopy,* Meas. Sci. Technol. **16**, 1547-1553 (2005)

[Wei04] D. Weidmann, F.K. Tittel, T. Aellen, M. Beck, D. Hofstetter, J. Faist and S. Blaser, *Mid-infrared trace-gas sensing with a quasi-continuous-wave peltier-cooled distributed feedback quantum cascade laser*, Appl. Phys. B **79**, 907-913 (2004)

[Wer01] R.A. Werner, M. Rothe and W.A. Brand, *Extraction of CO_2 from air samples for isotopic analysis and limits to ultra high precision $\delta^{18}O$ determination in CO_2 gas*, Rapid Commun. Mass Spectrom. **15**, 2152-2167 (2001)

[Whi42] J.U. White, *Long optical paths of large aperture*, J. Opt. Soc. Am. 32, 285 (1942)

[Whi00] W.M. White, *Isotope Geochemistry*, Chapter 9: Stable Isotopes, (2000), *http://www.geo.cornell.edu/geology/classes/geo455/Chapters.html*

[Wol05] M. Wolff, H.G. Groninga and H. Harde, *Isotope-selective sensor for medical diagnostics based on PAS*, J. Phys. IV France **125**, 773-775 (2005)

[Yak96] D. Yakir and X.F. Wang, *Fluxes of CO_2 and water between terrestrial vegetation and the atmosphere estimated from isotope measurements*, Nature **380**, 515-517 (1996)

[Yak00] D. Yakir and L.S.L. Sternberg, *The use of stable isotopes to study ecosystem gas exchange*, Oecologia (Berlin*)* **123**, 297-311 (2000)

[Yan06] T. Yanagawa, O. Tadanaga, Y. Nishida, H. Miyazawa, K. Magari, M. Asobe and H. Suzuki, *Simultaneous observation of CO isotopomer absorption by broadband difference-frequency generation using a direct-bonded quasi-phase-matched LiNbO3 waveguide*, Opt. Lett. **31**, 960-962 (2006)

[Zal95] P. Zalicki and R. N. Zare, *Cavity ring-down spectroscopy for quantitative absorption measurements*, J. Chem. Phys. **102**, 2708-2717 (1995)

[Zha00] H. Zhang, P.O. Wennberg, V.H. Wu and G.A. Blake, *Fractionation of $^{14}N^{15}N^{16}O$ and $^{15}N^{14}N^{16}O$ during photolysis at 213 nm*, Geophys. Res. Lett. **27** (16), 2481-2484 (2000)

Acknowledgement

Many people directly or indirectly contributed to the accomplishment of this thesis. In particular I wish to express my profound gratitude to Professor Markus W. Sigrist, the referee and supervisor of my thesis, for his full support and enthusiasm during the course of this project. He always had time for my problems, questions and gave me the freedom, assistance and encouragement to realize my ideas. By him, I learned not only to work accurately and exactly but also to promote the experimental results in the scientific community at international conferences.

I also wish to thank Professor Ursula Keller and Professor Frans J.M. Harren for their willingness of being my co-referees.

I also owe many thanks to my co-workers Richard Bartlome, Dilyan Marinov, Julien Rey and Daniel Vogler for the fruitful discussions, the friendly atmosphere and sharing of laboratory equipment. These discussions opened up new aspects for me to consider, which undoubtedly improved this work. It was a pleasure to work with them.

A special thank goes to my diploma and semester students Karen Robertson, Romedi Selm, Matthias Stahel and André Welti for their important contribution to this thesis. They have been highly motivated and it was a pleasure working with them.

Many thanks go to all my colleagues at the Department of Physics for borrowing equipment to me and for all their good advices.

Finally, I wish to express my deepest gratitude to Andreas M. Fischer, my family and my friends. They always encouraged me and without their confidence, assistance and patience I would not have come so far. Thank you so much for always being there for me.

This project was financially supported by the Swiss National Science Foundation.

Publications

Book Chapters

H. Waechter and M.W. Sigrist
"Generation of Coherent Mid-Infrared Radiation by Difference Frequency Mixing"
in Springer Handbook of Lasers and Optics, Chapter 11.10, F. Träger (Ed.), Springer (Berlin, Heidelberg, 2007)

H. Waechter and M.W. Sigrist
"Trace Gas Analysis with Isotopic Selectivity Using DFG-Sources"
in Mid-Infrared Coherent Sources and Applications, M. Ebrahimzadeh and I.T. Sorokina (Eds.), Nato Science for Peace and Security Series, Springer (Berlin Heidelberg, 2007)

Refereed Journal

H. Waechter and M.W. Sigrist
"Mid-infrared laser spectroscopic determination of isotope ratios of N_2O at trace levels using wavelength modulation and balanced path length detection"
Appl. Phys. B **87** (3), 539-546 (2007)

H. Waechter and M.W. Sigrist
"Determination of $^{13}C/^{12}C$ and $^{18}O/^{16}O$ isotopic composition of carbon monoxide at trace level by using mid-infrared laser spectroscopy"
Iso. Environ. Health Stud., submitted (2007)

Proceedings

H. Waechter and M.W. Sigrist
"Mid-IR laser-spectroscopic determination of isotope ratios at trace levels"
Dig. CLEO-Europe 2007, Munich (D), June 18-22 (2007), paper CH1-4-Mon

D. Vogler, H. Waechter and M.W. Sigrist
"Cavity Ringdown Spectroscopy for Petrochemical Process Monitoring"
Dig. CLEO-Europe 2005, Munich (D), June 12-17 (2005)
European Conf. Abstracts, Vol. 29B, paper CH2-2-THU

D. Vogler, H. Waechter and M.W. Sigrist
"Near-infrared Cavity ringdown Spectroscopy for Industrial Process Monitoring Applications"
4th Cavity Ring-Down User Meeting, Heeze (NL), October 7-8 (2004)

C. Fischer, D. Marinov, J. Rey, D. Vogler, H. Waechter and M.W. Sigrist
"Laser spectroscopy in sensing applications"
Dig. Optical Sciences Mini-Symposium, ETH Zurich, March 17 (2004)

D. Marinov, M.G. Müller, J. M. Rey, H. Waechter and M.W. Sigrist
"Advanced spectroscopic gas sensing for medical diagnostics and isotopic ratio measurement"
Dig. Optical Sciences Mini-Symposium, ETH Zurich, March 17 (2004)

Contributed oral presentations at conferences

H. Waechter and M.W. Sigrist
"Determination of isotopic composition of nitrous oxide and carbon monoxide at trace level by using difference frequency generation and balanced path length detection"
SIRIS 2007: 2nd International Workshop on Stable Isotope Ratio Infrared Spectrometry: New Developments and Applications, Florence (I), September 7-8 (2007)

H. Waechter and M.W. Sigrist
"Mid-IR laser-spectroscopic determination of isotope ratios at trace levels"
CLEO-Europe 2007, Munich (D), June 18-22 (2007)

D. E. Vogler, H. Waechter and M. W. Sigrist
"Cavity ringdown spectroscopy for petrochemical process monitoring"
CLEO-Europe 2005, Munich (D), June 12-17 (2005)

C. Fischer, D. Marinov, J. Rey, D. Vogler, H. Waechter and M.W. Sigrist
"Laser spectroscopy in sensing applications"
Optical Sciences Mini-Symposium, ETH Zurich, March 17 (2004)

Poster contributions at conferences

H. Waechter and M.W. Sigrist
"Laser-spectroscopic determination of isotope ratios at trace levels using difference-frequency generation"
6th International Conference on Tunable Diode Laser Spectroscopy, Reims (France), July 9-13 (2007)

D. Vogler, H. Waechter and M.W. Sigrist
"Near-Infrared Cavity Ringdown Spectroscopy for Industrial Process Monitoring Applications"
4th Cavity Ring-Down User Meeting, Heeze (NL), October 7-8 (2004)

D. Marinov, M.G. Müller, J. Rey, H. Waechter and M.W. Sigrist
"Advanced spectroscopic gas sensing for medical diagnostics and isotopic ratio measurements"
Optical Sciences Mini-Symposium, ETH Zurich, March 17 (2004)

Curriculum Vitae

Personal data

Name	Helen Waechter
Date of birth	4. 6. 1978
Civil status	single

Education

Oct. 03 – Oct. 07	PhD-student in Physics at ETH Zurich, Institute for Quantum Electronics, Laboratory for Laser Spectroscopy and Sensing
Oct. 98 – Apr. 03	Studies of Physics, ETH Zurich, Diploma thesis in collaboration with Opto Speed SA, Rüschlikon
Feb. 98 – July 98	Language Course at Auckland Language Centre, Auckland (New Zealand): First Certificate in English (FCE)
Aug. 91 – Jan. 98	Mathematisch-Naturwissenschaftliches Gymnasium, Zürich

Working Experience

Oct. 03 – Oct. 07	Research and Teaching Activities, ETH Zurich
Apr. 03 – July 03	Research Assistant, Opto Speed SA, Rüschlikon
Oct. 01 – Feb. 02	Teaching Assistant, ETH Zurich